Growth of 2D semiconductors and topological insulators

Maria Hilse[a,b,d], Nicholas Trainor[b], Andrew R. Graves[a,d], Run Xiao[c], Max Stanley[c], Yongxi Ou[c,d], Derrick Shao Heng Liu[b], Roman Engel-Herbert[f], Anthony Richardella[a,d], Stephanie Law[a,b,d,e], and Joan M. Redwing[b,d], [a] Materials Research Institute, The Pennsylvania State University, University Park, PA, United States; [b] Department of Materials Science and Engineering, The Pennsylvania State University, University Park, PA, United States; [c] Department of Physics, The Pennsylvania State University, University Park, PA, United States; [d] Two-Dimensional Crystal Consortium Materials Innovation Platform, The Pennsylvania State University, University Park, PA, United States; [e] Penn State Institute of Energy and the Environment, The Pennsylvania State University, University Park, PA, United States; and [f] Paul-Drude-Institut für Festkörperelektronik, Leibniz-Institut im Forschungsverbund Berlin e.V., Berlin, Germany

Key points

- Summary and classification of 2D layered chalcogenide-based semiconductors and topological insulators
- Properties of bulk and single layer 2D layered chalcogenides
- Fabrication of 2D layered chalcogenide bulk crystals
- Challenges and advantages of van der Waals epitaxy
- Fabrication of 2D layered chalcogenide thin films
- Synthesis methods of 2D layered topological insulators

Abstract

2D semiconductors exhibiting strongly anisotropic properties and non-trivial topological phenomena offer new material opportunities to find solutions for the energy crisis and global warming. Re-discovered after a lot of work nearly four decades ago, renewed research efforts fueled by recent advances in thin film growth technology are directed towards accelerating 2D materials' discovery, facilitating their synthesis, and studying their intrinsic properties. This chapter summarizes pursued synthesis approaches and the resulting materials properties of the three most common materials' classes among the 2D van der Waals layered semiconductors and topological insulators; post transition metal monochalcogenides, transition metal dichalcogenides, and Bi/Sb-based sesquichalcogenides.

Introduction

The rise and continued improvement of semiconductor materials has transformed society to a degree that almost every single aspect of modern daily lives, including those of critical importance ranging from personal health to national security, is facilitated by complementary metal oxide semiconductor (CMOS) technology (Zehen Prit Singh, 2023; Zhai, 2023). Perfecting semiconductor material quality over the past seven decades, as well as the associated device processing and fabrication technology has allowed to reach a near-perfection level, a mandatory requirement for the relentless scaling of the number of transistors per chip, keeping the pace with Moore's law (Radamson et al., 2020; Shalf, 2020; Külah et al., 2021; Chung et al., 2022). This extraordinary achievement has pushed semiconductor materials to the intrinsic physical limits of materials properties and device/fabrication concepts (Radamson et al., 2020; Shalf, 2020; Cao et al., 2023). Specifically, currently all technologically relevant semiconductor materials exhibit a 3D bonding geometry—which is originating from the sp^3-hybridized valence bonds—and thus a naturally occurring periodic arrangement of atoms in three dimensions, while scaling of electronic devices has driven spatial confinement of these 3D semiconductors to only a few atomic bond lengths in thin film thickness or channel dimension. The 3D bulk semiconducting properties—although predictable but not necessarily advantageously—are altered too much through quantum confinement effects, and a high density of unsaturated dangling bonds forming at their high-energy surfaces is leading ever more often to the break-down of conventional device concepts (Wang et al., 2023). Two-dimensional (2D) semiconductors, i.e., semiconductors consisting of single or few layers enabled by a highly anisotropic bonding geometry within these materials, give rise to ultra-low-energy surfaces due to the absence of dangling bonds. As a result, the single layers (SLs) within these materials are already intrinsically confined in one direction to the atomic scale. 2D semiconductors are therefore increasingly gaining importance as possible alternative choices of semiconductor materials (Radamson et al., 2020; Cao et al., 2023; Wang et al., 2023). The most compelling advantage of 2D systems arises from their strongly spatially anisotropic bonds with strong metallic and covalent bonds strictly limited to two dimensions (sp^2 hybridization), or quasi-two dimensions (sp^3-like hybridization) with very weak van der Waals (vdW) bonds in the third dimension (Hess, 2021). Approaching the structure and properties of such layered semiconductor compounds from a bonding perspective has been proven useful to understand their anisotropic structure and properties. Because of the saturation of all bonds in the third direction, i.e., in the vdW gap between SLs, these individual SLs have ultra-low surface, and interlayer binding energies (Wang et al., 2009; Cunningham et al., 2012; Huang et al., 2013; Annamalai et al., 2016; Mounet et al., 2018; Segev et al., 2018). As a result, their intrinsic in-plane properties like carrier and thermal transport properties are less affected by quantum mechanical confinement effects in the lightly bonded direction, thus allowing device concepts to remain intact even in the atomic scale limit when many interfaces are present in the electronic device (Huyghebaert et al., 2018; Lemme et al., 2022). Additionally, and maybe even more noteworthy, the unique binding geometry of 2D semiconductors lifts the epitaxial constraints inherent in 3D semiconductor heterostructures, and therefore facilitates the effortless integration of highly dissimilar materials to realize functional, new device concepts based on heterostructures with tailored properties made from structurally highly dissimilar materials (Huyghebaert et al., 2018; Radamson et al., 2020; Lemme et al., 2022; Cao et al., 2023; Wang et al., 2023). An added benefit of 2D vdW materials is furthermore their largely reduced dielectric screening effect—as well a consequence of the saturated bonds in the vdW gap between SLs. As a result, their properties can be generally easily modulated through external electric fields and many other external perturbations, substantially supporting the realization of ultra-high-efficiency, ultra-low-power electronics (Chaves et al., 2020; Bian et al., 2022).

To this end, topological insulators (TIs)—discussed in this chapter insofar as they are also part of 2D semiconductors—stand out with their unique carrier transport characteristics. In TIs, the spin-orbit coupling leads to a nontrivial topology of the electronic wave functions at the valence band maximum and conduction band minimum. Consequently, a non-trivial band structure topology arises causing gapless interface/edge or surface states when the TI is interfaced with an ordinary insulator, including vacuum (Ando, 2024). In the gapless states, i.e., edge states of a so called 2D TI and surface states of a so called 3D TI, the spin degeneracy of carriers is lifted and the spin is locked to its momentum ("spin-momentum locking") acting like an internal magnetic field with opposite signs for opposite spins. Due to their intriguing edge and surface conduction channels, TIs have the potential to unlock spin-dependent, highly dissipationless carrier transport—properties that are highly sought-after for spintronic applications, quantum computing, and systems that allow fundamental studies of electronic coupling and transport phenomena (Hou et al., 2019; Vaitkus et al., 2022; Ando, 2024). In contrast to the discussion above, the classification of 2D and 3D TIs does not refer to the crystallographic nature of the TI material. Instead, materials or heterostructures (of layered 2D vdW nature or not) showing a quantum spin Hall effect (QSHE) resulting from topological one-dimensional (1D) gapless edge states are referred to as 2D TIs, whereas intrinsic materials (of layered 2D vdW nature or not) that generalize the topological 1D edge states into topological 2D surface states are classified as 3D TIs (Ando, 2024).

The search for alternatives to the established 3D semiconductors and the rise of 2D materials has sparked significant investment in research and high-throughput computational-driven screenings of materials discovery of 2D crystal structures and phases (culminating for example in The 2021 Materials Genome Initiative Strategic Plan of the US government (National Science and Technology Council, 2021)). This resulted in a plethora of data bases (see for example The Materials Project (Jain et al., 2011, 2013; Aykol et al., 2018; Latimer et al., 2018; Wang et al., 2021; Merchant et al., 2023) and Materials Cloud (Mounet et al., 2018; Campi et al., 2023)) of lightly (vdW (Tang et al., 2022a)) and stronger bonded (non-vdW) 2D materials (McKinney et al., 2018; Friedrich et al., 2022). As a result, the field has made significant strides over the past decade to discover and classify 2D materials according to their interlayer bond strength (McKinney et al., 2018; Mounet et al., 2018; Tang et al., 2022a; Campi et al., 2023). Accepted vdW or quasi vdW bonded materials are materials with interlayer binding energies below (0.481−0.561) Jm^{-2}. In this range, materials were experimentally easily exfoliable, whereas higher interlayer binding energies cause enormous difficulties in layer exfoliation indicating that the nature of the interlayer bonding mechanism gradually changes to an increasing amount of ionic binding contribution to the extent of prohibiting exfoliation completely above 2.083 Jm^{-2} in interlayer binding energy.

This chapter will focus on the most researched compounds among the easily exfoliable intrinsic 2D van der Waals materials. These are the group-VI chalcogenides containing the elements sulfur, selenium, and tellurium (Ajayan et al., 2016; Kang et al., 2020; Bian et al., 2022; Hou et al., 2022; Liu et al., 2023b). An overview of semiconductors and topological insulators contained in this class is found in **Fig. 1** by plotting their band gap versus interlayer binding, i.e., surface energy. As an added benefit for materials and device synthesis, chalcogenides are considered earth-abundant and non-toxic elements (Shin et al., 2016; Fu, 2018). The most researched binary materials among the 2D vdW chalcogenide semiconductors can be divided into three sub-groups: the III-VI monochalcogenides like InSe and GaSe, the IV-VI tetrel-chalcogenides like SnSe and GeSe—combined forming the sub-group of post transition metal monochalcogenides (PTMMCs), the transition metal dichalcogenides (TMDs) like MoS_2, $MoSe_2$, $MoTe_2$, WS_2, WSe_2, WTe_2, HfS_2, and $HfSe_2$ as well as the V_2VI_3 sesqui-chalcogenides Bi_2Se_3, Bi_2Te_3, and Sb_2Te_3 as indicated in **Fig. 1**. 3D TIs among the 2D vdW materials are exclusively inherent to the last sub-group of Bi- and Sb-containing, i.e., heavy-weight constituents sesquichalcogenides with comparably small band gaps, whereas 2D TIs are formed at some TMD interfaces. For the

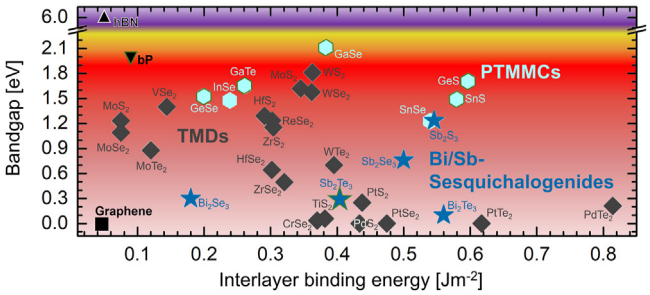

Fig. 1 Bandgap versus interlayer binding energy for the bulk 2D vdW chalcogenide [X = (S, Se, Te)] semiconductors with formulas MX − PTMMCs [with M = (Ga, In, Ge, Sn)], MX_2 − TMDs [with M = (W, Pt, Mo, V, Hf, Re, Pd, Zr, Cr, Ti)], and M_2X_3 − Bi/Sb-sesquichalcogenides [with M = (Bi, Sb)] as well as bP, hBN, and graphene. The bandgaps in TMDs span from far-infrared to the visible spectrum and their interlayer binding energies range for the most part at the mid to lower energy scale. The TMDs with zero, or close to zero bandgap in their bulk configuration are included as well since a sizeable gap opens in these materials towards the SL limit. PTMMCs possess mid to high interlayer binding energies making them harder to exfoliate, but their bandgaps are well matched to the solar spectrum. The Bi/Sb-sesquichalcogenides have on average the smallest bandgaps and their interlayer binding energies range at the mid to high energy scale. Only the materials with a green outline around their symbol have been demonstrated to show p-type transport characteristics, while all others are either n-type or ambipolar. The data to compose this image was sourced from references: (Wang et al., 2009; Jain et al., 2011; Cunningham et al., 2012; Huang et al., 2013; Annamalai et al., 2016; Ferhat et al., 2000; Samal and Rout, 2020; Zhang, 2015; Tan et al., 2016; Aykol et al., 2018; Latimer et al., 2018; Mounet et al., 2018; Bouša et al., 2020; Campi et al., 2023; Merchant et al., 2023).

ease of comparison, Fig. 1 also contains graphene, hexagonal boron nitride (hBN), and black phosphorus (bP) representing the purest form of vdW-bonded materials with lowest interlayer binding energies amounting to 0.047 Jm^{-2}, 0.050 Jm^{-2}, and 0.090 Jm^{-2}, respectively (Wang et al., 2009; Huang et al., 2013; Bouša et al., 2020). The PTMMCs SnSe, SnS, and GeS range with 0.54, 0.58, and 0.60 Jm^{-2}, respectively, right at the threshold of interlayer binding energy for easy exfoliation, whereas nearly all TMDs show surface energies clearly below that with the exception of $PtTe_2$ and $PdTe_2$. Only Sb_2S_3 and Bi_2Te_3 with 0.55 and 0.56 Jm^{-2}, respectively, are close to the easy exfoliation threshold among the Bi/Sb-sesquichalcogenides.

The traditional picture of band gap versus in-plane lattice parameters for the 2D vdW semiconductors in their bulk configuration is shown in Fig. 2. Many of the 2D vdW semiconducting chalcogenides have band gaps in the 1−2 eV energy range ideally matched to the solar spectrum, which elevates their potential for photovoltaic applications as well. In contrast to 3D semiconductors, the plot in Fig. 2 is not static for 2D materials, but instead depends on the thickness, i.e. the layer number, of the 2D material in question. General to all 2D vdW layered semiconductors is that their bandgap scales with the number of SLs due to quantum confinement alongside with reduced dielectric screening from adjacent SLs. Consequently, their bandgap is highly tunable by the number of layers: the bandgap increases as the layer thickness decreases. The bandgap tunability was in fact found to be one order of magnitude stronger in 2D compared to 3D materials (Velický and Toth, 2017; Chaves et al., 2020; Kang et al., 2020). The reduced dielectric screening from adjacent SLs in the SL limit of 2D materials furthermore leads to an increased exciton binding energy and for most materials changes the nature of the bandgap from indirect to direct or vice versa (Chaves et al., 2020). As a particular manifestation of the bandgap tuning Fig. 2 contains data points with vanishing band gap representing the noble metal dichalcogenides PdS_2, $PdSe_2$, $PtSe_2$, and $PtTe_2$—2D vdW chalcogenides that are metallic in their bulk configuration. Specifically, due to the large bandgap tunability, bandgaps as large as 1.37 eV for $PdSe_2$ and 1.2 eV for $PtSe_2$ are present in the single layer limit, rendering them semiconducting. Due to the relatively large interlayer binding energy, the bandgap is already reduced to 0.3 eV in bilayer $PtSe_2$ (Chaves et al., 2020). These drastic examples of thickness tuning from a metallic ground state in the bulk to a semiconductor band structure in its SL form brings an additional advantage for device fabrication. A thick, i.e., low-resistance metallic bulk region could serve as natural contact material to a SL-thick semiconducting channel of the same material aiding in the fabrication of low-resistance electrical contacts and circumventing the development of high doping schemes in the ever shrinking source and drain volume—a general challenge for both 3D and 2D semiconductor materials device fabrication (Ciarrocchi et al., 2018; Huyghebaert et al., 2018).

Many members of the PTMMC family (light blue hexagons in Figs. 1 and 2) have highly anisotropic effective masses due to their anisotropic crystal bond configuration and a resulting band structure like black phosphorus (bP) (Ajayan et al., 2016). Owing to their crystal structure, PTMMC materials generally show strong layer-dependent ferroelectric and piezoelectric properties (Fei et al., 2015; Manna et al., 2018; Priydarshi et al., 2022). Continuing the analogies to bP, PTMMCs have very low effective masses of electrons and holes and as a result show the highest carrier mobilities found among the 2D vdW chalcogenide compounds (Kang et al., 2020). Besides the high carrier mobilities that are found among the PTMMCs, they generally show excellent optical properties (Yu et al., 2021). Furthermore, this class of materials possesses potential for mid-temperature range thermoelectric applications, and contains the few semiconductors among all 2D vdW chalcogenides that are naturally inclined to be p-type, such as GaSe, GaTe, GeS, GeSe, and SnS (Shankar and Prabhu, 2023), which have been highlighted in Figs. 1 and 2 besides bP by a green outline around their symbol (Shankar and Prabhu, 2023).

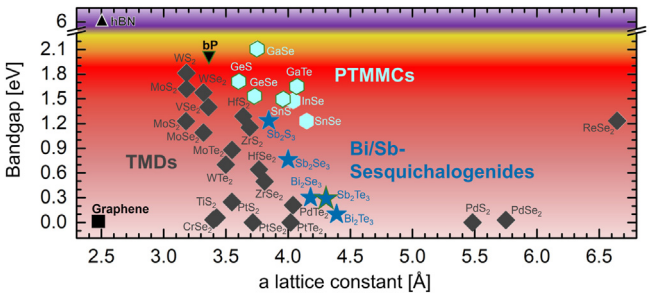

Fig. 2 Bandgap versus a lattice constant of the bulk 2D vdW chalcogenide [X = (S, Se, Te)] semiconductors with formulas MX − PTMMCs [with M = (Ga, In, Ge, Sn)], MX_2 − TMDs [with M = (W, Pt, Mo, V, Hf, Re, Pd, Zr, Cr, Ti)], and M_2X_3 − Bi/Sb-sesquichalcogenides [with M = (Bi, Sb)], as well as bP, hBN, and graphene. For crystal structures with two different in-plane lattice constants, the smaller one was chosen for this representation. TMDs possess bandgaps spanning from far-infrared to the visible spectrum and gather in their majority at the lower end of the lattice constants. The TMDs with zero, or close to zero bandgap in their bulk configuration are included as well since a sizeable gap opens in these materials towards the SL limit. Slightly higher lattice constants on average show the Bi/Sb-sesquichalcogenides with bandgaps almost exclusively in the far-to mid-infrared. PTMMCs gather at higher bandgaps in the visible spectrum with intermediate lattice constants. Only the materials with a green outline around their symbol have been demonstrated to show p-type transport characteristics, while all others are either n-type or ambipolar. The data to compose this image was sourced from references (Wang et al., 2009; Jain et al., 2011; Cunningham et al., 2012; Huang et al., 2013; Zhang, 2015; Annamalai et al., 2016; Ferhat et al., 2000; Samal and Rout, 2020; Tan et al., 2016; Aykol et al., 2018; Latimer et al., 2018; Mounet et al., 2018; Bouša et al., 2020; Campi et al., 2023; Merchant et al., 2023).

Inherent to the bulk configuration of TMDs (dark gray rhombi in Figs. 1 and 2) is their indirect band gap, which transitions for most of the TMDs into a direct band gap as the number of layers is reduced towards the SL limit. With this transition comes an increase in the optical absorption and radiative recombination efficiency despite a reduction of the material volume (Ajayan et al., 2016). Many TMDs have attracted attention due to their encouraging carrier mobilities at room temperature and first results of TMD field effect transistors (FETs) yielded high on/off ratios (Kang et al., 2020). The crystal structures of TMDs generally lack inversion symmetry, and the partially filled conduction bands mainly derived from *d* orbitals of the heavy transition metal atoms lead to a strong spin-orbit coupling (SOC). The pronounced SOC effect gives rise to spin-polarized split valence bands and hence a rich spin valley topology in the band structure (Ajayan et al., 2016). Furthermore, some TMDs have been shown to possess ferromagnetic properties down to the SL limit—traditionally regarded solely as a bulk or 3D property, absent in a 2D configuration (Mermin and Wagner, 1966; O'Hara et al., 2018; Zhang et al., 2021). Certain configurations of TMD SLs were in addition identified as 2D topological quantum spin Hall insulators (Bian et al., 2022). Most of the TMD semiconductors are n-type or ambipolar, whereas most p-type semiconductors were found among the PTMMC materials (Yu et al., 2021; Huang et al., 2022).

All Bi- and Sb-sesquichalcogenides (blue stars in Figs. 1 and 2) have very small band gaps and a non-trivial band structure, thus showing properties of 3D TIs (Cheng et al., 2019). These sesquichalcogenides have furthermore potential for low-temperature thermoelectric applications (Shankar and Prabhu, 2023). The reason for the remarkable thermoelectric, topological, and even phase-change properties observed in Bi- and Sb-containing sesquichalcogenides can be attributed to their highly unconventional metavalent bonding mechanism, i.e., neither covalent, metallic, or ionic, nor purely vdW (Cheng et al., 2019). Sesquichalcogenide TIs typically suffer from a parasitic n- or p-type bulk conductance stemming from defects that push the Fermi level away from the mid-gap and have it intersect with the bulk valence or conduction density of states, posing a materials challenge for accessing their topological surface states only (Koirala et al., 2015).

Many synthesis methods are being pursued to fabricate 2D semiconductors and TIs (Bian et al., 2022). Chemical vapor transport (CVT) and flux growth methods are to name for bulk single crystal growth. Since the crystal structure is very anisotropic and thus naturally quasi-2D, exfoliation of atomic-scale flakes from bulk crystals has gained tremendously in importance in this field of research. Exfoliation is typically done either mechanically or through liquid phase exfoliation, where the latter offers the added advantage of combined exfoliation and intercalation. Since exfoliation works so well for these types of 2D materials, extensive efforts with impressive results have been devoted to adjusting and refining the exfoliation process in ways that produce larger-area, higher-conformity thickness, i.e. high-quality flakes with high yield and reproducibility. Even after SLs or thin films of 2D chalcogenide materials are grown by bottom-up thin film growth methods, exfoliation, or layer transfer processes play an increased role in nowadays 2D heterostructure and device fabrication. Spiked by the demonstration of large-area, uniform graphene growth by chemical vapor deposition (CVD), CVD methods and among them in particular metal organic chemical vapor deposition (MOCVD) are currently at the forefront of bottom-up wafer-sized, reproducible fabrication of 2D chalcogenide semiconductors (Chubarov et al., 2021; Zhu et al., 2023a). Additionally, physical vapor deposition (PVD) techniques like molecular beam epitaxy (MBE) are also employed for bottom-up growth of 2D PTMMCs, sesquichalcogenides and TMDs.

This chapter gives a short introduction to each of the 2D vdW layered chalcogenide semiconductors and TIs and reviews their growth. After a general section outlining common considerations and challenges for the synthesis of these chalcogenide compounds, this chapter will discuss the growth and properties of PTMMCs, TMDs, and finally TIs in more detail in the following sections. A summary of and outlook into this emerging research field at the extension of the 2D vdW layered chalcogenide semiconductors and TIs will finally conclude this chapter.

General considerations and existing challenges for the growth of 2D chalcogenides

Since the PTMMCs, TMDs, and chalcogenide TIs considered here are from the same materials class of 2D layered chalcogenide materials, a short summary of commonalities between them—especially as far as they are concerned with their growth—will be discussed in the following. This section will first shed light on the vapor pressure mismatch between the elemental constituents of almost all chalcogenide compounds and the resulting formation of chalcogen vacancies, i.e., zero-dimensional (0D) point defects limiting the electronic purity achievable in 2D chalcogenide materials. Subsequently, the concept of vdW epitaxy will be introduced with a discussion of its inherent challenges and implications for the bottom-up synthesis of 2D chalcogenide semiconductors. Finally, the section will conclude by presenting a picture of the generally observed growth trends, demonstrating that controlling the nucleation density and increasing the lateral growth to overcome 1D line defect formation in these materials is key for high-quality 2D vdW semiconductor growth.

The vapor pressure mismatch

Depending on the selected growth approach, an important first consideration must be dedicated to the vapor pressure mismatch between the constituents forming the targeted chalcogenide compound. This challenges growth approaches where growth conditions deviate from equilibrium and growth kinetics like adsorption, desorption, and diffusion on the substrate as well as along edges play a tremendously important role. To this date, the different aspects directly affecting the chalcogenide layer growth kinetics are much less understood compared to the growth of 3D semiconductors, such as the growth of III-V nitrides, arsenides, or antimonides, but are coming into focus and are as such a research topic with a rapidly increasing number of publications in the field (Yue et al., 2017; Walsh et al., 2018). In many cases, chalcogenide growth involves low vapor pressure (refractory) metals as one constituent, which is in sharp contrast to the high vapor pressure of the chalcogen elements. Fig. 3 shows the vapor pressure of

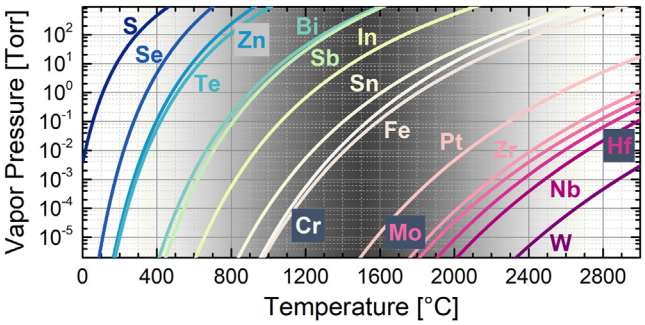

Fig. 3 Vapor pressure versus temperature for the chalcogens S, Se, and Te, as well as selected constituents of chalcogenide compounds representing transition metals, group-III, —IV, and —V elements demonstrating the high vapor pressure nature of the chalcogens in comparison to their most low to ultra-low vapor pressure compound counterpart.

typical chalcogenide compound constituents as a function of temperature. All three chalcogens have vapor pressures exceeding 10^{-1} Torr at temperatures below 500 °C, while the transition metal elements do have vapor pressures below 10^{-6} Torr even at temperatures well above 1000 °C.

This difference in vapor pressure manifests in two major challenges. First, it can be difficult to generate the high temperatures required to thermally evaporate pure transition metals, which can necessitate the use of higher vapor pressure intermediates such as oxides, halides, and organometallics or requires high-power thermal evaporation sources like electron beam evaporators that might impose an additional parasitic thermal load onto the substrate due to their high heat radiation. Second, approximating the compound as ideal solution, the large difference in the vapor pressures of the constituting elements and considering Raoult's law, large quantities of the chalcogen elements will evaporate from the forming layers and therefore must be often supplied in considerable excess at elevated growth temperatures, which are generally beneficial to enable crystallization and to enhance surface diffusivity. In fact, sticking coefficients of elemental and molecular chalcogen species were found to be zero already at 150 °C and above (Liu et al., 2021). Consequently, chalcogen-to-"metal" ratios on the order of 10^{5}-10^{6} are being used in MOCVD. The chalcogen-to-"metal" ratio is one of the primary parameters critically impacting the growth and crystalline quality of 2D chalcogenide compounds, which will be a recurring theme throughout this chapter. As **Fig. 3** demonstrates, the chalcogen-to-"metal" ratio requires precise flux control at very small "metal" supply and sufficiently large oversupply of the chalcogen.

The large vapor pressure mismatch is of particular impact for MBE growth. As a rule of thumb, the realization of structurally high-quality material in MBE requires a formation temperature, i.e., growth temperature, of 1⁄2 to 2⁄3 of the compound's melting point temperature (Yang and Flynn, 1989). This leads to an inherent challenge for the growth of materials with a high melting point like TMDs especially as the high vapor pressure chalcogen is extremely volatile in the required high temperature regime. Chalcogen desorption is thus one of the main factors that limits MBE growth to low temperatures as the available chalcogen oversupply spans only to chalcogen-to-"metal" flux ratios around 20—a factor of 10,000 smaller than typical ratios in MOCVD (Liu et al., 2020; Walsh et al., 2018). Those non-optimal growth conditions are shown to be the reason for the comparably low-quality TMD material grown by MBE characterized by small grain sizes and a high degree of rotational twin domain formation (Liu et al., 2020; Walsh et al., 2018; Yue et al., 2017).

The large vapor pressure mismatch, i.e., extremely high volatility and desorption rate of the chalcogen element during growth, is consequently the main reason for 0D point defects in 2D chalcogenides (Lin et al., 2016; Ko et al., 2024). Typical defects in these materials generally fall into one of two types: 0D point defects and 1D line defects, which will be discussed later on in section **Nucleation density and lateral growth**. The most common point defects are chalcogen vacancies (V_X), isovalent O-substitution (O_X), and a "metal" anti-site (M_x) (Xiao et al., 2024). Point defect densities in TMDs for example range around 10^{12}—10^{13} cm^{-2} (Zhussupbekov et al., 2021; Xiao et al., 2024). Such point defects have several consequences. First, they can electronically dope charge carriers into the material (Ko et al., 2024; Xiao et al., 2024). For example, chalcogen vacancies in all discussed chalcogenide compounds are expected from basic defect chemistry to be donor-like and are often considered the source of the intrinsic n-type conductivity found in the TMDs. For example, in MoS_2 and WS_2 they are considered as the main origin pushing the Fermi level up into the conduction band or below the valence band edge in the Bi/Sb-sesquichalcogenide TIs (Lin et al., 2016; Wang and Zhang, 2020; Zhu et al., 2021; Ko et al., 2024; Liebig et al., 2024; Xiao et al., 2024). However, more recent theoretical and experimental work indicates that chalcogen vacancies lead to deep defect levels in TMDs that can give rise to acceptor doping, while high concentrations again lead to donor-type behavior of these defects (Yang et al., 2019). Additionally, the incorporation of contaminants such as C and H at chalcogen sites can also lead to doping (Singh and Singh, 2019; Park et al., 2023). These defects furthermore can cause large conductivities for narrow bandgap TMDs like TiS_2, resulting in highly degenerative doping that masks their intrinstic semiconducting character (Wang et al., 2019b). Additionally, point defects can negatively impact carrier mobilities and can represent non-radiative recombination pathways, which negatively affect the luminescence yield as well as introduce new luminescence peaks (Tongay et al., 2013; Lin et al., 2016; Zhu et al., 2021; Xiao et al., 2024). Finally, point defects can change the energetics of stacking orientations in vdW epitaxy, which can result in lateral domain boundaries, i.e., 1D line defects (Nie et al., 2018; Zhang et al., 2019b,c; Mortelmans et al., 2020b).

van der Waals epitaxy

An important way to achieve single crystal thin films is the concept of epitaxy that will be discussed here within the framework of 2D materials, which is commonly referred to as vdW epitaxy across the entire field of 2D materials science to distinguish it from the conventional 3D materials epitaxy. Epitaxy is the utilization of a single crystalline substrate as a growth template from which the growing film inherits lattice periodicity, crystal symmetry and orientation. The ideal form of epitaxy is the homoepitaxial growth, where film and substrate are identical. In contrast, heteroepitaxial growth is the combination of two different materials, however if structurally and chemically sufficiently similar excellent results without formation of undesired phases at the interface can be achieved. Perfect epitaxy consequently leads to a single crystalline film and serves as the foundation for highly relevant and complex heterostructure devices, like light emitting diodes (LEDs) and lasers. In conventional epitaxy sketched in Fig. 4A, the film and substrate are bonded together at the interface via chemical bond formation across the interface. The film-substrate system minimizes its total energy by balancing the strain state in the film arising from a potential lattice parameter mismatch between film and substrate, the film and substrate surface dangling bond energies, and the formation energy of atomic structural defects and dislocations. An obvious straightforward case arises when film and substrate are perfectly lattice matched, all surface dangling bonds are easily saturated by atoms arriving at the substrate surface and initializing the film formation, i.e., the epitaxial process does not impose any additional energy barrier unto the system apart from the material's formation energy and the film grows relaxed. If film and substrate have different lattice parameters, epitaxial growth comes at the cost of free dangling bonds either in the substrate as shown in Fig. 4A or in the film, i.e., the formation energy required to create misfit dislocations. The two possible extreme cases under such conditions—fully relaxed or fully, i.e., coherently strained growth—are exemplarily depicted in Fig. 4A for a cube-on-cube epitaxy scenario. The fully relaxed case, i.e. the film's cubic unit cell assumes its unstrained dimension similar to its bulk and does not match the substrate's lattice parameter, is shown on the left in Fig. 4A. The energy required to deform the film lattice near the interface to accommodate the strain imposed by the substrate lattice is much higher than the energy required to form misfit dislocations. Therefore, the material in the film grows relaxed from the start and stitches coarsely together where bonds fit with the substrate resulting in an array of misfit dislocations at the interface. In the other extreme the biaxial strain imposed by the substrate deforms the film's cubic unit cell into a tetragonal shape to ideally match the film's in-plane lattice parameter to that of the substrate, shown on the right in Fig. 4A. Here, the formation energy of dislocations outweighs the deformation energy of the film to accommodate the imposed lattice parameter from the substrate. As a result, the film's lattice is deformed, and the film material grows fully strained with all bonds across the interface coherently matching up. In most cases, a situation between these extreme scenarios is found. Typically, the dislocation formation energy penalty will be paid for by increasing the strain state in the growing film until a certain threshold in thickness—critical thickness—is reached. At the critical thickness, the strain energy in the growing film has increased to the amount of energy required to create a misfit dislocation. Films thicker than the critical thickness will thus be (at least) partially relaxed and the interface will show an array of misfit dislocations. If the lattice mismatch is too large (>10 %), epitaxy of a continuous thin film may not be achievable (Ohtake et al., 2020).

For vdW materials, the absence of dangling bonds arising from the truncation of a 3D periodic crystal dramatically relaxes this criterion, allowing continuous film growth for combinations of 2D materials with widely different lattice parameters and structures—commonly referred to as vdW epitaxy—as sketched in Fig. 4B. For example, WSe_2 and hBN have an in-plane lattice mismatch of 32 % (with respect to hBN), which would prevent conventional epitaxial growth. However, WSe_2 can be grown epitaxially on hBN with (3×3) unit cells of WSe_2 matching to an coincidence site lattice of (4×4) unit cells of hBN (Zhang et al., 2019c). The relaxed

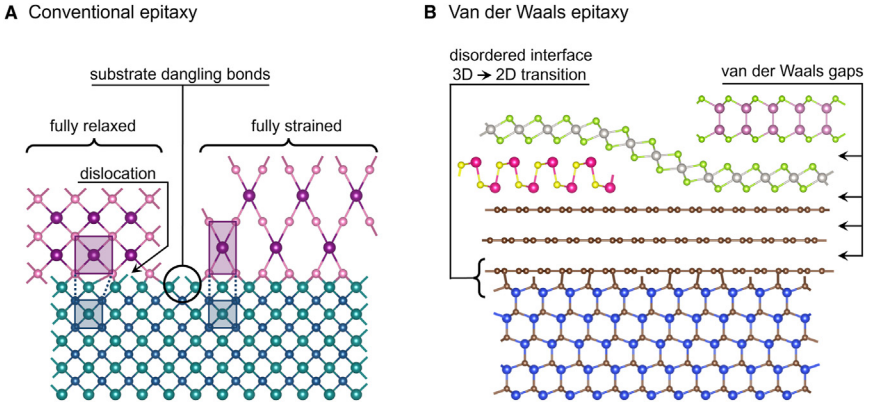

Fig. 4 Sketch of (A) conventional and (B) van der Waals epitaxy. In the case that materials are not lattice matched in conventional 3D epitaxy, the strong unsaturated dangling bonds at the interface are either partially left broken in the form of misfit dislocations at the interface to allow the film to grow relaxed (cube-on-cube) or impose an epitaxial strain upon the film that deforms the film lattice to match perfectly with the substrate at the interface (rectangle-on-cube). The lattice matching requirement is lifted in vdW epitaxy due to the inert surfaces of single layers with no dangling bonds. Dissimilar 2D vdW materials can thus grow in quasi-homoepitaxy on top of each other without the presence of misfit dislocations or epitaxial strain. If the growth platform, i.e., the substrate is a 3D material, a disordered interface realizes the transition from 3D to vdW epitaxy in the form of a substrate surface reconstruction and/or a surface passivation layer. This figure was created using Vesta (Momma and Izumi, 2011).

rules for van der Waals epitaxy in principle allow for a much larger pool of potential substrates and much increased design space for functional interfaces and heterostructures.

Symmetry considerations are very useful to predict vdW epitaxy and to get a handle on possible growth scenarios for different choices of substrates. Using point group theory, the number N of symmetrically equivalent orientations can be related to the orders n of substrate 2D point group G_{sub}, and film 2D point group G_{film} using the following equation (Grundmann, 2011; Dong et al., 2020b):

$$N = \frac{n(G_{sub})}{n(G_{sys})}$$

Where G_{sys} is defined as the largest common subgroup that G_{sub} and G_{film} share. For example, 2H−MoS_2 and graphene are represented by D_{3h} and D_{6h} point groups, respectively. For epitaxy, only the symmetries of the 2D growth plane need to be considered. For the growth of 2H−MoS_2 on graphene, this leads to $G_{sub} = C_{6V}$, and $G_{film} = C_{3V}$ (Wan et al., 2022). The shared largest subgroup between those two defines G_{sys} to C_{3V}. The orders for C_{3V} and C_{6V} are 6 and 12, respectively, which yields $N = 2$ equivalent orientations. Thus, MoS_2 should grow on graphene predominantly in 2 distinct orientations, which is indeed what is being observed (Batzill, 2018; Choudhury et al., 2020). This consideration changes for growth on hBN, which has also D_{3h} symmetry. The minimum number of expected orientations in this case is thus one, i.e., unidirectional growth should be possible on hBN, which was observed as well (Choudhury et al., 2020).

The drawback of vdW epitaxy is, however, that the lack of free unsaturated dangling surface bonds leaves the energetic landscape of the surface very homogeneous and inert for impinging adatoms. In conventional epitaxy, dangling bonds within the substrate surface determine the energetically most favorable nucleation sites, i.e., the lattice site at which the free adatom will get incorporated. This large modulation of the substrate surface energy landscape is the key for the film to inherit epitaxial information from the substrate. The adatom nucleation following a specific registry ensures the formation of a single crystal in one specific orientation over large scales without differently oriented structural domains. In vdW epitaxy, however, the substrate surface energy landscape modulation is much reduced due to the absence of unsaturated free dangling bonds. In other words, an order of magnitude smaller or less interaction force across the vdW gap compared to conventional epitaxy orders results in many different lattice sites at the substrate surface that are close to or even equivalent in energy for the nucleation of adatoms. This situation at least partially nullifies the above outlined symmetry considerations and originates a break-down of the long range coherency during film nucleation. For example, in MoS_2 growth on pristine hBN, the energy difference between 0° and 180° rotational domains is at most 0.5 meV per MoS_2 unit cell (Zhang et al., 2019b,c). Even at room temperature this small energy difference appears extremely small, which becomes even smaller compared to thermal energies k_BT for typical growth temperatures and causes the nucleation of structural domains with different in-plane rotational orientations. As the growth process evolves, these different domains coalesce and form rotational and mirror grain boundaries in the film, that have far-reaching implications on the properties of the film (Komsa and Krasheninnikov, 2017; Man et al., 2021; Kim, 2023). Thus, achieving unidirectional growth in vdW epitaxy is an inherent challenge that requires thoughtful and careful substrate surface engineering. For example, for the homoepitaxial growth of WSe_2, the Se vacancy defects present have far reaching implications to the extreme that the growing phase of WSe_2 is changed from 2H (no Se vacancies) to 3R depending on the vacancies being present or absent (Zhang et al., 2019c). Of similar benefit can be B vacancies in hBN for the growth of MoS_2 and WSe_2. Since both materials prefer to bind strongly to B vacancies in hBN, their intentional creation can alleviate the near degeneracy between the 0° and 180° orientations and yield larger than 90% unidirectional TMD growth on hBN (Zhang et al., 2019b,c). Out-of-plane stacking fault formation energies were found to assume very low energies as well, reaching from 0 to 27 meV per formula unit (fu) in the PTMMC InSe for example (Hilse et al., 2024). It is therefore highly likely that growth conditions far from equilibrium lead to an abundance of stacking faults. This has particular implications for some materials in the PTMMC family since the stacking sequence in materials like GaSe and InSe determines the respective phase and polymorph that forms. Consequently, MBE-grown films were indeed recently found to consist of a mixture of different polytypes to the degree that even novel polymorphs that do not exist in the bulk configuration of the material were observed in GaSe and InSe (Hilse et al., 2024; Yu et al., 2024a).

Finally, the relaxed rules for vdW epitaxy in terms of lattice mismatch tolerances are further put in perspective by the overall much reduced total surface energies of the 2D vdW materials. As demonstrated in **Fig. 1**, the majority of 2D vdW chalcogenide surfaces have energies at or below 0.6 Jm^{-2}, i.e., much lower than typical surface energies present in conventional epitaxy of 3D bonded materials as shown in **Fig. 5**. This has far-reaching implications for the growth mode, i.e., the way epitaxial growth develops from nucleation to the completion of a thin film. In 2D vdW materials, the strong in-plane bonds outweigh the weak out-of-plane vdW interaction forces by far, which implies for 2D vdW quasi-homoepitaxy (growth of a 2D vdW material on a same or different 2D vdW material as sketched above the 3D crystal in **Fig. 4**B) that the system favors lateral growth over the nucleation of new vertical nuclei, i.e., island growth until a SL is completed. It is therefore expected that these conditions should enable a perfect layer-by-layer growth mode. However, the energy penalty that the system must pay for creating new vertical nucleation is at most comparable to the available thermal energy k_BT in the non-equilibrium growth process. Hence, 2D vdW quasi-homoepitaxy almost exclusively progresses in the Volmer-Weber island growth mode rendering large-scale SL-growth and large-scale film thickness control extremely difficult to achieve (Chubarov et al., 2021; Wan et al., 2022; Li et al., 2024).

It appears similarly straightforward to assume perfect SL lateral growth for 2D vdW on 3D heteroepitaxy from basic surface energy considerations. Since, as shown in **Fig. 5**, the extremely low-energy inert SLs of 2D vdW materials should wet the comparably

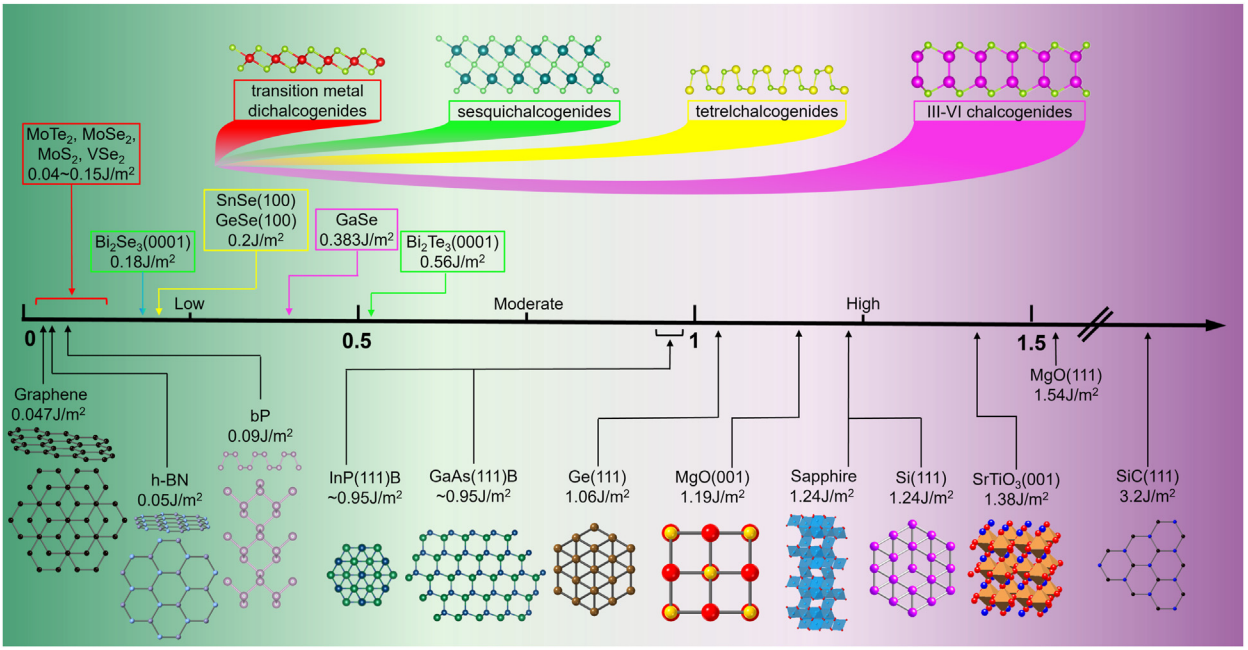

Fig. 5 Surface energy landscape of van der Waals epitaxy. Compared to the available conventional growth platforms, i.e., substrates like the selected InP, GaAs, Si, MgO, Al_2O_3, $SrTiO_3$, and SiC in this figure, 2D vdW materials have much reduced surface energies. The surface energies displayed in this graph were sourced from references: (Eglitis, 2014, 2015; Ferhat et al., 2000; Gendry et al., 1997; Gilman, 1960; Heifets et al., 2000; Jaccodine, 1963; Kumikov and Khokonov, 1983; Liu et al., 1999; Logsdail et al., 2015; Rathod and Hatzikiriakos, 2004; Sadan and Kaplan, 2006; Samal and Rout, 2020; Wander et al., 2003; Wang, 2009; Yamashita et al., 2010; Cunningham et al., 2012; Huang et al., 2013; Zhang, 2015; Annamalai et al., 2016; Tan et al., 2016; Segev et al., 2018).

much higher energy surface of the 3D crystal nearly perfectly. However, there are no free bonds available from the 2D SL that could stretch across the vdW gap and saturate the dangling substrate surface bonds while stabilizing an intact 2D SL. The 3D to 2D transition at the interface therefore leads to a disordered interfacial layer as depicted in **Fig. 4**B that effectively passivates the 3D surface bonds and provides a starting vdW template for 2D vdW quasi-homoepitaxy. Although little is known to date about the influence of the 3D to 2D interfacial transition layer on the properties of the 2D material, it was observed that it has a particular negative influence in Bi_2Se_3 growth on $Al_2O_3(0001)$ as it adds parasitic bulk electrons to the system that dominate the conductance through bulk over the topological surface states (Koirala et al., 2015). The 3D surface passivation in the form of chalcogen-assisted surface reconstructions or partial 2D layer growth was observed predominantly for growth on III-V, and group-IV semiconductors to either happen naturally during the growth process or was realized intentionally by introducing an additional growth step or substrate surface preparation step before the actual vdW epitaxy growth process (Yu et al., 2024a,c).

Nucleation density and lateral growth

The above discussed vapor pressure mismatch in the framework of vdW epitaxy of 2D chalcogenides was found to culminate in characteristic island nucleation patterns depending on the main growth parameters—temperature, and growth rate. Since the chalcogen constituent is the much more volatile species during growth with a desorption coefficient of 100 % under nearly all growth conditions, 2D vdW chalcogenide growth is intrinsically self-regulated and the growth rate determining species is the non-chalcogen element. Typically observed nucleation patterns for 2D vdW epitaxy were summarized well by kinetic Monte Carlo simulations for the growth of different TMDs that predicted the resulting number density and shapes of growth domains for varying growth conditions and are shown in **Fig. 6**A (Rajan et al., 2020). The general trend seen in **Fig. 6**A spans from an undesirable high nucleation density and poor lateral growth at high growth rates and low growth temperatures, resulting in a large number of small dendritic or fractal islands, to a much reduced nucleation density and increased lateral growth yielding regularly shaped large domains at low growth rates and high growth temperatures. **Fig. 6**B shows the resulting WSe_2 island morphologies for growth under different conditions as an experimental confirmation of this general trend (Yue et al., 2017). Low "metal" (non-chalcogen) fluxes and high substrate temperatures, i.e. low sticking coefficients and high non-chalcogen adatom mobility thus lead to the intended 2D layered growth and limit nucleation. In particular for TMDs high growth temperatures are required, driving up the chalcogen desorption rate and requiring huge overpressures/oversupply of the chalcogen counterpart. Consequently, this requires the above already mentioned extremely large chalcogen-to-"metal" ratios presenting an inherent challenge to the MBE growth approach.

The distinct nucleation and growth behavior of 2D vdW materials furthermore lead to a high number of line defects, such as grain boundaries that form consequently as growth progresses and the above discussed differently nucleated domains coalesce (Lin et al., 2016; Batzill, 2018; Man et al., 2021; Kim, 2023). Rotational grain boundaries emerge when film domains nucleated

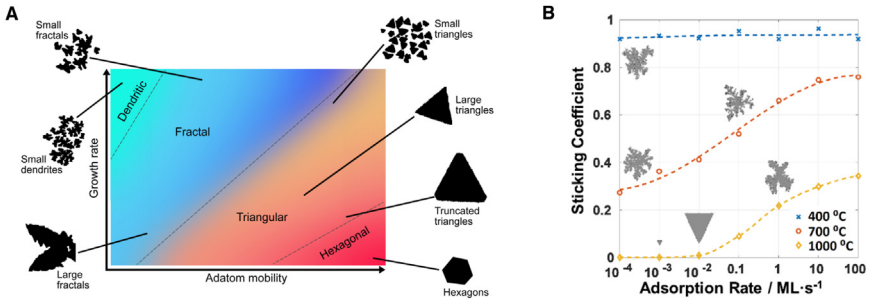

Fig. 6 Effect of growth kinetics during vdW chalcogenide epitaxy. (A) Observed island shapes and densities in kinetic Monte Carlo TMD growth simulations of different 2D vdW materials and their dependence on growth rate, i.e., non-chalcogen supply and adatom mobility of the non-chalcogen constituents, i.e., temperature. Small nucleation densities and large lateral scales of regularly shaped islands, i.e., conditions where lateral growth of existing nuclei dominates over new nucleation can be achieved at elevated temperatures and low growth rates. (B) Experimentally observed island morphology for vdW epitaxy of WSe_2 and its dependence on the W sticking coefficient, i.e., the temperature-dependent balance between supplied and desorbed W atoms with indicated temperature contour lines for 400, 700, and 1000 °C and the resulting W-determined growth rate of WSe_2. The largest regular growth domains were found at low growth rates and high temperatures. (A) Reprinted with permission from reference (Rajan et al., 2020). (B) Reprinted with permission from open access reference (Yue et al., 2017).

under different orientations laterally expand and finally touch. Among them, the specific case of a 180 °-rotation between domains is also referred to as mirror, twin, or inversion domain boundary, which are metallic in nature (Batzill, 2018). These spatially extended structural defects can be electronically very different from their surrounding matrix. Metallic line defects for example are detrimental for the class of semiconductors discussed here. They furthermore present scattering sites for carriers, which has negative impacts on the electronic properties (Ly et al., 2016; Vitale et al., 2018). Additionally, grain boundaries can create local strain fields that have the potential for nucleating screw dislocations and cause undesirable vertical growth (Nie et al., 2018). Several different approaches have been studied to reduce the number of grain boundaries and line defects to minimize their associated detrimental effects for many applications. The first is to reduce the number of possible orientations that domains can nucleate and grow in. This has been achieved for some materials via epitaxial growth and substrate engineering. As already outlined before, the proper selection of substrate, substrate surface engineering and growth parameters can lead to unidirectional domain alignment that has the potential to result in a coalesced SL free of rotational boundaries (Lin et al., 2016; Zhang et al., 2019b–d; Choudhury et al., 2020; Chubarov et al., 2021; Wan et al., 2022; Zhu et al., 2023a; Li et al., 2024). It should be noted, however, that even unidirectional growth can yield films that contain purely translational grain boundaries (Reifsnyder Hickey et al., 2021). However, this route is often not practical, particularly if direct deposition on a particular substrate is required. The second approach to reduce 1D line defects in 2D vdW materials is simply to reduce the total domain density. This approach roots in the fact that in a coalesced single layer, the areal density of grain boundaries roughly scales with the domain density (Mortelmans et al., 2020). Thus, the fewer domains nucleate, the less domain boundaries can form throughout the entire film. A low nucleation density can be achieved by fine tuning growth parameters, such as using higher growth temperatures, low "metal" fluxes, i.e. low growth rates, or the use of a seed promoter (Kim et al., 2017a; Mortelmans et al., 2021).

2D post transition metal chalcogenides

Introduction

Post transition metal chalcogenides (PTMCs) are a broad class of materials that have been known for decades, which have garnered renewed interest in the past decade. These materials are composed of post-transition metals (M) and chalcogens (X = S, Se, Te). In this case, M refers to elements in the periodic table between the transition metals and the metalloids and include Al, Ga, In, Tl, Ge, Sn, Pb, Sb, and Bi. Although there are a wide range of PTMC compounds with a variety of stoichiometries, the post-transition metal monochalcogenide (PTMMC) group, in which the ratio of the metal to the chalcogen is 1:1, is of particular interest due to their relatively simple crystal structures (Xu et al., 2016b; Sarkar and Stratakis, 2020; Barraza-Lopez et al., 2021; Yu et al., 2024b). The PTMMCs can be broken into four groups: GaX, InX, GeX, and SnX. Among these groups, GaS, GaSe, GaTe, InS, InSe, GeS, GeSe, SnS, and SnSe are typically classified as 2D layered materials, while InTe, GeTe, and SnTe are typically classified as 3D materials (Cheng et al., 2019; Arora et al., 2023; Wuttig et al., 2023). We will only discuss the 2D PTMMC materials in this chapter.

Crystal structures of PTMMCs

The 2D PTMMCs take on a variety of crystal structures. GaS, GaSe, InS, and InSe (GaX′ and InX′) all share a similar crystal structure, which is hexagonal in the plane with van der Waals bonds between the layers, as shown in **Fig. 7** for GaSe (Kuhn et al., 1975). Their unit cells are comprised of quadruple SLs with the atomic stacking X-M-M-X with X the chalcogen and M the metal element. Multiple stacking sequences are possible, leading to a large variety of polytypes, which often have different optical and electronic structures and properties. GaSe, for example, can form β (2H), ε (2H′), γ (3R), δ (4H), and γ′ polytypes, while InSe can form in the

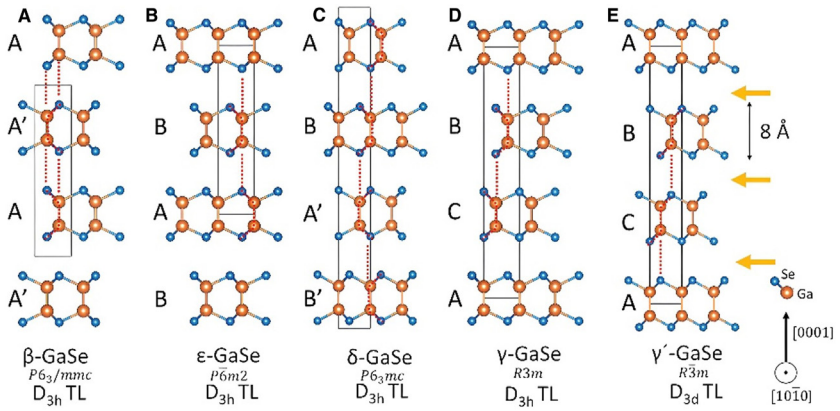

Fig. 7 Polymorphs and polytypes of the GaSe 2D vdW layered materials. Side-view sketches of the crystal structures of (A) β-GaSe, (B) ε-GaSe, (C) δ-GaSe, (D) γ-GaSe, and (E) γ'—GaSe. Highlighted are the vdW gaps by yellow arrows, the unit cells by black boxes, and the layer stacking sequence by red dashed lines. Reprinted with permission from open access reference (Grzonka et al., 2021).

β (2H), ε (2H′), and γ (3R) polytypes (Sun et al., 2018; Lim et al., 2020). As shown in **Fig. 7**A—D, the β, ε, γ, and δ polytypes are all based on the same SL and have different stacking sequences. This leads to larger effective c-axis lattice parameter: while β, and ε polytypes have a two SL repeating length, the γ polytype has a three SL repeating length, and the δ polytype has a four SL repeating length. The γ′ polytype has a slightly different centrosymmetric SL structure, resulting in very different optical properties, and has a repeat length of three SLs (Grzonka et al., 2021). As shown in **Fig. 7**, even in the SL limit, GaSe and InSe have multiple polytypes with different bond lengths and symmetries, while GaS and InS only assume a single polytype.

GeS, GeSe, SnS, and SnSe (GeX′ and SnX′) all share a crystal structure similar to black phosphorous (bP), a distorted orthorhombic rock salt structure, shown in **Fig. 8**A and B. GeSe, SnS, and SnSe can also form other polytypes (Von Rohr et al., 2017; Wei et al., 2017; Xu et al., 2017b; Yu et al., 2018; Lee et al., 2021). Under pressure, α-GeSe transitions through $R3m$ and $Fm\bar{3}m$ phase before finally stabilizing in the β-GeSe phase—also bP-like, but with a much larger lattice constant (Von Rohr et al., 2017; Xu et al., 2017b; Yu et al., 2018). Bulk SnX′ crystallizes in the black phosphorous crystal structure, as shown in **Fig. 8**D, in either the α-phase with a *Pnma* space group at room temperature or the β-phase with a *Cmcm* space group at high temperature. The phase transition from the α-to β-phase occurs at 873 K for SnS and 800 K for SnSe (Antunez et al., 2011; Xu et al., 2016a). Unlike the perfect 90° bond angle in a true black phosphorous structure, slight deviations in the cation-anion bond angles (θ_1 and θ_2) occur in α-SnX′, resulting in a lattice structure without inversion symmetry (Fei et al., 2016). While for the SL SnX′ many polymorphs exist that are shown in **Fig. 8**, the α phase remains the most studied structure (Gomes and Carvalho, 2015).

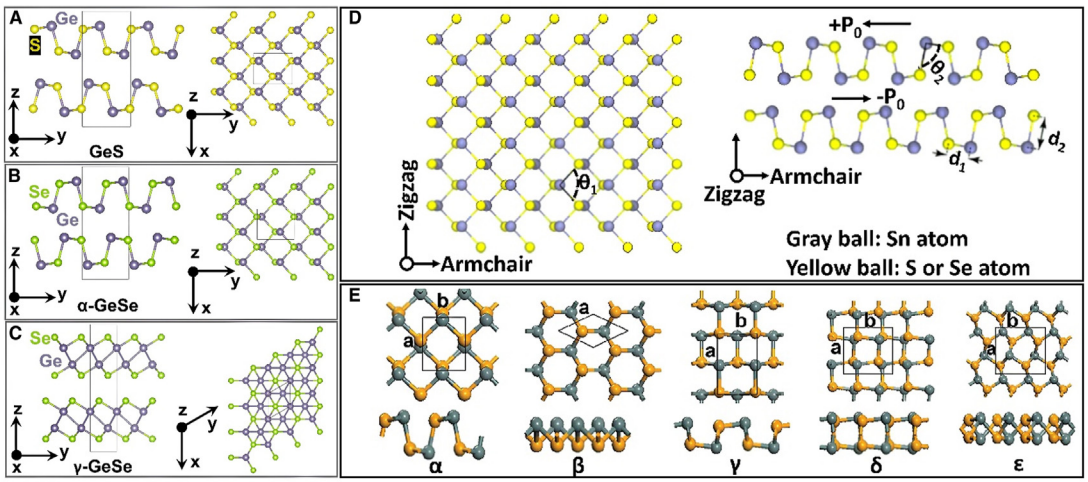

Fig. 8 Overview of the orthorhombic crystal structures of the Ge—, and Sn-PTMMCs. (A) GeS, (B) α-GeSe, and (C) as the only exception to the orthorhombic structures hexagonal γ-GeSe.(D) Top and side views of bulk α-SnX (X = S, Se) with $\theta_1 = 96.8°$ for SnS, and $\theta_1 = 96°$ for SnSe. $\theta_2 = 89°$ for both α-SnX. (E) Top and side views of SL SnX in different phases. (C) Reprinted with permission from reference (Yu et al., 2024b). (D) Reprinted with permission from reference (Titova et al., 2020) (E) Reprinted with permission from reference (Hu et al., 2017).

Properties of PTMMCs

The PTMMCs have a range of properties relevant for a variety of applications. In the bulk limit, bandgaps range from the mid-infrared to the blue, while in the SL limit, bandgaps range from the near-infrared to the ultraviolet (Antunez et al., 2011; Zhou et al., 2014; Jung et al., 2015; Hu et al., 2017; Sun et al., 2018; Grimaldi et al., 2020). The bandgap type often exhibits an unusual thickness-dependent behavior. For example, the bandgap of GaSe changes from direct to indirect with reducing layer number from the bulk to SL. Their tunable optical properties make these materials good candidates for photodetectors (GaS, GaSe, InSe), photovoltaics (GaS, GaSe, GeS, GeSe, SnS, SnSe), and infrared detectors (GaSe, SnSe) (Kübler et al., 2004; Hu et al., 2012, 2013; Lei et al., 2013, 2014, 2015; Nicolosi et al., 2013; Li et al., 2014; Yang et al., 2014b; Cao et al., 2015; Mudd et al., 2015; Ramasamy et al., 2016; Chang et al., 2017; Xue et al., 2017; Yan et al., 2017; Feng et al., 2018; Chen et al., 2019a; Mao et al., 2019b; Pan et al., 2019; Curreli et al., 2020; Murgatroyd et al., 2020; Hao et al., 2020a,b; Shang et al., 2020; Hu et al., 2022a; Shiffa et al., 2024). The anisotropic nature of the SnX′ and GeX′ crystals renders these material systems ideal candidates for polarization-sensitive optical devices (Allakhverdiev et al., 2009; Yüksek, 2012; Deckoff-Jones et al., 2016; Koskinen et al., 2017; Zhou et al., 2018b; Liao et al., 2020; Kim and Choi, 2021). In addition to their optical properties, the PTMMCs have applications in electronic devices such as field effect transistors (GaS, GaSe, InSe) spintronics (SnS, SnSe), and piezoelectrics (SnS, SnSe) (Late et al., 2012; Fei et al., 2015; Sucharitakul et al., 2015; Hu and Dong, 2016; Tian et al., 2016; Xu et al., 2017a; Huang et al., 2018; Lebedev, 2018; Gomes and Carvalho, 2020; Hu et al., 2022b; Singh et al., 2022; Liu et al., 2023a). Finally, the PTMMCs have applications in gas sensing (GaS, GaSe), catalysis (GaS, GeSe), thermoelectrics (GeSe, SnS, SnSe), and as ferroelectrics (InSe, SnS, SnSe) (Zhao et al., 2014; Harvey et al., 2015; Wang et al., 2015; Fei et al., 2016, 2016; Medrano Sandonas et al., 2016; Tan et al., 2016; Chowdhury et al., 2017; Shafique and Shin, 2017; Li et al., 2018a; Roychowdhury et al., 2018; Ul Haq et al., 2018; Yu et al., 2018; Bao et al., 2019; Hu et al., 2019, 2021; Wu et al., 2019; Chang et al., 2020; D'Olimpio et al., 2020; Higashitarumizu et al., 2020; Zhou et al., 2021; Minhas et al., 2022). Heterostructures can easily be made from the PTMMCs and can show superior performance over devices made from a single material. For example, a GeSe/SnSe heterostructure shows higher hole mobilities than either material alone, while heterostructures of GaSe and InSe have broader absorption bandwidths (Yan et al., 2017; Mao et al., 2019b). Due to their similar crystal structures, stacking GaX′ and InX′ or GeX′ and SnX′ layers is relatively straightforward.

Growth of PTMMCs

The 2D PTMMCs have been synthesized by employing a wide range of methods, utilizing both top-down and bottom-up approaches. Top-down methods include exfoliation, typically from crystals grown using the Bridgman method. Bottom-up methods include MBE, (MO)CVD, atomic layer deposition (ALD), and pulsed laser deposition (PLD). Exfoliation is not as commonly used for the PTMMCs as it is for other vdW materials, primarily due to the relatively high exfoliation energies inherent to the materials in this class, especially for the GeX′ and SnX′ families. The most commonly used bottom-up methods are MBE and MOCVD. Although it is highly desirable to obtain wafer-scale films of the 2D PTMMCs, multiple challenges need to be overcome. For all the MX materials, the chalcogen has a much higher vapor pressure than the metal atom, which typically necessitates an excess chalcogen flux during synthesis to compensate for the chalcogen desorption from the MX film. The growth of MX films is similar to the growth of III-As materials, with the metal atom controlling the growth rate and the chalcogen atom only bonding in the presence of an excess metal atom. Like most 2D materials, the PTMMCs suffer from twin defects arising from nucleating domains with two opposite orientations, pyramidal growth in which a second or third layer starts growing before the first layer has been completed, and spiral growth in which the domains grow like a spiral staircase with or without a screw defect at its center. In addition to these structural challenges, the PTMMCs also suffer from the presence of many polytypes with similar formation energies and a resulting lack of phase selectivity.

Polytype and polymorph selectivity

As noted above, the PTMMCs can have many different polytypes which often have different optical, and electronic properties albeit small structural changes. For most applications, polytype-pure films are required to ensure that the device functions as desired. Even if multiple polytypes are not detrimental to the functioning of a device, grain boundaries, stacking faults, and other defects arise when grains of two different polytypes coalesce. These defects can lead to enhanced nonradiative recombination, increased electron scattering, and generally to a poor device performance. The different polytypes often have different properties but extremely similar formation energies, making it challenging to synthesize wafer-scale polytype-pure films. However, some progress has been made in this area. Polytype-pure γ′ GaSe thin films have been grown on c-plane sapphire and GaAs(111) substrates using MBE. Density functional theory (DFT) calculations indicate that the γ′ polytype can be stabilized in a film with a sufficient density of gallium vacancies. For InSe, the γ polytype has recently been stabilized at a wafer scale, and there are previous reports of wafer-scale ε-InSe films, though it can be difficult to distinguish among the various polytypes since they often have similar X-ray diffraction (XRD) and Raman spectra. The two polytypes of GeSe are sufficiently different in structure making it relatively straightforward to synthesize polytype-pure films simply by choosing the appropriate substrate. However, to date, there have been very few successful syntheses of GeSe by any method, and those that were successful resulted in nanowires or nanosheets rather than large-area films. Since GaS, InS, and GeS have only one known polytype, synthesis of these materials is significantly easier.

Phase selectivity

Another challenge in the synthesis of PTMMC thin films is phase selectivity. The PTMMCs are a subset of the much broader PTMC family, which includes a range of stoichiometries such as M_2X, MX, MX_2 and M_2X_3. For many of the PTMCs, the MX stoichiometry occupies a narrow fraction of the M-X phase diagram, as shown in the phase diagrams for the MSe compounds in **Fig. 9**, and it often does not have the highest thermal stability. Obtaining a phase-pure film therefore requires careful control of the metal to chalcogen flux ratio, regardless of the synthesis method used. If too much of the chalcogen is supplied, the MX_2 and/or M_2X_3 phases will form, while if too little of the chalcogen is supplied, the M_2X phase or pure metal droplets will form. Because the window of flux ratios to produce the desired MX phase is narrow, films are prone to metal and/or chalcogen vacancies as well as metal droplets. Despite these challenges, phase-pure wafer-scale films of InSe, GaS, GaSe, SnS, and SnSe have been grown by tightly controlling the ratio of the metal to the chalcogen. To date, no wafer-scale films of InS, GeS, or GeSe have been produced. For InS, this is primarily due to the extremely narrow range of the phase diagram that InS occupies, while for GeX′, the formation of GeS_2 and $GeSe_2$ are significantly energetically favored over their monochalcogenide counterparts.

Thin film morphology and film coalescence

Coalescence of PTMMC films is generally challenging and is particularly problematic for growing SL or few-layer films. This can primarily be attributed to the poor wettability of the M atom on most substrates. As noted in the previous section, Ga, In, Ge, and Sn all tend to "ball up" and form droplets when deposited on a substrate, rather than wetting the surface and forming a smooth, ultrathin, coalesced metal film. This behavior influences the formation of the MX phase, often resulting in MX films comprised of discrete islands with three-dimensional growth taking place resulting in a high film surface roughness. This problem is particularly severe when MX films are grown by pure vdW epitaxy on non-vdW substrates such as c-plane sapphire or MgO. One way to promote coalescence is to change the surface chemistry using a two- or three-step growth. In these growth schemes, one or more layers of the MX film is deposited at a low temperature. The film is then annealed at a higher temperature to either form a coalesced layer, or to decompose the film completely. An example of a partial or complete decomposition three-step growth process and its resulting film is shown in **Fig. 10**. A 3 SL GaSe film grown by direct co-deposition on c-plane sapphire is shown in **Fig. 10**A by a reflection high energy electron diffraction (RHEED) image and **Fig. 10**B an atomic force microscopy (AFM) image. The RHEED image shows no crystallinity, and the AFM image shows droplets. A 3 SL GaSe film grown using the three-step substrate surface treatment on a c-plane sapphire substrate is shown in **Fig. 10**C by a RHEED image and **Fig. 10**D an AFM image. We see clear evidence of crystallinity in the RHEED image, and the AFM image is much smoother. A schematic of the three-step substrate treatment to grow GaSe is shown in **Fig. 10**E.

These steps change the substrate surface chemistry, either by forming a coalesced MX layer, by terminating the substrate with the chalcogen species, or through the formation of small, nanoscale MX islands. Subsequent layers can wet the surface more easily, resulting in smoother films with better coalescence. The use of vdW substrates such as hBN, graphene, or other 2D materials typically produces smoother films with a high degree of coalescence. Unfortunately, it can be difficult to obtain high-quality large-are vdW substrates. These substrates are furthermore often electrically conducting or have other properties that make them undesirable from a device perspective. Another option for improving film coalescence in the MX family is by using quasi-vdW epitaxy. In this growth mode, films are deposited on substrates with dangling bonds such as Si(111), GaAs(111), InP(111), or similar. This method can be particularly useful for the GaX′ and InX′ materials since they share a cation with commonly available III-V substrates. Many of

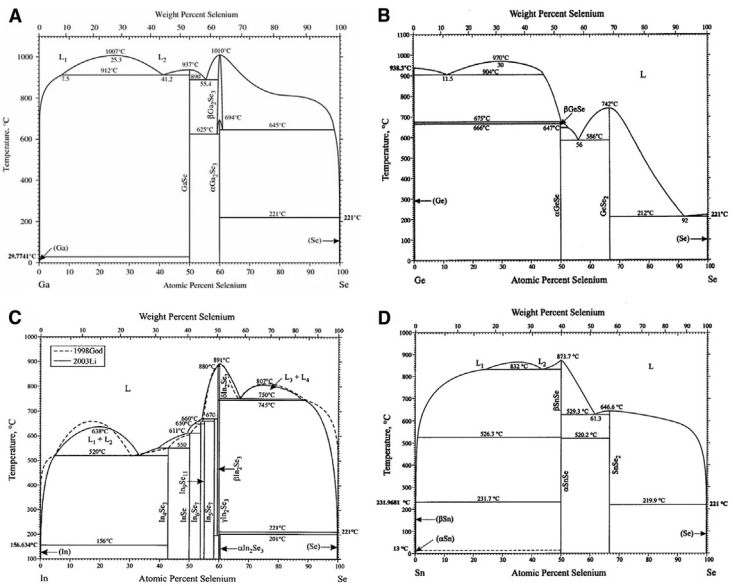

Fig. 9 Phase diagrams of the MSe compounds. (A) GaSe, (B) GeSe (C) InSe, and (D) SnSe. Reprinted with permission from references (Okamoto, 1998, 2000, 2004, 2009).

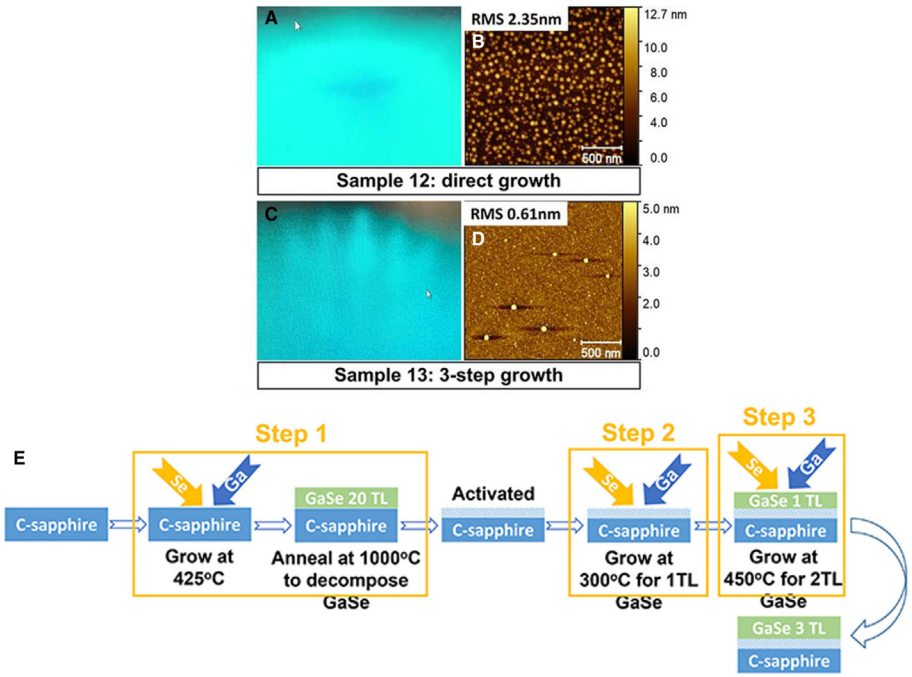

Fig. 10 Three-step growth of GaSe. (A) RHEED and (B) AFM images of sample 12 grown directly using optimal conditions. (C) RHEED and (D) AFM images of sample 13 grown using the three-step growth mode. (E) Diagram of the process for the three-step growth mode to grow a 3-SL-thick Ga_2Se_2 film. Reprinted with permission from reference (Yu et al., 2023).

the III-V or group IV substrates can be purchased in the (111) orientation, resulting in a hexagonal in-plane structure, matching the GaX′ and InX′ structures. Due to the high energy of the substrate surface arising from the dangling bonds, a quasi-vdW gap is formed at the interface between the MX film and the substrate. This stronger interaction can significantly improve wettability of the film on the substrate, resulting in smoother films with better coalescence compared to growth on inert, non-vdW substrates. Using a multi-step growth method with quasi-vdW epitaxy can further improve film quality. An additional benefit of growing on III-V or group IV substrates is the ability to grow complex semiconductor-based structures below the PTMMC layer for added device functionality.

More so than for many other chalcogenide thin films, the metal to chalcogen flux ratio has a strong impact on the morphology of PTMMC thin films. For example, in MBE growth of GaSe, Se:Ga flux ratios of 1.4 produce uncoalesced GaSe films with very small (∼10 nm) triangular domains. Increasing the flux ratio to 2.2 results in coalesced films with the typical triangular domain shape that are 100−200 nm in size. A further increase in flux ratio to 2.8 results in a poorly coalesced film with rounded island domains separated by deep pits. Similarly narrow flux ratio windows are found for InSe grown by MBE. At temperatures near the film decomposition point, a Se:In ratio of 4 results in triangular spiral growth. Slightly lower flux ratios of 2.5−3.8 result in coalesced films with triangular domains and no spiral growth. A further decrease in flux ratio to 1.3−2.5 gives rise to films with both triangular and hexagonal domains, though the spiral growth is still suppressed. Irrespective of its different crystal structure and valence state, SnSe films grown by MBE are also very sensitive to the metal to chalcogen flux ratio, generally showing three-dimensional growth when the Se:Sn ratio is above 1.35 and showing layer-by-layer growth for lower flux ratios. Tightly controlling the X:M ratio is therefore critically important to obtaining smooth, wafer-scale, phase-pure PTMMC layers and thin films.

In addition to flux ratio, substrate temperature is also a key parameter impacting the morphology of MX films. In general, films grown at low substrate temperatures have small domains and often exhibit three-dimensional growth and poor coalescence due to the relatively low adatom mobility of the metal atom. The low surface mobility of the adatom makes it more likely for a metal atom to nucleate a new domain rather than to diffuse to the edge of an already existing domain, leading to a higher density of smaller domains. Higher temperatures typically result in smoother films with larger domains due to the larger metal adatom mobility, and the smoothest films are often grown at or very near the thermal decomposition point of the film. For most chalcogenide materials, the chalcogen atom has a sizeable re-evaporation rate from the film surface at practical growth temperatures employed, necessitating the supply of a constant chalcogen flux to replace the atoms that have desorbed from the film. For MX films, the entire film will decompose at moderate temperatures (typically 300−400 °C) due to the relatively large instability of the M-X bond. If the MX film is grown at a substrate temperature just below the thermal decomposition point, adatom deposition and adatom or small molecule desorption will occur simultaneously. If the deposition rate is faster than the desorption rate, eventually a film will nucleate. The metal adatoms will have a relatively long diffusion length, making it more probable that they will bond to an existing domain. The smallest domains and the misoriented domains will be the most susceptible to re-evaporation, decreasing the density of domains. These effects work together to reduce pyramidal growth, in which the second layer nucleates before the first layer coalesces. The longer metal adatom mobility increases the probability that a metal adatom will incorporate at the edge of an existing domain rather than forming

a new domain on a second layer, and the increased probability of decomposition of small domains means that the second layer has a higher likelihood of desorbing. In addition to adatom mobilities, for MOCVD deposition, higher substrate temperatures promote precursor decomposition, which can improve the film's crystallinity and reduce defects.

Twin domain formation and defects

Like most 2D chalcogenides, GaX′ and InX′ thin films suffer from twin defects due to their hexagonal crystal structure. The hexagonal domain has three armchair sides and three zigzag sides, as shown in Fig. 11A. The higher density of dangling bonds along the zigzag edge results in a much faster growth rate of this side, which ultimately leads to the triangular shape of the GaX′ and InX′ domains. When growing these materials on a substrate that also has hexagonal symmetry (e.g. c-plane sapphire, Si(111), GaAs(111), etc.), domains can nucleate along two different crystallographic directions separated by 180° with zero or nearly zero energy difference. When two domains with opposite orientation try to coalesce, a twin or antiphase defect is formed. These defects are difficult to suppress. Some promise in reducing or eliminating twin defects in other 2D hexagonal material systems has been shown by using intentionally miscut substrates to align the domain nucleation, but this approach has not been widely adopted for the GaX′ and InX′ materials to date. Due to its orthorhombic and in-plane anisotropic crystal structure, SnX′ films can be grown twin-free by the correct choice of substrate. MgO, which has a square in-plane lattice, typically shows a high density of SnSe twin defects since it is equally energetically favorable for domains to nucleate in two directions separated by 90°. However, when SnSe is grown on a-plane sapphire, which has rectangular in-plane symmetry, almost 100 % of the SnSe domains are oriented in the same direction, resulting in a nearly complete suppression of twin defects. Since GeX′ has a similar crystal structure to SnX′, it is likely that a similar approach would suppress twin defects in this material as well, assuming other difficulties could be overcome.

The difference in growth rates between the armchair and zigzag edges can also lead to spiral growth. When the point of a domain encounters a substrate step, the fast growth rate of the zigzag edge results in the domain climbing over the step edge, as shown schematically in Fig. 11B. However, if the edge of a domain encounters a substrate step corner, the zigzag edge will grow more quickly than the armchair edge, ultimately resulting in spiral growth, as shown schematically in Fig. 11C. It is difficult to suppress spiral growth, though some success has been made by using higher growth temperatures. A higher substrate temperature may promote the desorption of domains that encounter a substrate step corner. When the zigzag edge climbs over the substrate step, it forms a very small domain. This domain is likely to be unstable to high temperatures, and thus may thermally decompose preferentially, while the larger domain underneath will be more stable and is thus more likely to remain. This would lead to a reduction in spiral growth due to the instability of the first spiral layer. It is also possible that high substrate temperatures result in a reconstruction of the dangling bonds on the edges of the domains that reduce the growth rate difference between the armchair and zigzag sides. For GaSe and InSe in particular, films grown near the thermal decomposition point often show hexagonal domains in addition to or instead of the typical triangular domains. Hexagonal domain shapes imply that the lateral growth rates on the armchair and zigzag edges are equal or nearly equal. In this case, spiral growth would not be expected to occur since spiral growth requires the zigzag sides to grow much faster than the armchair sides, and indeed, spiral growth is often suppressed or eliminated in GaSe and InSe films grown near the thermal decomposition point. If films were grown on substrates with c-axis lattice constants that were similar to the film's c-axis lattice constant, spiral growth would also be suppressed. Spiral growth has not been observed in the growth of SnX′ or GeX′ films, presumably due to their orthorhombic crystal structure, which should have similar growth rates along both edges.

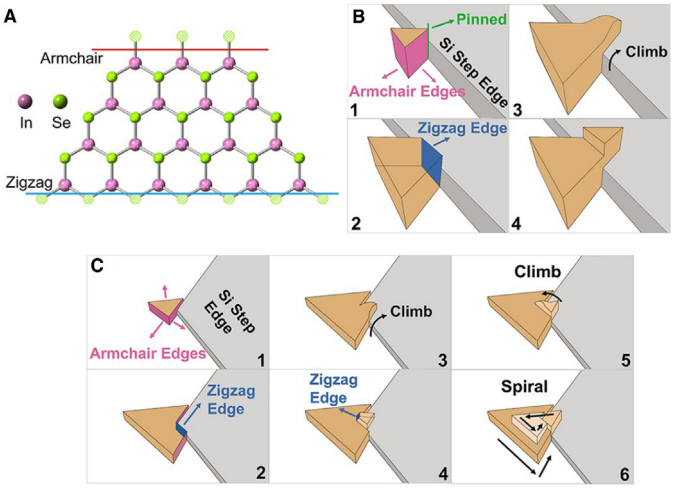

Fig. 11 Process of spiral growth. (A) Top view of a single InSe layer flake sketching its atomic arrangement. The pink line intercepts the In-terminated armchair edge, and the blue line intercepts the In-terminated zigzag edge. (B) Schematic lateral expansion flow of an InSe nucleus climbing over a Si(111) step edge. (C) Schematic lateral expansion of an InSe nucleus and spiral growth mode triggered by a step-edge corner. Reprinted with permission from reference (Liu et al., 2023a).

Thermal expansion

When growing thin films of PTMMC materials, one must also consider the coefficient of thermal expansion (CTE). These films are typically grown at moderate substrate temperatures of 300−600 °C. If the CTE of the film and substrate are very different, then upon cooling to room temperature, the film could be under significant compressive or tensile strain. For materials grown by pure vdW epitaxy, this problem may not be severe since the film/substrate interaction is relatively weak and the film can "glide" on the substrate. However, for films grown via quasi-vdW epitaxy on technologically important III-V or group IV substrates, a large mismatch in the CTE of the film and substrate can cause severe problems, including significant interfacial strain, film buckling, or film delamination. This effect is especially problematic for materials with large CTEs like GeS and GeSe or those with anisotropic or negative CTEs like SnSe.

Film oxidation

One major drawback of the PTMMC family is their degradation in ambient conditions. All members of this family are unstable upon exposure to air, with degradation times ranging from hours to weeks depending on the material and the specific storage conditions. Storing films in gloveboxes or in vacuum bags can significantly slow down the degradation process, but cannot completely stop it. This means that devices based on PTMMCs must be capped or encapsulated for long-term use. The choice of capping or encapsulation material depends on the details of the device as well as the conditions under which it is deployed. To date, successful capping layers include h-BN, graphene, and a variety of polymers and dielectrics.

Doping

Another roadblock towards the utilization of PTMMCs in devices is the difficulty doping these materials. The PTMMCs typically have Fermi energies deep in the conduction or valence bands due to high densities of point defects. GaS and InSe are typically n-type, while GaSe, SnS, SnSe, GeS, and GeSe are typically p-type. Traditional II-VI, III-V, and group IV semiconductors have established elements serving as donor and acceptor dopants which can be used to tune the Fermi energy. Although the PTMMCs are all semiconductors with moderate band gaps, a general solution for electron and hole doping has not been found. For traditional semiconductors, the dopant typically substitutes on the cation site. Dopants that substitute on the anion site exist but are much less commonly used. Following that formula, we should look for dopants that would substitute on the Ga, In, Ge, or Sn sites in the PTMMC family. This could include Si as an n-type dopant or Be as a p-type dopant for GaX′ and InX′, similar to conventional III-V compound semiconductor materials, though to date, there are very few examples of doping of GaX′ or InX′ with any dopant. A variety of dopants on both the Sn and S sites have been proposed for SnS; successful experimental realizations in thin film form include Na, Ag, and Cu as p-type dopants and Pb and Cl as n-type dopants. SnSe has been successfully p-type doped with Na, K, Ag, and In, while n-type doping has been achieved with Bi, Cl, Br, and I. However, doping SnS and SnSe is challenging due to the anharmonic bonding and the low solubility of dopants. In addition, working with the halogens is technically challenging. Due to the difficulty of synthesizing GeX′ thin films, doping has not been explored. Overall, the question of doping in the PTMMCs is still open, with the ideal dopants yet to be determined.

Summary and outlook

Overall, the PTMMCs have a range of useful and interesting properties with applications across a range of fields including optics, electronics, spintronics, ferroelectrics, and more. Making heterostructures of the PTMMCs will further expand the range of opportunities for these materials. However, to maximize their potential, a variety of technical challenges must be overcome. These include synthesis methods to achieve polytype-pure GaSe and InSe films, n- and p-type dopants for all PTMMCs, techniques for eliminating twin defects and spiral growth, and methods of encapsulation that are compatible with device applications.

Transition metal dichalcogenides

Introduction

Transition metal dichalcogenides (TMDs) comprise a specific class of layered chalcogenide crystals that have garnered significant attention in recent years due to their unique properties at the single layer to few-layer limit and its potential for applications in various fields. The TMDs, with a generalized formula of MX_2, where M is a transition metal and X represents a chalcogen (S, Se, Te) element, exhibit a range of intriguing electronic, optical, mechanical, and catalytic properties (Wang et al., 2012; Chhowalla et al., 2013; Novoselov et al., 2016). Their strong in-plane and relatively weak out-of-plane vdW-like bonding facilitates exfoliation of ultra-thin films from bulk crystals and layer transfer to or from a variety of substrates. This leads to chemical anisotropy whereby the vdW basal plane in TMDs is largely passivated while the edge facets are chemically reactive. These attributes make TMDs attractive candidates for use in a variety of applications including electronics, photonics, sensing, catalysis and energy storage.

Semiconducting TMDs, such as MoS_2 and WSe_2, for example, exhibit distinctive electronic band structures, with a transition from an indirect gap in bulk crystals to a direct bandgap in SL form, leading to enhanced optoelectronic properties (Ganatra and Zhang, 2014). In general, TMDs exhibit strong light-matter interactions, making them attractive candidates for photodetectors and image sensors (Koppens et al., 2014; Long et al., 2019). The electronic properties of SL TMDs are furthermore strongly

dependent on their surrounding dielectric environment, making them promising candidates for applications in gas sensing (Joshi et al., 2018; Lee et al., 2018). The high carrier mobility of TMDs in the SL limit has sparked much attention for their possible use in ultra-scaled field-effect transistors for next generation logic circuits and for 3D integration (Chhowalla et al., 2016; Akinwande et al., 2019). Their atomically thin nature imparts exceptional mechanical flexibility and strength, opening possibilities for flexible electronics and wearable devices, whereas the edge facets of TMDs possess remarkable catalytic activity, rendering them promising candidates for catalysts in hydrogen evolution and oxygen reduction reactions (Akinwande et al., 2014; Su et al., 2018).

Synthesis methods for TMDs must be selected while keeping the specific property and application of interest in mind. For example, bulk crystals synthesized by CVT and flux growth methods offer superior crystallinity, but produce material that is typically limited to only a few millimeters in size (Han et al., 2018; Zhang et al., 2019d). CVD techniques are scalable to wafer sizes compatible with semiconductor manufacturing ((150−300) mm) but produce films with grain boundaries and point defects (Hu et al., 2023). Catalysis and electrochemical applications that rely on access to the edge facets benefit from synthesis methods that produce textured films with the c-axis parallel to the substrate surface (Yazdani et al., 2019). By understanding the synthesis strategies and the resulting material properties, the full potential of TMDs can be realized for advancing technologies across a wide range of applications.

Crystal structures of TMDs

Fig. 12 shows the two primary polytypes of TMD SLs. Both structures consist of one monolayer of metal atoms sandwiched between two chalcogen monolayers, where each metal and chalcogen atom is bonded to 6 chalcogen and 3 metal atoms, respectively. Importantly, these bonds only occur within each SL and there are no chemical bonds between different layers. Rather, the interlayer interaction is via weak vdW forces, which allows TMDs to be easily cleaved and thinned down to the SL limit. Moreover, the lack of dangling bonds means that TMD SLs are stable. Nearly all TMDs possess a hexagonal crystal structure with 3-fold in-plane rotational symmetry, with the main difference between the two pictured polytypes being the alignment of the chalcogen atoms. In the trigonal prismatic phase (Fig. 12A), the chalcogen atoms are aligned vertically, giving rise to a horizontal mirror plane. Furthermore, this phase lacks inversion symmetry, which will strongly impact the electronic properties.

There are two primary stacking arrangements for trigonal prismatic layered TMD SLs. In the 2H arrangement, the SLs are stacked with alternating orientation with odd- and even-layered systems having D_{3h} and D_{3d} symmetry, respectively (D_{6h} symmetry in the bulk). In contrast in the 3R phase, the trigonal prismatic SLs are stacked without a change in orientation but are shifted with respect to each other. The resulting crystallographic system therefore has C_{3v} symmetry regardless of the number of SLs. Meanwhile, in the octahedral phase (Fig. 12B), the chalcogen layers are rotated by 60° with respect to each other. This structure thus possesses inversion symmetry but lacks the horizontal mirror plane. Octahedral SL stacks are achieved without translation or rotation with respect to each other to form the 1T phase, which has D_{3d} symmetry independent of the total number of SLs (Ribeiro-Soares et al., 2014). Finally, some TMDs such as ReS_2 display distorted versions of these structures (Chhowalla et al., 2013; Lin et al., 2015).

Properties of TMDs

The properties of TMDs span a wide range from semiconducting to superconducting electronic characteristics. The physics of transition metal compounds is often complex due to the presence of transition metal d orbital electrons in the valence band and strong spin-orbit coupling. With that in mind, some basic periodic trends can be observed within the family of TMDs. Generally, TMDs containing even-group (4—Ti, Zr, Hf; 6—Cr, Mo, W; and 10—Ni, Pd, Pt) transition metals (excluding Ti and Mo) form typically semiconductors as expected from basic band theory, with the bandgap decreasing with increasing chalcogen size. However, there are some exceptions like the semi-metallic WTe_2 for example (Chhowalla et al., 2013; Li et al., 2017). TMDs with odd-group transition metals such as V, Nb and Ta are often metallic or semi-metallic, as expected from basic band theory. However, an exception here is for example ReS_2, which is a semiconductor (Chhowalla et al., 2013; Lin et al., 2015). Furthermore, a wide range of exotic behaviors like charge density waves (CDWs), ferromagnetism, and superconductivity has been found in TMDs (Chhowalla et al., 2013; Wang et al., 2017; Bonilla et al., 2018).

The most studied TMDs are the 2H semiconducting group-6 (M = Cr, Mo, W) sulfides and selenides MoS_2, $MoSe_2$, WS_2, and WSe_2. These materials are indirect semiconductors in bulk form but transition to direct-gap semiconductors when thinned down to a SL due the interplay between interlayer and spin-orbit coupling (Sun et al., 2016b). Fig. 13 shows a schematic of the band

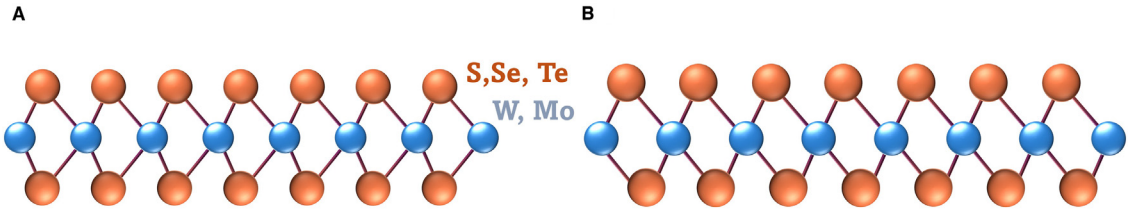

Fig. 12 The two polytypes of TMD SLs. (A) In the trigonal prismatic arrangement, the chalcogen atoms are aligned vertically, resulting in a horizontal mirror plane. This system lacks inversion symmetry, which has consequences for the band structure. (B) In the octahedral arrangement, the chalcogen layers are rotated with respect to each other. This breaks the mirror symmetry of the SL but grants inversion symmetry.

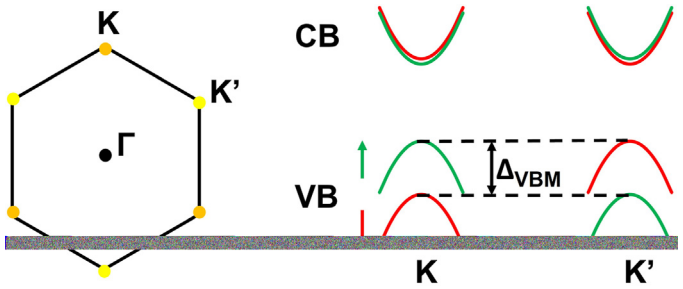

Fig. 13 Sketch of the band structure of the Mo/W-sulfides and selenides in the 2H phase. The VBM and CBM are located at the K and K′ points at the edge of the Brillion zone. Due to the lack of inversion symmetry, the band structure displays spin-orbit coupling, highlighted by the red and green bands. The resulting spin splitting is largest at the VBM (Δ_{VBM}) due to the symmetry of the transition metal orbitals that make up those states.

structure for a SL. The valence band maxima (VBM) and conduction band minima (CBM) lie at the K and K′ points at the corners of the Brillouin zone. Unlike in graphene, the K and K′ points are not equivalent due to the broken inversion symmetry of the 2H phase (Zhu et al., 2011; Xiao et al., 2012). One important feature of TMD band structures is the presence of spin-orbit coupling. Atomic spin-orbit coupling is a relativistic effect that is becoming more dominant for heavier elements, such as Mo and W, where the energy of an electronic state depends on how the electron's spin and orbital angular momentum are aligned (Kaxiras and Joannopoulos, 2019). When such heavy atoms are placed in a crystal that lacks inversion symmetry, the band structure itself can display spin-orbit coupling. This effect can be understood via three simple equalities and inequalities (Zhu et al., 2011; Xiao et al., 2012; Gilardoni et al., 2021). If time-reversal symmetry is maintained, i.e., no external or internal magnetic field is present, then, by Kramer's degeneracy theorem, the energy dispersion must be symmetric when spin and momentum are flipped:

$$E\left(\vec{k},\uparrow\right)=E\left(-\vec{k},\downarrow\right)$$

However, in a system with broken inversion symmetry, the band dispersion is not symmetric when the momentum alone is flipped, which necessitates that the dispersion cannot be spin-degenerate.

$$E\left(\vec{k},\uparrow\right)\neq E\left(-\vec{k},\uparrow\right)\Rightarrow E\left(\vec{k},\uparrow\right)\neq E\left(\vec{k},\downarrow\right)$$

Thus, instead of a set of spin-degenerate bands, the band structure will consist of a set of non-degenerate bands accommodating the different spin states. The effect of spin-orbit coupling on TMD band structure is shown in **Fig. 13**. At K and K′ valleys, the spin-orbit interaction lifts the spin-degeneracy, resulting in valleys that differ in spin and energy. Because of time-reversal symmetry, the spin states at the K and K′ valleys are flipped. Thus, the spin and valley degrees of freedom are coupled, an effect commonly referred to as spin-valley polarization. The spin splitting Δ is largest for the VBM as the electronic states there are primarily comprised of in-plane dx^2-y^2 and dxy orbitals of the transition metal element, as well as the px and py orbitals from the chalcogen (Zhu et al., 2011; Xiao et al., 2012; Gilardoni et al., 2021). In contrast, the electronic states of the CBM are primarily comprised of the out-of-plane metal dz^2 and chalcogen pz orbitals, which results in a much weaker spin splitting that is typically on the order of 10s of meV (Xiao et al., 2012; Mak and Shan, 2016; Gilardoni et al., 2021). Many semiconductor systems that lack inversion symmetry, display such spin-orbit coupling, and its effect generally scales with the atomic mass of the constituents (Jancu et al., 2005). It is therefore due to the large atomic numbers of transition metals that TMDs exhibit large spin splitting with Δ_{VBM} between 150 meV for MoS_2 and 480 meV for WSe_2. As a rule of thumb, for a given chalcogen X, the spin splitting of WX_2 is $\sim$ (280−290) meV larger than for MoX_2, while for a given metal M, the spin splitting of MSe_2 is about $\sim$ (30−40) meV larger than for MS_2 (Mak and Shan, 2016).

Furthermore, since the bandgap is direct, it is easy to photoexcite carriers. Using circularly polarized light, one can populate different valleys and create carriers with different spins, which can be useful for spin- and valleytronics (Mak et al., 2012; Xiao et al., 2012). One important feature of spin-valley coupling is that it can strongly enhance spin and valley lifetimes due to the combination of symmetry and conservation requirements for scattering processes (Xiao et al., 2012; Gilardoni et al., 2021). Additionally, valley polarization lifetimes can be dramatically increased by creating multilayered vertical heterostructures as the staggered band alignment results in charge separation and the formation of interlayer excitons (Kim et al., 2017b).

TMDs also display strong excitonic effects due to a reduction in dielectric screening. Because electrons and holes have opposite electric charges, they will be attracted to each other, forming bound pairs called excitons that possess a hydrogen-like spectra. **Fig. 14** shows an archetypical energy diagram and photoluminescence (PL) spectra for a TMD exciton. The exciton binding energy E_b (purple in **Fig. 14**) is the energy difference between the bound exciton E_A (green in **Fig. 14**) and free carrier band gap E_G (black in **Fig. 14**) (Ugeda et al., 2014). In a bulk material, the electron-hole interaction will be dielectrically screened, resulting in a small exciton binding energy. For example, the measured values for E_b for Si and GaAs are about 15 and 4 meV, respectively (Nam et al., 1976; Green, 2013). However, when a semiconductor is atomically thin, as in the case of TMDs, then the electric fields mediating the electron-hole interaction is not entirely confined to the semiconductor but protrudes into the surrounding environment, in particular in the few-layer or single layer limit. This in turn leads to the large exciton binding energies of about (0.1−0.5) eV observed in

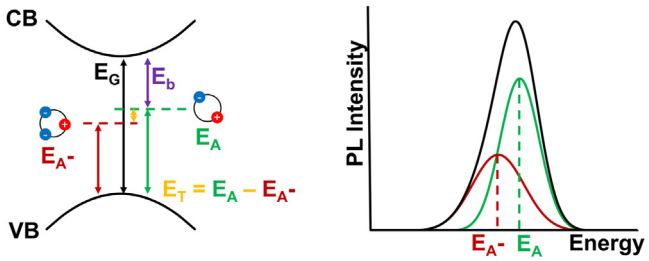

Fig. 14 Observed excitons and trions in TMDs and their relationship. When environmental dielectric screening is low, the electrons and holes in a TMD SL will be attracted to each other, forming a bound pair known as an exciton. The exciton binding energy (E_b) is the difference between the band gap (E_G) and the exciton energy measured via optical spectroscopy. E_b for TMDs is rather large and on the order of several 100 of meV. Additionally, three-particle states known as trions can form. The difference between E_A and E_A-is the trion binding energy (E_T), which is on the order of (20—40) meV. An archetypical photoluminescence spectrum is shown on the right with both the A and A^- peaks highlighted.

TMDs, depending on the amount of dielectric screening. In general, E_b increases with decreasing dielectric constant, and will be largest in the free-standing case due to the complete absence of dielectric screening (Lin et al., 2014; Kylänpää and Komsa, 2015). For example, E_b for MoS_2 on Al_2O_3 has been measured as ~240 meV, and ~420 meV for free-standing MoS_2 (Park et al., 2018; Yu et al., 2019). Unfortunately, the reported measured values for E_b can differ significantly, even for the same TMD on the same substrate at the same temperature. For example, measured E_b for WS_2 on SiO_2 have ranged from 0.32 to 0.83 eV, with the main challenge being an accurate bandgap determination (Chernikov et al., 2014; Hanbicki et al., 2015; Zhu et al., 2015). Regardless of the exact value of E_b, it requires several 1000 °C in temperature for the thermal excitation distribution k_BT to reach comparable values, thus making the physics of excitonic states and their associated optical response accessible at and even above room temperature.

TMDs can host many secondary excitonic species. The main primary exciton is often labeled the A exciton. Excitons can bind with free charge carriers to produce charged trions. Typically, the Mo/W-TMDs are n-type semiconductors. Therefore, an A exciton can bind with a free electron to produce a negatively charged A^- trion that is comprised of two electrons and one hole. **Fig. 14** shows a typical PL spectrum of a TMD, which consists of an A exciton and an A^- trion peak. The energy difference between the exciton (E_A) and trion (E_A^-) is called the trion binding energy and is about 40 meV (Jones et al., 2013; Lin et al., 2014). These peaks overlap at room temperature but become distinguishable at cryogenic conditions (Jones et al., 2013; Ajayi et al., 2017). The exact peak positions depend on the strain in the TMD, with compressive and tensile strains causing blue and red shifts, respectively. For example, in MoS_2, the A exciton peak position shifts by -110 meV/% of biaxial strain (Li et al., 2015). Thus, the exciton peak position can be used to compare strain between different films as well as mapping strain states across different locations within the same film. The relative intensities of the A and A^- peaks depend on the carrier density and can be manipulated by electrostatic or chemical doping. The peak intensity ratio can thus serve as a semi-quantitative measurement of doping levels in TMDs (Ross et al., 2013; Tebyetekerwa et al., 2020). Furthermore, an additional spin-split B exciton is often observed due to the above-discussed spin-orbit coupling. The separation between the A and B excitons is approximately equal to Δ_{VBM}. In the case of MoS_2, the relatively small Δ_{VBM} results in overlapping A and B exciton peaks. Defect-based nonradiative recombination typically suppresses the A exciton more than the B exciton. The intensity ratio between the A and B exciton peaks is therefore also used as a semi-quantitative measurement of defects in TMDs (McCreary et al., 2018). Additionally, more exotic excitonic species such as biexcitons and Ryberg excitons can be observed in cryogenic PL spectra (Chernikov et al., 2014; Hill et al., 2015; Stevens et al., 2018; Van der Donck et al., 2018). Lastly, interlayer excitons, i.e., excitons that couple electrons and holes across different SLs were found in TMDs, that show significantly enhanced lifetimes in vertical TMD heterostructures with staggered band alignments (Rivera et al., 2015, 2018; Kim et al., 2017b).

Growth of TMDs

Bulk growth—Chemical vapor transport

One of the oldest and most common ways to obtain SLs of TMD semiconductors is the mechanical exfoliation of bulk crystals. SL TMDs were first made by exfoliation from these crystals and are used both in fundamental research as well as for benchmarking synthesis methods due to their high crystal quality (Novoselov et al., 2005; Mak et al., 2010). Bulk TMD crystal growth is relatively equipment-light, mainly requiring a multizone furnace and ampoule sealing station. Bulk TMD crystals are often limited in size to about several cm^2 and take days to weeks to grow (Ubaldini et al., 2013; Ubaldini and Giannini, 2014; Ali et al., 2015; Pisoni et al., 2015; Ueno, 2015; Zhao et al., 2015a; Zhang et al., 2015; Edelberg et al., 2019; Patil et al., 2021; Liu et al., 2023c). The exfoliation process itself is rather labor intensive and offers low yield and reproducibility. Thus, while this method is suited for fundamental research, it is not readily scalable for potential industrial use.

The most common method for TMD bulk crystal growth is CVT. Here, a transport agent is used to reversibly form a volatile intermediate that supplies the transition metal to the growing crystals as sketched in **Fig. 15**A (Ubaldini et al., 2013; Ubaldini and Giannini, 2014; Pisoni et al., 2015; Ueno, 2015). Typically, a halogen such as Br_2 or I_2 serves at a transport agent. However, sometimes

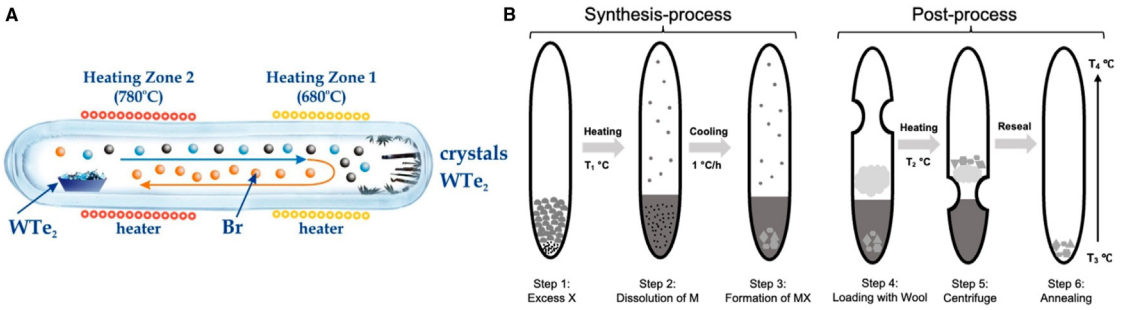

Fig. 15 Schematic of (A) CVT and (B) flux method growth for bulk TMD synthesis. In CVT, precursors and a transport agent (such as a halogen) are held in a quartz ampoule that is then placed in a two-zone tube furnace. The temperature gradient causes a change in chemical equilibrium which drives the growth process. Flux growth uses a molten solvent such as excess chalcogen as a growth media. (B) Reprinted with permission from open access reference (Buchkov et al., 2021). Reprinted with permission from reference (Liu et al., 2023c).

excess chalcogen or no added transport agent is used instead. For example, bulk crystals of MoS_2 can be grown from MoS_2 powder using Br_2 as a transport agent via the following reaction (Ueno, 2015):

$$MoS_2(s) + \frac{x}{2} Br_2(g) \Leftrightarrow MoBr_x(g) + S_n(g).$$

CVT is typically performed in a sealed quartz ampoule charged with precursor (often either powders of the different elements or the desired TMD itself) and a small amount of transport agent on one end (known as the source zone—right side of the ampoule in Fig. 15A), while crystal growth occurs at the other end (left side of the ampoule in Fig. 15A). The ampoule is then heated in a two-zone furnace that maintains the ends of the crucible at different temperatures. The generated temperature gradient results in a change in chemical equilibrium and drives convective transport through the tube. At the source zone, the forward reaction will be favored, generating the volatile intermediate species. These intermediates then move via diffusion and convection to the growth zone, where the reverse reaction takes place, forming crystals and regenerating the transport agent. The transport agent then returns to the source zone, allowing the cycle to continue (Ubaldini et al., 2013; Ubaldini and Giannini, 2014; Ueno, 2015).

One important complication with CVT is the selection of the transport agent. Br_2 and I_2 are liquid and solid at room temperature, respectively, and thus safer and easier to handle, although still toxic. Cl_2 in contrast is a highly toxic gas, which makes handling difficult (Ueno, 2015). However, Cl_2 is a better transport agent for certain metals such as Mo and Ta (Ubaldini and Giannini, 2014). One approach to circumvent this challenge is to use a chloride precursor that decomposes *in-situ*, including the intermediate chloride (e.g. $MoCl_5$) directly as a precursor (Ubaldini et al., 2013; Ubaldini and Giannini, 2014; Ueno, 2015). Another aspect a grower must consider is the effect of contamination. Halogens are a known dopant for many TMDs (Yang et al., 2014a; Pisoni et al., 2015). As a result, TMDs grown with halogen transport agents can be unintentionally doped, which may be undesirable. This can be avoided by using chalcogen as the transport agent or direct vapor transport in which no agent is used (Ueno, 2015).

A further method for bulk TMD crystal growth is flux growth, which uses a molten solvent as a growth media. Flux growth can be carried out with uniform temperature or a temperature gradient similar to CVT (Ali et al., 2015; Zhao et al., 2015b; Zhang et al., 2015; Cevallos et al., 2019; Edelberg et al., 2019; Patil et al., 2021; Liu et al., 2023c). Since the boiling point of sulfur is much lower compared to the growth temperature, secondary compounds are required. For example, MoS_2 and WS_2 have been grown using Zn and NaCl/CsCl as fluxes around 1000 °C (Zhang et al., 2015; Cevallos et al., 2019; Patil et al., 2021). In contrast, Se and Te can serve as fluxes themselves for the growth of WSe_2 and WTe_2, a technique sometimes referred to as "self-flux," with chalcogen-to-"metal" ratios ranging from ~20 to 100 (Ali et al., 2015; Zhao et al., 2015b; Edelberg et al., 2019; Liu et al., 2023c). Using self-flux growth, crystals with defect densities around $\sim 10^{11}$ cm^{-2} can be achieved, which is one to two orders of magnitude lower than common defect densities in CVT crystals (Edelberg et al., 2019). Raising the chalcogen-to-"metal" ratio and limiting Si and O contamination have yielded WSe_2 crystals with record-high room temperature mobilities of ~840 $cm^2/(Vs)$ in hBN-based SL transistors, which is near the phonon limit (Liu et al., 2023c).

Synthesis via metal film and liquid phase precursor transformation

Initial research on large-area TMD films utilized the chalcogen-assisted transformation of transition metal or metal-oxide films into TMD materials. The starting metal or metal-oxide layers, mostly Mo or MoO_3, were deposited via evaporation or sputtering prior to the transformation process. These films were subsequently sealed in a tube furnace with sulfur and converted into MoS_2 through high-temperature annealing steps (Lin et al., 2012). This approach produces uniform few-layer films over wafer-scale substrates. However, the films are typically polycrystalline with small grain sizes, and it is difficult to achieve a continuous TMD SL film without pinholes. Interestingly, by controlling the thickness of the metal seed layer, the TMD film can be made to grow in either a planar direction with its basal plane parallel to the substrate surface or vertically with its basal plane perpendicular to the substrate surface (Jung et al., 2014). The perpendicular orientation is of particular interest and benefit for catalytic applications that are based on edge facets as the active site since this orientation exposes a film surface that is solely comprised of SL cross-sections. An alternative approach to the synthesis of MoS_2, for example, is to use liquid phase transition metal precursors like $(NH_4)_2MoS_4$ or Na_2MoO_4

that are either dip- or spin-coated onto a substrate followed by sulfurization (Guan et al., 2023). The quality of TMD films obtained by liquid phase methods is, however, inferior compared to films prepared by exfoliation or CVD methods. Non-uniform spin coating can lead to regions of dense and sparse nucleation. In addition, it is difficult to achieve epitaxial growth of TMDs on single-crystal substrates using either metal or metal-oxide film deposition or liquid-phase precursors as a result of the limited surface adatom mobility available for these approaches.

Molecular beam epitaxy growth

MBE offers unparalleled control over film growth at the atomic level, making it an attractive approach for the synthesis of TMD single- and few-layer films. In addition, the MBE growth chamber can be connected to other ultra-high vacuum (UHV) chambers enabling sophisticated post-growth surface analysis such as angle-resolved photoemission spectroscopy (ARPES) or X-ray photoelectron spectroscopy (XPS) while maintaining a pristine surface. The UHV environment in the MBE technique, however, can present specific challenges for TMDs as the sticking coefficient of chalcogens on the growth surface is significantly reduced for substrate temperatures greater than 150 °C (Liu et al., 2021). As a result, TMD growth by MBE is often carried out using vdW surfaces such as highly oriented pyrolytic graphite (HOPG), epitaxial graphene, mica or other vdW materials that enable enhanced surface diffusion of adatoms at reduced temperatures (Lasek et al., 2021). The very low vapor pressure of transition metals precludes the use of typical thermal evaporation Knudsen effusion cells for the source supply and instead requires the use of an electron-beam evaporation source, that offers less flux stability especially in the very low flux range, is more complicated to handle due to the high power, and generates much more thermal radiation heat compared to simple Knudsen effusion cells. The much-increased thermal radiation from the electron-beam evaporator generates re-evaporation form otherwise cold reactor parts that can contaminate the growing film and can add a certain additional heat load to the sample growth (depending on the MBE growth chamber geometry, especially the throw-distance of the electron-beam evaporator device) that negatively impacts film formation. In addition, while Knudsen cells can be used for the chalcogen elements, chalcogens tend to evaporate as large molecules and clusters with low chemical reactivity rather than highly reactive single atoms. To mitigate this problem, hot-wall cracker sources can be employed whereby the thermally evaporated chalcogen clusters are dissociated as they pass through a tube that is heated to (800–900) °C. Despite these constraints, MBE-growth of a variety of TMDs like VSe_2, $TiSe_2$, $PtSe_2$, WSe_2, $MoSe_2$, etc. has been demonstrated, that enabled elaborate studies of their surface electronic band structure and bandgap characteristics via ARPES and scanning tunneling microscopy (STM) (Lasek et al., 2021). The high vapor pressure of sulfur results in S sublimation under UHV even at room temperature requiring careful control to isolate the sulfur source from the growth chamber. An alternative approach is to use evaporation of sulfur compounds such as SnS_2 or FeS_2 in a Knudsen cell which provides a reduced sulfur vapor pressure of sulfur but may introduce metal contaminants (Shimada et al., 1992; Pielić et al., 2020). As a result, reports about chalcogenide growth of S-containing compounds by MBE are very scarce.

Chemical vapor deposition

An important technique for TMD synthesis is CVD. In CVD, volatile gaseous precursors are supplied to the target substrate that react within the gas phase in proximity of the substrate to produce the film. The most common CVD technique for TMDs is powder CVD or oxide CVD, which uses transition metal oxide and elemental chalcogen powders as the precursors (Duan et al., 2014; Gong et al., 2014; Wang et al., 2014, 2020; Chen et al., 2016; Yu et al., 2017; Zhang et al., 2017; Cain et al., 2018; Zhou et al., 2018a). A typical CVD system is shown in **Fig. 16** and consists basically of a quartz tube in a tube furnace (Wang et al., 2014). The oxide powder (green circle of MoO_3 powder in **Fig. 16**) is placed within the hot zone (Furnace 2 in **Fig. 16**) of the furnace with the substrate (purple squares in **Fig. 16**) either located directly above or further downstream. The chalcogen powder is placed further upstream,

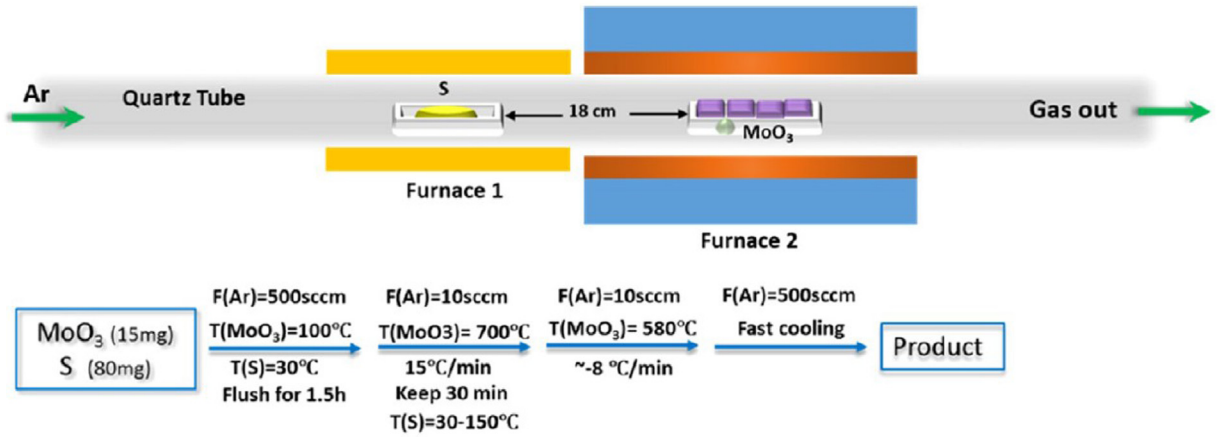

Fig. 16 Working principle of powder-based CVD. In this method, transition metal oxides and chalcogen powders are used as precursors. A typical system uses a tube furnace with the oxide at the hot zone near or upstream of the substrate and the chalcogen further upstream. When the system is heated to the growth temperature, the precursors evaporate and are transported by the carrier gas to the substrate. Reprinted with permission from reference (Wang et al., 2014).

where it is held at a lower temperature (the temperature of the chalcogen must be keep below its boiling point at the desired growth pressure) as represented by Furnace 1 in **Fig. 16**. During the growth, the oxide powder is heated to (700−900) °C to drive the evaporation of the oxide, which will then react with the chalcogen to produce the TMD thin film (Duan et al., 2014; Gong et al., 2014; Wang et al., 2014, 2020; Chen et al., 2016; Yu et al., 2017; Zhang et al., 2017; Cain et al., 2018; Zhou et al., 2018a). During growth, Ar or N_2 is flown through the system as a carrier gas. It should be pointed out here as a side note that H_2 as carrier gas should be avoided to prevent the formation of the highly toxic gases H_2S, H_2Se, and H_2Te. The vapor pressures of many transition metal oxides are, however, like for example in the case of Nb, too low to reliably supply and adequate "metal" flux for growth. It is therefore common to add an alkali-halide salt such as NaCl to the metal oxide. When heated, the alkali-halide and transition metal oxide powders react to form oxyhalide species with a lower melting point and higher vapor pressure than the parent oxide, which increases the rate of evaporation of the transition metal. This modification enables the growth of many TMD compounds that were otherwise impossible to synthesize with powder CVD (Zhou et al., 2018a). Using powder CVD, large, isolated domains on the order of 100s of μm as well as coalesced SLs can be grown both on amorphous and crystalline substrates (Chen et al., 2016; Yu et al., 2017; Wang et al., 2020).

It is easy and straightforward to expand this growth mechanism to various TMD heterostructures through carrying out multiple sequential growth runs (Gong et al., 2015). However, this method introduces thermal cycling and air exposure, which can be detrimental, especially when growing lateral heterostructures within one SL (Xie et al., 2018). Ideally, heterostructure growth should occur within a single growth run, which as a matter of fact can be achieved. If the difference in vapor pressures between the targeted oxides is large enough, heterostructures with distinct compositional regions can be produced just from the difference in evaporation in one single growth run. For example, because of the difference in vapor pressures, MoO_3 will evaporate at a higher rate than WO_3 at any set temperature, which enables the growth of MoX_2/WX_2 heterostructures (Gong et al., 2014; Huang et al., 2014). Furthermore, the geometry of the heterostructure can also be tuned by changing the growth temperature, with low temperatures favoring lateral heterostructures and higher temperatures favoring vertical heterostructures (Gong et al., 2014). By carefully tuning the growth temperature and ramp rate, it is possible to grow different vertical and lateral heterostructures of TMDs using such one-pot methods, which can be organized into time-temperature-architecture diagrams (Cain et al., 2018). One downside of one-pot methods is that the order of deposition is pre-set by the selected precursors, which limits the possible architectures that can be grown. Alternatively, the growth of different regions can be started and halted by adjusting the temperature of the different precursors individually, which can be achieved, for example, by moving the precursors using manipulators like quartz boats and rods attached to magnets (Duan et al., 2014).

Finally, MOCVD, which uses relatively volatile organometallic precursors to supply the transition metal, is a highly versatile technique to synthesize TMDs. Typically, carbonyl compounds like $Mo(CO)_6$ are used as the metal precursors, but other compounds such as bis(tert-butylimido)bis (dimethyl amido)-molybdenum ($C_{12}H_{30}N_4Mo$), and molybdenum dimethyl dithiocarbonate ($C_{20}H_{40}MoN_4S_8$) can be used as well (Kang et al., 2015; Liu et al., 2016a; Mun et al., 2016; Kalanyan et al., 2017; Kim et al., 2017c; Andrzejewski et al., 2018; Marx et al., 2018; Simonson et al., 2018; Zhang et al., 2018b; Kwak et al., 2019; Smets et al., 2019; Dodda et al., 2020; Mo et al., 2020; Xiang et al., 2020; Chowdhury et al., 2021; Chubarov et al., 2021; Hong et al., 2021; Park et al., 2021; Schaefer et al., 2021; Sebastian et al., 2021; Shi et al., 2021; Choi et al., 2022; Tang et al., 2022b; Zhu et al., 2023a). Similar to CVD, the chalcogen is supplied with either an organochalcogen such as diethyl sulfide ($C_4H_{10}S$) or a hydride such as H_2S (Kang et al., 2015; Mun et al., 2016; Kim et al., 2017a,c; Kalanyan et al., 2017; Simonson et al., 2018; Kwak et al., 2019; Smets et al., 2019; Dodda et al., 2020; Mo et al., 2020; Xiang et al., 2020; Chowdhury et al., 2021; Hong et al., 2021; Park et al., 2021; Schaefer et al., 2021; Sebastian et al., 2021; Shi et al., 2021; Choi et al., 2022). Due to their high vapor pressures, these precursors can be stored outside of the reactor chamber in gas cylinders or bubblers. During the growth, the flow rates of each precursor can be independently controlled, enabling precise control over the gas composition that can be varied over time. For example, multi-step growth methods for WSe_2 and WS_2 can involve a short nucleation stage followed by a long anneal under a chalcogen atmosphere to increase domain size and improve film crystallinity (Zhang et al., 2018b; Chubarov et al., 2021; Zhu et al., 2023a). Pulsed growths are possible as well but involve a systematic interpretation of the growth process, while pulsed growth-etch based techniques can use H_2O to remove carbon contaminants, and effectively improving crystallinity (Kalanyan et al., 2017; Cohen et al., 2020, 2023; Choi et al., 2022). Lateral and vertical heterostructure and superlattices can finally be achieved by changing the precursor during the growth (Xie et al., 2018; Herbig et al., 2021; Jin et al., 2021).

There are two major geometries for MOCVD reactors. In a hot-wall geometry as shown in **Fig. 17**A, heat is applied to the exterior walls of the reactor and diffuses inside to maintain the sample at the intended growth temperature. As a result, the gas phase within the reactor gets hot, which can cause undesired side reactions that lead to precursor decomposition and carbon contamination. This method, therefore, typically necessitates relatively low growth temperatures (<600 °C) for growth on amorphous substrates such as oxidized silicon (Kang et al., 2015; Park et al., 2021; Zhu et al., 2023b). To increase the domain size, seed promoters such as the already mentioned NaCl can be used in addition. The added NaCl can, however, negatively impact the photoluminescence response and electronic properties (Kim et al., 2017a; Zhang et al., 2018a; Zhu et al., 2023b). In a cold-wall system as sketched in **Fig. 17**B, the sample susceptor is heated via a radiofrequency (RF) induction coil or resistive heating element, while the reactor walls are maintained at a lower temperature. The lower overall gas temperature thus reduces gas phase reactions, which limits carbon contamination from organochalcogens and chalcogen buildup with the reactor when using hydrides. Cold-walled reactors are therefore better suited for high temperature (>700 °C) growths and with that better equipped for epitaxial growth on single-crystal substrates (Chubarov et al., 2021; Zhu et al., 2023a).

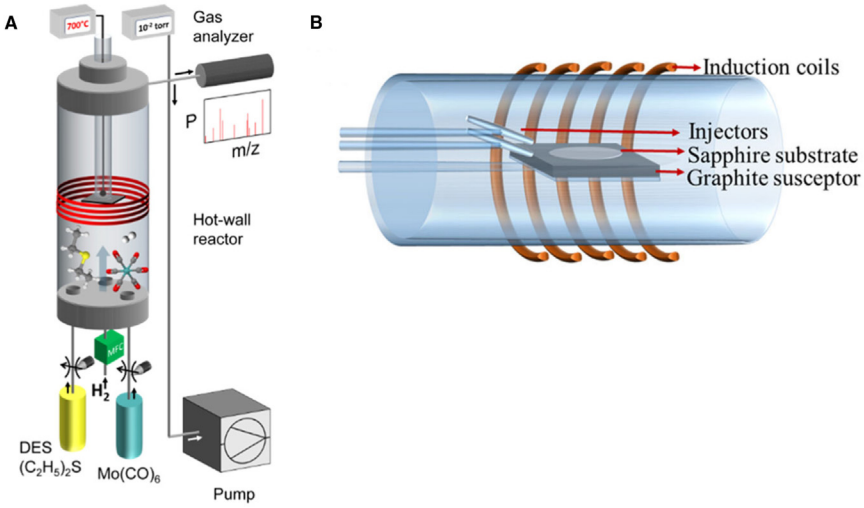

Fig. 17 Schematic of MOCVD growth using (A) hot-wall and (B) cold-wall reactor types. In MOCVD, the volatile precursors are stored outside of the reactor and are fed in during the growth. In a hot-walled reactor, the heat is supplied externally, while in a cold-wall geometry, the substrate is heated by induction. Hot-wall systems are typically used for lower temperature growths (often on amorphous substrates) while cold-wall systems are used for growth at high temperatures (often on crystalline substrates for epitaxy). Reprinted with permissions from references (Schaefer et al., 2021; Sebastian et al., 2021).

An inherent challenge in MOCVD growth is the selection of appropriate precursors. When using organochalcogens such as diethyl selenide ($C_4H_{10}Se$) and di-tert-butyl sulfide ($C_8H_{18}S$), graphitic carbon contamination were found for growths above the onset of pyrolysis, which can result in lower coverage and reduced crystallinity (Zhang et al., 2016b; Schaefer et al., 2021). Furthermore, such carbon contamination introduces midgap states that act as donors and suppress the PL response (Schaefer et al., 2021; Park et al., 2023b). This contamination can be reduced through the addition of H_2 as a carrier gas, which results in improved coverage and PL intensity. However, using a too high H_2 flow can reduce the growth rate (Schaefer et al., 2021). Alternatively, lowering the growth temperature can also reduce carbon contamination (Marx et al., 2018; Schaefer et al., 2021). Lowering the growth temperature, though, comes at the cost of increased domain density (Mortelmans et al., 2021). In contrast, hydrogen chalcogenides (also called chalcogen hydrides) like H_2S and H_2Se do not contain carbon and can thus produce cleaner films (Zhang et al., 2016b). These gases on the other hand are highly toxic and mandate expensive and elaborate monitoring and gas handling equipment. It should be noted here that H_2Se is known to readily decompose at common growth temperatures and leading to a Se build-up within the system (Pearson and Haugen, 1981).

Lastly, it should be mentioned, that a major drawback of any CVD process is its highly complex and complicated flow dynamics and gas phase reactions that are intrinsic features of the process itself, which strongly impact film morphology and quality. In powder CVD, the flux of the metal oxide is one of the main parameters affecting the growth, which in turn is strongly affected by the geometry and flow dynamics of the system in use. For example, by placing the substrate face down above the oxide precursors, large, isolated domains form, while placing the substrate downstream facing up results in many small domains. Placing the substrate downstream oriented vertically and with that perpendicular to the gas flow results in vertical out-of-plane-oriented growth. The exact mechanism behind this is not well understood but is likely due to changes in the metal flux, which can change both the nucleation density as well as the growth direction (Zhang et al., 2017). Multiscale modeling of MOCVD growths ranging from the molecular to the macroscale can be used to help understand gas phase reactions and fluid flows within the reactor, and assist with the selection of growth parameters (Dhar et al., 2016; Xuan et al., 2019; Ghorai and Govind Rajan, 2024).

Epitaxy on Al_2O_3(0001)

Al_2O_3

One of the commonly used, economical and well-studied substrates for epitaxial growth of TMD SLs is Al_2O_3, also referred to as sapphire. Sapphire is commonly used in nitride epitaxy and wafers are commercially available at relatively low costs. Additionally, Sapphire is chemically stable under chalcogen exposure and, unlike for example Si, it will not etch (Rai-Choudhury and Noreika, 1969). The pseudo-hexagonal unit cell of Al_2O_3 is shown in **Fig. 18**A (Wang et al., 2016b). Each unit cell contains 6 oxygen layers and 6 double Al layers, resulting in a total height of 1.298 nm (Lee and Lagerlof, 1985; Wang et al., 2016b). Although the *m*-, *r*- and *a*-planes of sapphire have been used for the growth of TMD films, the prior literature is overwhelmingly focused on the *c*-plane (Ma et al., 2020; Peters et al., 2020). The surface of *c*-plane sapphire can be O, Al, or Al—Al terminated. Each of these surfaces displays a 3-fold rotational symmetry, thus fulfilling the symmetry requirement outlined before (Wang et al., 2016b). Additionally, sapphire has an *a* lattice parameter of 0.475 nm, which results in about 50 % lattice mismatch when compared to the group-6 2H TMDs (e.g.

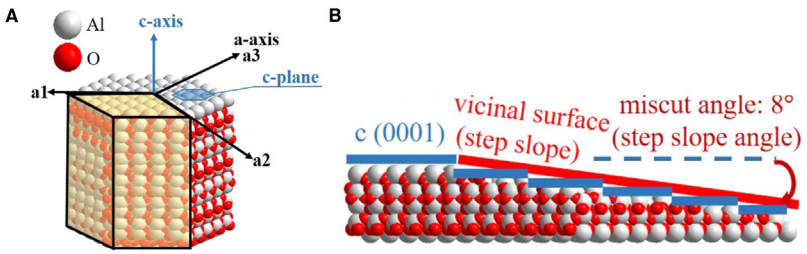

Fig. 18 The Al_2O_3 crystal structure and its surfaces. (A) A unit cell of Al_2O_3 consists of 6 alternating layers of O and Al. The c-plane is normal to the c-axis and possesses 3-fold rotational symmetry, satisfying the symmetry requirement for unidirectional epitaxy. (B) The sapphire can be miscut to form step terraces and edges. The size and density of the terraces are defined by the miscut angle, while the step termination is defined by the miscut direction. Reprinted with permission from reference (Wang et al., 2016a,b,c).

MoS_2 has a lattice parameter of 0.316 nm) (Schönfeld et al., 1983; Lee and Lagerlof, 1985). In conventional epitaxy, this lattice mismatch would be too large to achieve good film growth. However, since this is a quasi-vdW system, a commensurate lattice match of 3 unit cells of TMD to 2 unit cells of Al_2O_3 can be considered, which for MoS_2 results in 0.2 % tensile strain based on the room temperature lattice parameters.

Sapphire is often found with a miscut that produces step terraces and step edges on the surface that can serve as nucleation sites, as show in **Fig. 18**B. The miscut is defined by two parameters. The miscut angle determines the slope of the step terraces and is measured with respect to the flat terrace surface, while the miscut direction is defined as the direction normal to the terrace edge (Wang et al., 2016b). For example, the steps will be rotated by 90° when the miscut is to the *m*-axis versus the *a*-axis (Wang et al., 2016b; Li et al., 2021b). Moreover, the miscut direction lowers the global rotational symmetry of the surface, which can enable unidirectional growth (Grundmann, 2011; Dong et al., 2020b; Fu et al., 2023). However, there are several complications that the miscut imposes. First, as mentioned above, *c*-plane sapphire can be O, Al, or Al−Al terminated. All three terminations can be present on miscut sapphire. Additionally, there are 5 distinct step compositions based on the exact terminations of the top and bottom steps. The exact type, sequence and periodicity of the step edges is defined by the miscut direction, while the terrace width (and its reciprocal, the step density) are defined by the miscut angle, with higher miscuts resulting in a higher density of narrower terraces (Wang et al., 2016b).

Additionally, the step structure and surface chemistry of sapphire can be modified by annealing under different conditions. When annealed at low temperatures, i.e., 600−900 °C, O and H_2O desorb from the sapphire, resulting in an Al-terminated surface (Tsuda et al., 2003; Park et al., 2023a). At higher temperatures, the sapphire surface can etch, with different step edges merging to form taller step edges in a process known as step bunching. When annealed in an oxidizing atmosphere of air or oxygen, the etching and bunching process produces large, straight, well-aligned steps with wide terraces, which can be useful if the as-received sapphire does not have well-defined step edges. In contrast, when annealed under a reducing atmosphere such as H_2, the steps etch jaggedly, producing a surface with poorly aligned steps and non-uniform step bunching (Curiotto and Chatain, 2009). Furthermore, when annealed at or above 1200 °C, a new $(\sqrt{31} \times \sqrt{31})$R9 Al reconstruction that is rotated by 30° is formed (Mortelmans et al., 2019).

TMD growth on Al_2O_3

Due to their atomically thin nature, the growth and epitaxy of TMDs on sapphire is strongly affected by the sapphire surface and thus can be impacted by many of the variables mentioned above. There are two primary epitaxial orientations for TMDs on *c*-plane sapphire. In the first orientation, the *a*-axes ($[11\bar{2}0]$) and *m*-axes ($[1\bar{1}00]$) of the TMD and sapphire are parallel with respect to each other ($[11\bar{2}0]MX_2(0001) \parallel [11\bar{2}0]Al_2O_3(0001)$ or $[1\bar{1}00]MX_2(0001) \parallel [1\bar{1}00]Al_2O_3(0001)$). Thus, the TMD is said to be orientated by 0° and 60° with respect to the axes of the Al_2O_3 substrate. Due to the difference in lattice parameter, the resulting super-cell consists of $(3 \times 3)MX_2$ unit cells on a $(2 \times 2)Al_2O_3$ unit cell depicted in **Fig. 19**A, which for MoS_2 and WSe_2 result in 0.2 % tensile strain and 4 % compressive strain, respectively based on room-temperature lattice constants. In the second orientation, the *a*-axis of the TMD is parallel to the *m*-axis of the sapphire and vice versa (i.e., $[11\bar{2}0]MX_2(0001) \parallel [1\bar{1}00]Al_2O_3(0001)$). This epitaxy (often denoted as ± 30°) necessitates a $(5 \times 5)MX_2$ to $(3 \times 3)Al_2O_3$ super cell as shown in **Fig. 19**B. **Fig. 19**C shows the underlying sapphire lattice for clarity. Unlike in 0° or 60° epitaxy, the lattice mismatch is higher for the ± 30° orientation, resulting in a 4 % tensile strain for MoS_2 and 9 % compressive strain for WSe_2 (Mortelmans et al., 2019; Lai et al., 2021). DFT calculations indicate that, for flat *c*-plane sapphire without steps, the ± 30° orientations are energetically favored on O- and Se-terminated surfaces, while 0° or 60° orientations are favored on Al-terminated surfaces. In the case of O- and Se-terminations, the energy difference between the ± 30° and 0° or 60° orientations ranges on the order of 10 meV, i.e., a relatively small value, and thus the epitaxial orientation may be established or influenced by other effects (Zhu et al., 2023a; Park et al., 2023a).

There are several proposed mechanisms for TMD epitaxy. The first is that the step edges in the sapphire are the primary driver for nucleation. This view is supported by the fact that TMDs typically nucleate along step edges with one edge of the TMD aligned with the step. Zhu et al. found that WSe_2 can nucleate along either the top or bottom of the sapphire step edge when grown at 200 and 700 Torr, respectively (Zhu et al., 2023a). Simulations found replacing O with Se is most energetically unfavorable along the

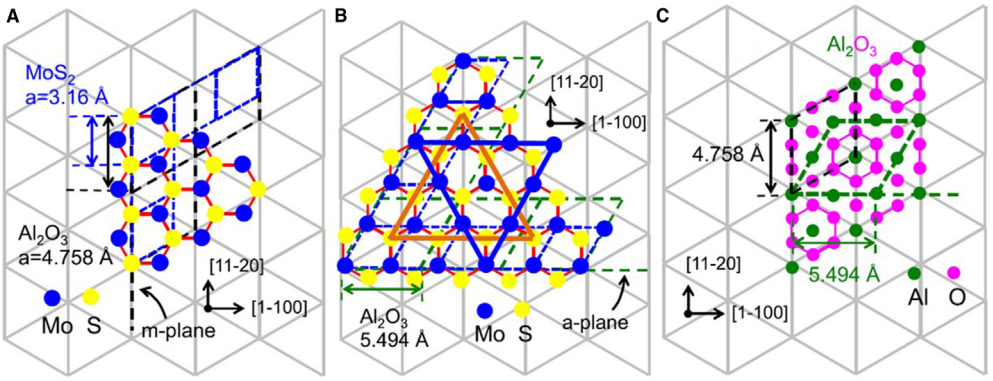

Fig. 19 TMDs grow on sapphire in two main epitaxial orientations. (A) When the a-axis of the sapphire and TMD are parallel, the TMD is rotated by 0° or 60° with respect to the sapphire. The resulting super-cell consists of $(3 \times 3)MX_2$ unit cells on $(2 \times 2)Al_2O_3$ unit cells (see highlighted rhombi). (B) When the a-axis of the TMD is parallel to the m-axis of the sapphire and vice-versa, the TMD is rotated by ± 30° with respect to the sapphire. This results in a $(5 \times 5)MX_2$ to $(3 \times 3)Al_2O_3$ super cell. (C) The sapphire surface without the TMD for clarity. Reprinted with permission from reference (Lai et al., 2021).

bottom of the step and that this remnant O inhibits nucleation along the bottom of the step. By increasing the reactor pressure, this remnant O can be more effectively removed, changing the preferred location for nucleation (Zhu et al., 2023a). Furthermore, Shi et al. found that MoS_2 grown on miscut sapphire has more uniform electrical properties as measured by conductive AFM and device statistics when compared to substrates with small, unintentional miscuts (Shi et al., 2021).

However, there are reports of TMD growth where the epitaxial orientation does not match what would be expected from the step-edge hypothesis. For example, Li et al. found that, when using powder CVD, MoS_2 grows with ± 30° epitaxy, regardless of whether the sapphire was miscut towards the *m*-axis or the *a*-axis, what should have resulted in 0° or 60° and ± 30° epitaxy if step-edge driven, respectively (Li et al., 2021b). However, they achieved nearly complete unidirectionality when using the *a*-axis miscut, which they attribute to a broken degeneracy in the binding between the sapphire steps and the MoS_2 edges (Li et al., 2021b). Fu et al. claimed that uniformly terminated sapphire with a single orientation rather than step edges are the primary cause of unidirectional growth, which can be achieved by tuning the miscut angle and reconstruction annealing conditions (Fu et al., 2023). Lai et al. demonstrated that "metal" and chalcogen rich growths favor 0° or 60° and ± 30° epitaxy, respectively (Lai et al., 2021). Furthermore, the sapphire reconstruction can strongly impact TMD epitaxy. For example, when growing WSe_2 with MBE, Mortelmans et al. report that using (1×1) reconstructed sapphire results in 0° or 60° epitaxy. In contrast, using $(\sqrt{31} \times \sqrt{31})R9$ reconstructed sapphire results in primarily ± 30° epitaxy, with some WSe_2 domains following the 0° or 60° epitaxy. Furthermore, the amount of the secondary epitaxy decreased with increasing the pre-anneal temperature used to produce the reconstruction. These results suggest that TMD epitaxy is established based on conditions of the sapphire surface rather than based on the bulk (Mortelmans et al., 2019). Furthermore, there have been reports of chalcogen and oxide buffer layers at the interface between the sapphire surface and TMD SL whose nature and importance is not yet well understood (Lin et al., 2018; Xiang et al., 2020; Cohen et al., 2023; Zhu et al., 2023a; Li et al., 2024).

Another aspect to consider is the effect of growth temperature. In general, higher temperatures typically favor lower domain densities, which in turn results in less grain boundaries (Mortelmans et al., 2020a, 2021). However, when growing MoS_2 on $(\sqrt{31} \times \sqrt{31})R9$ reconstructed sapphire via MOCVD, there are instances when lower growth temperatures results in ± 30° epitaxy while higher temperatures favor 0° or 60° (Mo et al., 2020; Mortelmans et al., 2020a). RHEED measurements indicate that exposure to H_2S converts the $(\sqrt{31} \times \sqrt{31})R9$ reconstruction to a (1×1) surface (Mo et al., 2020). For MoS_2 grown on unreconstructed sapphire by MOCVD, Chen et al. found that increasing growth temperature for MoS_2 from 900 °C to 1000 °C reduced the areal density of low angle grain boundaries from 50 % to 5 % but increased the coverage of high angle grain boundaries from 2 % to 10 % (Chen et al., 2024). As a result, the electronic properties were optimized using an intermediate growth temperature of 950 °C. Chubarov et al. found that by increasing the growth temperature for a single step growth of WS_2 from 850 °C to 1000 °C the number of distinct epitaxial orientations increased as measured by in-plane XRD, which the author hypothesized to be the result of modification of the sapphire step structure (Chubarov et al., 2021). However, by implementing a multi-step growth in which the film is nucleated at 850 °C and lateral grown is carried out at 1000 °C, films retain the 0° or 60° orientation of the 850 °C single-step growth (Chubarov et al., 2021). Additionally, the multi-step growth reduced the full-width at half-maximum (FWHM) of the in-plane XRD φ-scan from 1.13° to 0.09°, i.e., reducing the in-plane twist in the SL of WS_2 (Chubarov et al., 2021). In summary, the effect of growth temperature is multifaceted and must be carefully tuned, and most likely requires implementing multiple different temperatures for different stages of the growth to achieve films with optimized properties.

Summary and outlook

Several key areas emerge as promising avenues for further exploration and advancement of TMD synthesis technology, as highlighted in **Fig. 20**. This includes substitutional doping to modulate the Fermi level and carrier density, the synthesis of heterostructures including Janus SLs and twisted bilayers, selective area growth, *in-situ* monitoring during thin film synthesis and the development of multi-wafer deposition systems. These areas are aimed at improving controllability, expanding the versatility of TMD synthesis and tailoring film properties for scientific studies and key applications.

The controlled incorporation of dopant elements into the TMD lattice emerges as a crucial strategy to modulate the electronic and catalytic properties of TMDs (**Fig. 20**A). The addition of dopants to semiconducting TMDs such as MoS_2 and WSe_2 to modulate carrier type (n-type vs. p-type) and concentration is of key importance for electronic devices such as FETs whose performance is constrained by the Schottky barrier inherent in the metal-to-2D semiconductor contact (Das et al., 2021). While surface charge transfer doping has been employed to modulate carrier concentration, substitutional doping is preferred as a more robust approach (Loh et al., 2021). Substitutional doping of group-V (e.g. nitrogen and phosphorus) and group-VII (e.g. chlorine) elements on the chalcogen sublattice has been pursued for p-type and n-type doping, respectively. Alternatively, metals such as vanadium and niobium have been investigated as substitutional p-type dopants on the transition metal sublattice along with Re and other metals for n-type doping (Younas et al., 2023). While a variety of dopants have been incorporated in TMD films both *in-situ* during growth and via post-growth processing, several challenges remain. The reduced dielectric screening in SL TMDs significantly increases the ionization energy of dopants (Noh et al., 2015). Consequently, dopant concentrations on the order of a few percent or more are required. The high doping levels can result in increased grain boundaries and other defects in films grown by CVD or MBE when added during growth (Lin et al., 2021). Post-growth doping involves plasma irradiation and/or thermal annealing to create chalcogen vacancies which are then substituted by dopants. Careful optimization of this process is required to minimize defects.

Janus SLs in TMDs refer to a type of asymmetrically structured SL where two distinct chalcogen atoms (e.g. sulfur and selenium) occupy opposite sides of the transition metal atom within the same layer, as shown in **Fig. 20**B. This effectively leads to symmetry breaking and thus unique properties such as out-of-plane piezoelectric polarization and a strong Rashba effect (Zhang et al., 2020). Janus structures were initially synthesized using a hydrogen plasma to strip off the top layer of chalcogen atoms and replace them with hydrogen which can then be substituted with a different chalcogen atom via thermal annealing (Lu et al., 2017; Zhang et al., 2017). Synthesis approaches for TMD Janus SLs present challenges due to the precise control required to maintain structural integrity and ensure uniformity. The recent use of *real-time* Raman and photoluminescence spectroscopy for process monitoring has enabled improved control and insights into this transformation process (Harris et al., 2023).

Selected area growth (SAG) is of particular interest for device applications of TMDs to enable precise control over the location and spatial distribution of the layers as well as their doping level. Several approaches have been pursued for SAG, such as the use of patterned metal seeds that serve as TMD nucleation sites, and the use of patterned substrates whereby TMD growth occurs only in the window openings (Wang et al., 2016c; Kim et al., 2023). While both approaches lead to site selective nucleation, uniformity over large areas is challenging. Limiting the growth to a single nucleus is difficult too. Consequently, the resulting islands may contain multiple orientations and defects. While initial results have been promising, challenges remain to develop SAG as a robust approach for deterministic growth of TMDs. Opportunities exist to engineer seeds, masks, precursors, and growth conditions to optimize selectivity and achieve single domain nucleation across wafer-scale areas. Selective re-growth of multi-layer doped source and/or drain regions is also of significant interest as a route to reduce contact resistance in TMD FETs.

The synthesis of TMD multilayers and heterostructures, including twisted bilayers, holds significant promise for exploring emergent phenomena and novel device functionalities. In-plane TMD heterostructures have been synthesized by CVD by sequential modulation of the metal or chalcogen source (Neupane et al., 2019). In-plane modulation of composition has been demonstrated on the transition metal (e.g. MoS_2/WS_2) and chalcogen (e.g. WSe_2/WS_2) site but this has largely been limited to individual triangular TMD domains. Extension of this approach to coalesced films where the in-plane composition is modulated periodically over a large area remains an area for future exploration. Most studies thus far involving TMD vertical heterostructures and twisted bilayers have utilized samples formed by exfoliation, layer transfer and stacking. In general, the formation of vertical heterostructures *in-situ*

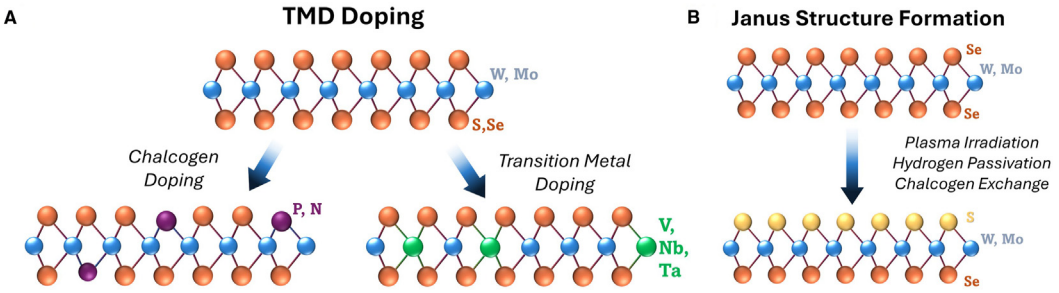

Fig. 20 Future major avenues for TMD research. (A) Substitutional doping of TMDs could be used to control carrier type and density, which is key for the development of high-performance electronic devices. (B) In Janus TMDs, two different chalcogens occupy the different sides of the SL. This structure gives rise to unique properties such as out-of-plane polarization and a strong Rashba effect.

is favored for combinations of TMDs with dissimilar crystal structures whereas lateral heterostructures are obtained when the crystal structures are similar (Liang et al., 2022). Significant opportunities exist to advance the synthesis of heterostructures and twisted bilayers using large area films via control of defects in the underlying SL which then serve as sites for bilayer nucleation with controlled orientation and via control of the step structure of the underlying substrate as has been demonstrated for bilayer MoS_2 epitaxy (Liu et al., 2022).

As the field of TMD synthesis moves forward and matures towards manufacturing, key advances will be required to improve scalability and reproducibility. Achieving uniform SL films that are < 1 nm thick over wafer sizes as large as 150 mm or 300 mm will require an unprecedented level of process control. This will require the development of *in-situ* growth monitoring methods that can measure sub-SL surface coverages to track layer-by-layer growth. Epitaxial growth technologies such as MOCVD and MBE which are used for commercial manufacturing of III-V epi-wafers are likely to be best suited to meet these requirements given their ability to tightly control precursor flux, monitor and control other process parameters (e.g. temperature, gas flow rates) and facilitate *in-situ* monitoring using electron diffraction and optical reflectance methods. Combining *real-time* process data monitoring with machine learning and other data science techniques presents new pathways for process stability beyond what is currently possible with statistical process control methods. Ultimately the development of multi-wafer deposition tools enabling high-throughput synthesis of TMDs will be required for industrial applications. The convergence of advances in doping techniques, heterostructure synthesis, selective area growth, *in-situ* monitoring, machine learning, data science and multi-wafer deposition tools holds the promise of ushering in a new era of tailored TMD materials with unprecedented functionalities and performance characteristics.

2D layered chalcogenide-based topological insulators

Introduction

The relevance of topology to the electronic states of materials was first grasped in relation to thin superconductors and superfluids in the 2D limit and to the integer quantum Hall effect (QHE) in 2D electron gases. The work of Thouless, Haldane and Kosterlitz in developing the theoretical framework of topological phases in condensed matter was awarded with the 2016 Nobel Prize in physics (Thouless et al., 1982; Haldane, 1988). Thouless developed the theory that explained the quantized values of the Hall conductivity in the QHE. Using the Berry curvature of the wavefunctions in the Landau levels of the QHE, he showed that the Hall conductivity is defined by a topological invariant known in mathematics as the first Chern number, which has an integer value of 1 for each Landau level (Thouless et al., 1982). The question of whether such a quantized state could occur without the external magnetic field needed for the QHE was addressed by Haldane. He showed that on a hexagonal lattice with a staggered magnetic field that fluctuated from site to site, a topological state that did not involve Landau levels but had a zero net magnetization, where time-reversal symmetry was broken, could be created (Haldane, 1988). How such an atomically fluctuating internal field could be created seemed unrealistic until Kane and Mele pointed out that spin-orbit coupling could play such a role, in what they termed the quantum spin Hall effect (QSHE) (Kane and Mele, 2005). Spin-orbit coupling does not break time-reversal symmetry, so it results in no Hall conductance, but it does act like an internal field with opposite signs for opposite spins. The quantum spin Hall state is like two counter propagating quantum hall edge states whose Hall conductances cancel. Simplistically, this is the origin of the so-called "spin-momentum locking" of topological insulators, where the electron spin polarization is linked to the electron flow direction. Quantum spin hall materials are also known as 2D topological insulators exhibiting 1D topological edge states that propagate around the 2D edge of the sample. As the spin of each edge state is orthogonal, backscattering is not allowed. The first demonstration of QSHE was in MBE grown HgTe/CdTe quantum wells (Bernevig et al., 2006; König et al., 2007). Since then, it has also been shown in several TMD materials (Qian et al., 2014; Wu et al., 2018; Ma et al., 2019).

The 3D topological insulators generalize the 1D edge states of the QSHE into 2D surface states that exist on all surfaces of the material in contact with a topologically trivial material, including the vacuum. The surface states of 3D TIs have a linear dispersion that sweeps out a cone in momentum space, crossing at a point called the Dirac point. The semimetal alloy $Bi_{1-x}Sb_x$ was the first 3D topological insulator identified (Hsieh et al., 2008, 2009b). Shortly afterward the binary compounds Bi_2Se_3, Bi_2Te_3 and Sb_2Te_3 were identified as TI materials and have become the most widely studied TIs to date. Bi_2Se_3 is the easiest to grow on the widest range of substrates and has the largest bulk band gap of ~300 meV (Zhang et al., 2009). Unfortunately, it is also prone to intrinsic defects that cause the Fermi energy (E_F) to lie in the bulk conduction band. Nevertheless, it was found to be one of the best material candidates to host giant spin-orbit torques (Mellnik et al., 2014). The ternary compound $(Bi_{1-x}Sb_x)_2Te_3$ (often referred to as BST) can be grown by carefully balancing the ratio of Bi to Sb to cause the defects to compensate each other so E_F can be pushed into the bulk band gap near the surface state Dirac point. Doping with magnetic elements such as Cr and V also leads to robust ferromagnetism in Sb_2Te_3, which was crucial to the experimental observation of the quantum anomalous Hall effect (QAHE), in Cr-$(Bi,Sb)_2Te_3$ (Chang et al., 2013b). Although the system is very different, the QAHE in Cr-$(Bi,Sb)_2Te_3$ is a realization of Haldane's idea, where no external field is needed because time reversal symmetry is broken by the internal ferromagnetism of the crystal. Since then, the stochiometric magnetic TI $MnBi_2Te_4$ has demonstrated that reducing disorder is an effective pathway to increasing the temperature at which the QAHE can be observed (Deng et al., 2021).

This section will focus on Bi_2Se_3, Bi_2Te_3, Sb_2Te_3, and their alloys. Several other topological materials have been identified which will not be dealt with in detail because they are not 2D layered chalcogenide materials. SnTe, which was among the first epitaxial materials grown by a molecular beam, is among the class of materials now called topological crystalline insulators (TCI) where

a crystal symmetry is crucial to its non-trivial topology (Zemel et al., 1965; Hsieh et al., 2012; Tanaka et al., 2012). $Bi_{1-x}Sb_x$ has seen renewed interest in spintronics studies as a spin-orbit torque material (Khang et al., 2018; Chi et al., 2020). New classes of topological materials have also been found such as Dirac and Weyl semimetals, which have massless linear dispersing bands in their bulk band structure, that have been subject to recent reviews (Jia et al., 2016; Armitage et al., 2018; Narang et al., 2021).

Properties of TIs

Long before they were identified as topological insulators, Bi_2Se_3, Bi_2Te_3, Sb_2Te_3 and their alloys were known to be good thermoelectric materials. This is not accidental, thermoelectrics typically are small band gap materials with heavy atoms and features of the topological band structure can be beneficial for thermoelectric performance (Shi et al., 2015). The heavy atoms lead to large spin-orbit coupling in the material, which in the case of TIs is large enough to cause a band inversion. Using Bi_2Se_3 as an example, in the absence of spin orbit coupling, the chemical bonding and crystal field splitting would lead to a conduction band derived primarily from Bi orbitals and the valence band from Se orbitals with different parities. However, when spin orbit is included, its effect is large enough at high symmetry points, such as the Γ point, that the energetic ordering is reversed and the electronic states and parities that would typically form the conduction and valence bands at the Γ point switch as demonstrated in **Fig. 21**B and C (Zhang et al., 2009). The topological surface states can be viewed as a consequence of the inversion being undone at the interface with a topologically trivial material (like vacuum), where the states must cross going from inverted to non-inverted ordering. Unlike some TIs that have multiple surface states (for example, on the $Bi_{1-x}Sb_x$ (110) surface) (Zhu et al., 2013), in the Bi/Sb-sesquichalcogenides, the topological surface states form a single Dirac cone centered at the Γ point that is protected by time-reversal and inversion symmetry. This simple structure makes them ideal for studying the properties of the topological surface states.

Among them, Bi_2Se_3 has the largest bulk band gap at ~300 meV, while the bandgaps of Bi_2Te_3 and Sb_2Te_3 are only about half of that. Additionally, it is found that the Dirac point of the Bi_2Se_3 is near the middle of the bulk band gap (see **Fig. 21**D), while it is beneath the valence band edge for Bi_2Te_3 (Chen et al., 2009; Hsieh et al., 2009a). This would seem to make Bi_2Se_3 an ideal material to study topological properties except that the already mentioned defects always push the Fermi energy up into the conduction band. Consequently, isolating the surface state conductance from the parasitic parallel conduction channel through the bulk is difficult. Bi_2Te_3 is typically n-type, while the dominant defects in Sb_2Te_3 cause it to be p-type. However, due to the opposite effect of the dominant defects in those two materials, the Fermi energy can be controlled and placed near the Dirac point by the Bi/Sb ratio in the ternary compound $(Bi_{1-x}Sb_x)_2Te_3$. Additionally, it was found that the Dirac point moves above the valence band edge for a Sb concentration $x > 0.5$ (Zhang et al., 2011). Because of this, the TI $(Bi_{1-x}Sb_x)_2Te_3$ has been synthesized most widely by thin film growth methods such as MBE, whereas it is extremely challenging to control the stoichiometry in bulk growth techniques (Kushwaha et al., 2016; Heremans et al., 2017).

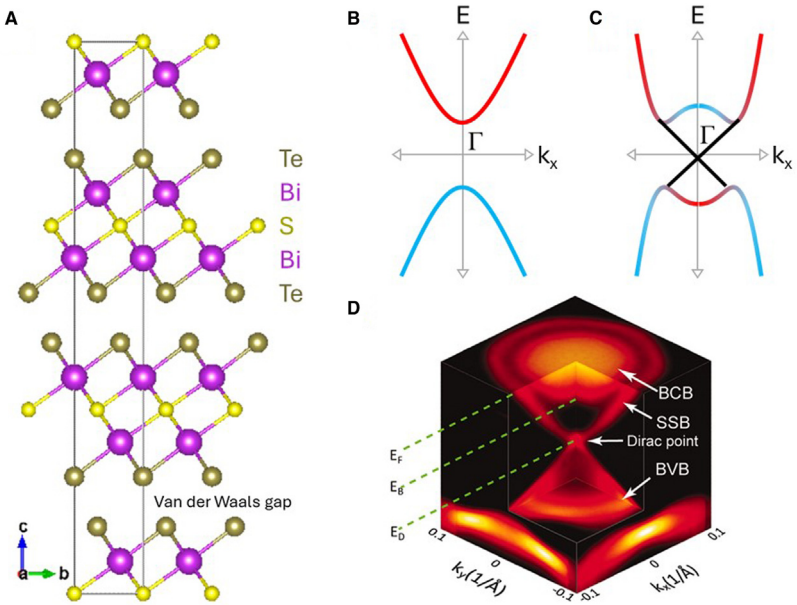

Fig. 21 The layered Bi_2Te_2S system and fundamentals of topology. (A) Crystal structure of tetradymite Bi_2Te_2S showing the layered structure of five-atomic layers per SL with a van der Waals gap between them. S sits primarily at the central chalcogen site while Te sits primarily at the outer chalcogen sites. (B) Typical trivial band structure of a semiconductor with a conduction band (red) and valence band (blue). (C) Inverted band structure of a TI where the band character near the high symmetry Γ point arises from states that would typically form the opposite band. The topological surface state that crosses the bulk bandgap is shown in black. (D) ARPES bandmap of the electronic structure of Bi_2Se_3 showing the bulk conduction band (BCB), bulk valence band (BVB) and the surface state bands (SSB). Reprinted with permission from reference (Cha et al., 2010).

The Dirac cone of the surface states can be described by an effective Hamiltonian of the form;

$$H = \hbar v_f \left(\sigma^x k_y - \sigma^y k_x\right),$$

where the z direction is out of plane. From this, the spin lies in the plane and is always perpendicular to the momentum. This forms a helical spin texture in momentum space on both the top and bottom surfaces that rotates in a left-handed sense around the cone above the Dirac point and reverses at energies below it. This is often referred to as "spin-momentum locking" but in the presence of spin-orbit coupling it is the total angular momentum $\overrightarrow{J} = \overrightarrow{S} + \overrightarrow{L}$ that is a good quantum number. The surface states therefore also have an orbital texture (Zhang et al., 2013a). From the spin texture, direct backscattering across the Dirac cone is forbidden, like in the QSH, but scattering to other k vectors is allowed. Additionally, Bi_2Te_3 particularly shows a pronounced hexagonal warping of the Dirac cone near the conduction band edge that is not captured in this simple Hamiltonian.

The Dirac point is located at the Γ point in momentum space and is protected by inversion symmetry and time-reversal symmetry. However, it is possible to open a gap at the Dirac point by either breaking inversion symmetry through thickness tuning or by breaking time-reversal symmetry by introducing magnetism. At thicknesses of three SLs or less for Bi_2Se_3, the surface states on the top and bottom surfaces hybridize opening a gap at the Dirac point (He et al., 2010). Breaking time-reversal by introducing magnetic order can also gap out the Dirac point, which is the most widely pursued avenue that leads to a number of interesting effects as will be discussed in the following subsection.

Magnetism and TIs

Breaking the time-reversal symmetry of topological insulators by introducing ferromagnetic order can lead to exotic quantum phenomena including the QAHE and the topological magnetoelectric effect (TME) (Chang et al., 2013b, 2015; Mogi et al., 2017; Xiao et al., 2018). One approach to break the time-reversal symmetry in TIs is doping with magnetic ions. Based on the density functional theory calculation, several transition metals including Cr, V, Mn, and Fe can be used as magnetic dopants to form perpendicular magnetic anisotropy (Zhang et al., 2012b). This led to the experimental realization of QAHE in Cr or V doped $(Bi,Sb)_2Te_3$ thin films.

There are three conditions for realizing the QAHE. First, the system should have long-range ferromagnetic order with perpendicular magnetic anisotropy. Second, the system should be thin enough to localize the dissipative bulk and surface states. Third, the Fermi energy should be tuned into the magnetic gap so only the chiral edge states are conducting. Theoretically, breaking time reversal symmetry with an out-of-plane field contributes a half quanta of Hall conductance $\sigma_{xy} = \pm\frac{1}{2}\frac{e^2}{h}$ for each surface, where the sign depends on the direction of the magnetization. When the magnetization directions are aligned the $\frac{e^2}{h}$ quantization of the QAHE is observed, but when they are anti-aligned, they cancel and the Hall and longitudinal conductances are both zero. In Cr-doped-$(Bi_{1-x}Sb_x)_2Te_3$/$(Bi_{1-x}Sb_x)_2Te_3$/V-doped-$(Bi_{1-x}Sb_x)_2Te_3$ heterostructures and in $MnBi_2Te_4$, conditions can be achieved such that the top and bottom magnetic layers are in the antiparallel magnetization configuration. In this case, all the surface states are gapped while the bulk states still obey the time-reversal symmetry. In this scenario, the zero Hall resistance and conductance plateaus can be observed, known as the axion insulator state (Mogi et al., 2017; Xiao et al., 2018).

Chiral magnetic textures such as skyrmions or chiral domain walls can be seen as topology in real space. These chiral spin textures can also induce an exceeding Hall current known as topological Hall effect. The topological Hall effect has been observed in magnetic TI-based heterostructures including Cr-doped-$(Bi_{1-x}Sb_x)_2Te_3$/$(Bi_{1-x}Sb_x)_2Te_3$ heterostructures and Cr-doped-$(Bi_{1-x}Sb_x)_2Te_3$/$(Bi_{1-x}Sb_x)_2Te_3$/Cr-doped-$(Bi_{1-x}Sb_x)_2Te_3$ sandwich heterostructures (Yasuda et al., 2016; Jiang et al., 2020).

Crystal structures of 2D chalcogenide TIs

The Bi/Sb-sesquichalcogenides are also termed tetradymites because they have the same rhombohedral layered structure as the mineral tetradymite (Bi_2Te_2S), with space group $R\bar{3}m$ as shown in **Fig. 21**A. A hexagonal unit cell is often convenient to describe the structure. The unit cell consists of 3 SLs along the c-axis with ABC stacking. Each SL contains 5 strongly bonded monolayers, and the SL is therefore commonly referred to as a quintuple layer (QL). Each SL consists of equivalent chalcogen sites at the top and bottom, an inequivalent chalcogen site in the middle, and pnictide sites between them in an octahedral arrangement with the surrounding chalcogens, as shown in **Fig. 21**A. For Bi_2Se_3 the SL looks like alternating layers of Bi and Se atoms, $Se_{(1)}$—Bi—$Se_{(2)}$—Bi—$Se_{(1)}$. The inequivalence of the middle chalcogen site can lead to ordering in mixed chalcogen materials, such as the $Te_{(1)}$—Bi—$S_{(2)}$—Bi—$Te_{(1)}$ SL structure of tetradymite, although the ordering is often not perfect. It was found that the shorter bond length of S on the central site of tetradymite necessitates additional S on the Te sites to relieve the strain in the crystal, resulting in a composition closer to $Bi_2Te_{1.8}S_{1.2}$ (Pauling, 1975). The bonds between the SLs have vdW character and thus this location is the natural cleavage plane of the material.

Bi_2Se_3, Bi_2Te_3, Sb_2Te_3 will all form in the tetradymite structure. However other binary combinations of pnictide and chalcogen elements will generally form in lower symmetry structures that are not topological. Bi_2S_3 and Sb_2Se_3 form in the orthorhombic stibnite (Sb_2S_3) structure. As an extension of this class of materials, arsenic forms in the monoclinic orpiment (As_2S_3) structure, although a metastable tetradymite structure β-As_2Te_3 can be synthesized (Morin et al., 2015). A summary of the phases of ternary alloys and solubilities can be found in (Heremans et al., 2017).

Growth of 2D chalcogenide TIs

Bulk growth of 2D chalcogenide TIs

Much work has been done trying to create intrinsic samples without carriers populating the bulk bands (Butch et al., 2010). This avenue is though extremely difficult because the volatility of the chalcogen causes vacancies as outlined in **section The vapor pressure mismatch** and the similar electronegativities of the elements make anti-site defects highly common. In bulk grown Bi_2Se_3, selenium vacancy V_{Se}^{2+} double donors are the predominant defect (Navrátil et al., 2004; Unzueta et al., 2016). Imaging the defects using STM confirmed this and identified lower densities of Bi_{Se} anti-sites and Se interstitials (Dai et al., 2016). DFT calculations predict V_{Se}^{2+} to dominate under Bi-rich growth conditions and Se_{Bi}^{+} under Se-rich growth conditions (West et al., 2012; Xue et al., 2013). As both are donors, Bi_2Se_3 is invariably n-type. At stoichiometry, Bi_2Te_3 melts incongruently and creating bulk insulating samples has not been possible (Heremans et al., 2017). This is even though for bulk growth under Te-rich conditions samples are n-type because of Te_{Bi}^{+} anti-sites and p-type under Bi-rich conditions because of Bi_{Te}^{-} anti-sites. Nevertheless, this ambipolarity has been useful for thermoelectrics. Sb_2Te_3 is invariably p-type because of Sb_{Te}^{-} and Sb^{-} vacancies (West et al., 2012). It is therefore close to impossible to grow a charge-neutral binary topological insulator with chemical potential inside the bulk band gap with bulk methods.

While doping with elements such as Ca has been used to make Bi_2Se_3 p-type (Hor et al., 2009), ternary or quaternary alloys have been the most promising materials. Among bulk growth methods, Bi_2Te_2Se has been widely grown, where Se predominantly occupies the middle chalcogen site of the SL like S does in tetradymite. This reduces Se vacancies and anti-site defects leading to much more insulating samples where Shubnikov-de Hass oscillations from the surface states can be observed but where, like Bi_2Te_3, the Dirac point is buried in the valence band (Ren et al., 2010). As mentioned above, the addition of Sb into the crystal can move the Dirac point above the valence band edge. Multiple groups have reported bulk growth of the quaternary $(Bi_{1-x}Sb_x)_2(Te_{1-y}Se_y)_3$, however this is especially difficult to control when trying to create large single crystals because there is no thermodynamic minimum helping to stabilize the correct ratio of the elements. Cava's group synthesized lightly Sn doped $Bi_{1.1}Sb_{0.9}Te_2S$ by vertical Bridgman which balances the strain from the small S atoms in the central layer sites by replacing some Bi with smaller atomic radius Sb, to stabilize the stoichiometric compound with a bulk resistivity $> 100\ \Omega$ cm (Kushwaha et al., 2016). The substitution of a small amount of Sn for Bi creates a resonant defect level near the band edge that helps localizing free carriers. This localization effectively compensates for the remaining defects, leading to a very insulating material. The formation of large single crystal boules from the melt is possible through this mechanism, which elevates $Bi_{1.1}Sb_{0.9}Te_2S$ to the most promising bulk grown composition identified thus far.

Thin film growth of 2D chalcogenide TIs

Due to interest in their thermoelectric properties, thin films of these materials have been grown by MBE since at least the late 1980s (Charles et al., 1988). These compounds are generally easy to grow by conventional MBE techniques, where Bi_2Te_3 is n-type under typical growth conditions while Sb_2Te_3 is typically strongly p-type. Point defects in samples grown by MBE observed by STM appear to be the same as in bulk-grown samples but densities were reported to be lower than in bulk samples (as low as 1 per 50 nm^2) (Cheng et al., 2010). Se cracker sources for MBE growth have been introduced in an effort to reduce this number even further and increase Se incorporation into the growing film. Simple Knudsen effusion cells deliver thermally evaporated Se in the form of long chains, ring molecules or clusters of atoms such as Se_5 and Se_8. Cracker cells, however, deliver much smaller Se molecules that have increased reactivity compared to the larger ones, which potentially lowers the need for excessively high Se overpressures, increases the surface diffusion and leads to better film growth. The growth with Se crackers though did not provide clear evidence for improved film properties. Simple Knudsen effusion cells are therefore still common in the field (Zhang et al., 2012c; Ginley and Law, 2016) Nevertheless, the carrier density in MBE-grown thin films is often higher than in the best bulk-grown samples. The reason for this may be the much larger density of extended defects in vdW epitaxy grown samples, such as the above discussed 1D line defects like grain boundaries from in-plane rotational domains and interface dislocations common in van der Waals materials (Li et al., 2010; Tarakina et al., 2014). These types of defects lead to surface roughening, increased scattering of both bulk and surface states, and with that to a lower carrier mobility (Kandala, 2015). As expected, this is influenced by the substrate, where well lattice-matched substrates such as InP(111) were found to reduce these defects (Guo et al., 2013; Schreyeck et al., 2013; Richardella et al., 2015). The presence of such defects is clearly seen in AFM and XRD characterization as shown in **Fig. 22**. Triangular hillocks are the common surface roughening growth topology. Different orientations of the hillocks indicated twinned crystal domains and the terraces often spiral around the center of the hillock where a screw dislocation resides. Like other vdW materials, the substrate surface preparation can strongly influence the epitaxial relationship between the film and substrate and the degree of twinning present.

Another influence on the carrier densities are the electrostatics at work in the band-bending that occurs in very thin samples of small bandgap materials like these. In Bi_2Se_3 the best bulk carrier densities achievable are still orders of magnitude higher than what would be needed for the crystals to be intrinsic semiconductors. Instead, E_F in the bulk is pinned near the conduction band edge, as observed in ARPES. The dispersion of the topological surface states allows the flat-band condition to be calculated to occur for $\approx 5.0 \times 10^{12}\ cm^{-2}$ carriers at the surface (Brahlek et al., 2015). The actual surface density would be expected to be affected by defects, environmental contamination and oxidation, well as charge traps at interfaces and substrates. If the surface E_F is below this carrier density upward band bending would be expected resulting in a surface depletion region, while higher densities result in downward bending and an electron accumulation area at the surface. Charge accumulation results in Rashba split surface states, which can cancel the transport spin polarization of the topological surface states to some extent (King et al., 2011). If a film is

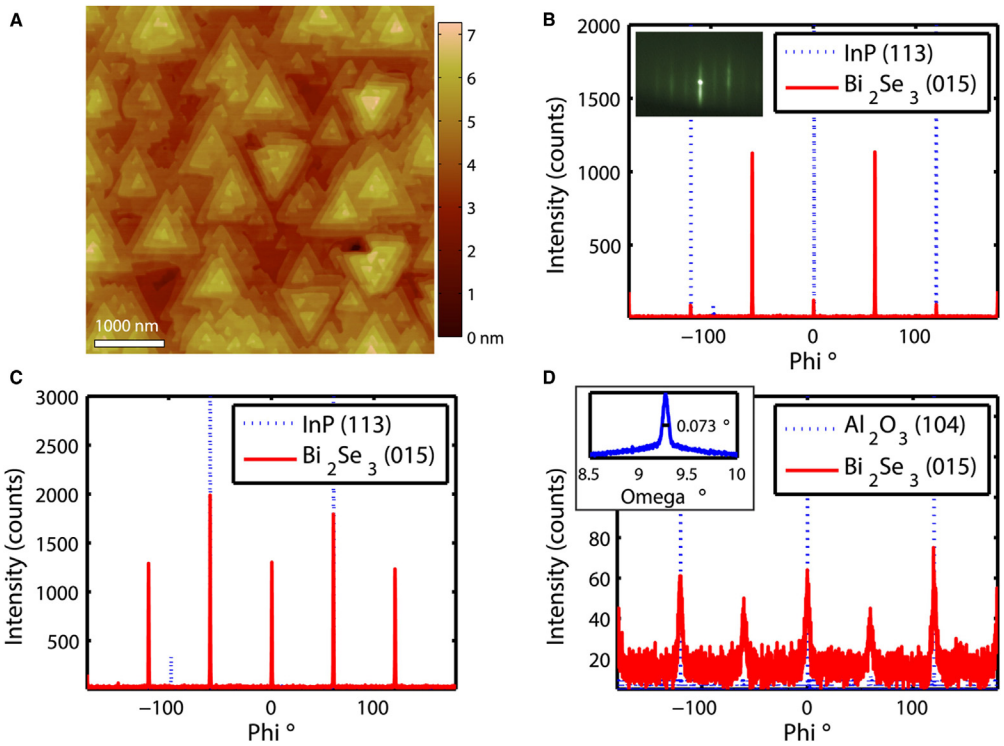

Fig. 22 Structural defects in TIs. (A) AFM image of Bi_2Se_3 grown on InP(111)A after the substrate oxide was desorbed under a flux of arsenic. Twinned domains can be seen in such images as regions where the triangular features on the surface point in different directions (up vs. down in this image). (B) XRD phi-scan of the same sample versus (C) phi-scan of a sample grown on InP(111)A, where the substrate oxide was desorbed under Se flux. Such scans measure the proportion of twinned domains. For an un-twinned sample, i.e., the InP substrate only a three-fold (every 120°) pattern is observed. (D) Phi-scan for Bi_2Se_3 on sapphire shows it also has a dominant orientation but the broad rocking curve tails in the inset indicate that the crystal quality at the interface is poor. Reproduced under a Creative Commons Attribution (CC BY) license from Richardella et al. (2015).

dominated by extrinsic defects at the surfaces, the film carrier density will increase and move E_F away from the Dirac point. Charge accumulation is common in Bi_2Se_3 samples, and it is expected that the mobility of these resulting states will be lower than in the depletion regime. Conversely, in the upward bending, depletion regime the band bending potential is not well screened and can deplete carriers out of the bulk bands for films of a few 10s of nm (Brahlek et al., 2014, 2015).

Ironically, reducing the bulk carriers can effectively put samples in the downward bending regime if the surface charge density stays the same. Careful analysis of Shubnikov-de Haas oscillations has revealed this behavior and shown that the interface with a substrate can result in significant charge accumulation that influences the transport properties (Veyrat et al., 2015). This highlights the importance of defects at both top and bottom surfaces of the TI films on the final properties of devices.

One novel way of reducing the effect of defects at the substrate interface was pioneered by Oh's group in using an elaborate In_2Se_3 buffer layer procedure, which lowered the Bi_2Se_3 carrier density to around 10^{12} cm^{-2} and resulted in mobilities of over 11,000 cm^2/Vs. (Koirala et al., 2015).

Magnetic doping of TIs

The transition metal doped TI systems have been successfully grown in the last two decades by various single crystal and thin film growth methods (Zhou et al., 2005, 2006b; Cha et al., 2010; Hor et al., 2010; Checkelsky et al., 2012, 2014; Zhang et al., 2012a, 2013a, 2017c; Haazen et al., 2012; Kou et al., 2012, 2013, 2014; Li et al., 2012, 2013; Liu et al., 2012b; Xu et al., 2012; Bao et al., 2013; Chang et al., 2013a; Lee et al., 2014; Kandala et al., 2015; RŮžička et al., 2015; Liu et al., 2017). Among them, the MBE technique allows to grow high quality thin films under non-equilibrium condition with precise doping control. In this section, we therefore mainly focus on the magnetic TI systems grown by MBE.

The growth recipes of magnetically doped TI materials are similar with pure TI growth, which can be achieved by co-evaporating transition metal dopants (Cr, V, Mn and Fe) and TI elements (Bi, Sb, Te and Se). Several characterizations including the content and homogeneity of magnetic dopants should be done after the growth to check the sample quality. For the doping concentration, beam equivalent pressure (BEP) or quartz crystal monitors (QCM) can be used to calculate the elemental ratios. A different way to obtain the doping concentration is using XRD to compare the change of lattice parameter. However, the magnetic dopants can be incorporated into the crystal lattice sites by several distinct processes including substituting for the cation or anion, occupying interstitial lattice sites, and entering the vdW gaps (Zhou et al., 2006b).

In order to investigate the ferromagnetism in the magnetic TI systems, measurement methods including transport, superconducting quantum interference device (SQUID) and ARPES are widely used. As shown in Fig. 23, electrical transport Hall measurements and SQUID can both assess the anomalous Hall effect, while ARPES can directly detect the magnetic gap. Up to now, the ferromagnetism was observed in Cr-, V-doped Sb_2Te_3, Mn-, Cr-, V-doped Bi_2Se_3, Mn-, Cr-doped Bi_2Te_3, Cr-doped $Bi_2(Se_xTe_{1-x})_3$ and Cr-, V-doped $(Bi_{1-x}Sb_x)_2Te_3$ (Zhou et al., 2005, 2006a,b; Haazen et al., 2012; Zhang et al., 2012c, 2017c; Kou et al., 2012, 2013, 2014; Liu et al., 2012b; Xu et al., 2012; Bao et al., 2013; Chang et al., 2013a,b, 2015; Zhang et al., 2013a,b; Checkelsky et al., 2014; Lee et al., 2014; Kandala et al., 2015; RŮžička et al., 2015; Liu et al., 2017).

The QAHE was first observed in five quintuple layer $Cr_{0.15}(Bi_{0.1}Sb_{0.9})_{1.85}Te_3$ thin films grown on $SrTiO_3(111)$ in 2013 (Chang et al., 2013a). Other substrates including InP(111) and GaAs(111) have also been used to realize the QAHE in the Cr-doped TI system (Checkelsky et al., 2014; Kou et al., 2014; Kandala et al., 2015). In 2015, the QAHE was observed in V-doped $(Bi_{1-x}Sb_x)_2Te_3$ thin films with high precision of Hall conductance at 25 mK, which confirms the equivalence between the QAHE and the QHE (Chang et al., 2015).

In the following section, we take the five quintuple layer $Cr_x(Bi_ySb_{1-y})_{2-x}Te_3$ as an example to discuss the growth procedures in detail. In $Cr_x(Bi_ySb_{1-y})_{2-x}Te_3$ thin films, the Bi/Sb ratio is tuned to $y \approx 0.25$. To get long range ferromagnetic order, the magnetic dopants are introduced by co-evaporating Cr, Bi, Sb and Te. At low doping levels, Cr can be uniformly doped into $(Bi_{1-x}Sb_x)_2Te_3$ by replacing Bi or Sb atoms. High doping levels, however, can form Cr clusters and drive the system into the topologically trivial phase. Thus, the doping level should be precisely controlled to generate long-range ferromagnetic order while avoiding Cr clusters. In $Cr_x(Bi_ySb_{1-y})_{2-x}Te_3$ thin films, the Cr concentration x is usually in the range from 0.05 to 0.15. Long-range ferromagnetic order can be assessed by transport and SQUID measurements. The Curie temperature is typically found at or around 90 K in Cr-doped Sb_2Te_3. After Bi is introduced into Cr-doped Sb_2Te_3, its Curie temperature shows a decrease to around 20 K.

An important step is to finely adjust the Cr concertation and Bi/Sb ratio during growth to increase the Hall resistance and decrease the longitudinal resistance. In Cr- or V-doped $(Bi_{1-x}Sb_x)_2Te_3$ thin films, the observable temperature of the QAHE is at dilution fridge temperature (tens of mK), which makes QAH measurements tedious and expensive. Fortunately, the behavior of the magnetoresistance around 2 K can predict the likelihood of observing the QAHE. At 2K, if bulk conduction is freezing out and chiral edge state conduction starts to dominate, R_{xx} will show a dip while R_{xy} will show a peak as the gate voltage is swept across the Dirac point. Consequently, this can be used to screen samples for the occurrence of the QAHE at dilution fridge temperatures.

Modulation doping of ferromagnetic $(Bi_{1-x}Sb_x)_2Te_3$ films has become the standard way to improve the robustness of the QAHE. By introducing the magnetic dopants only in the vicinity of the top and bottom surfaces, they can still provide strong magnetic order near the surface states while reducing the doping induced disorder in the bulk of the film. An increase in the observable temperature of the QAHE up to 2 K was demonstrated using this method (Mogi et al., 2015). Furthermore, as the coercive field of V-doped samples is significantly higher than for Cr-doping, one surface with Cr and the other with V allows the orientation of the magnetization of the surfaces to be controlled independently using an external magnetic field allowing the observation of the axion insulator state (Mogi et al., 2017; Xiao et al., 2018).

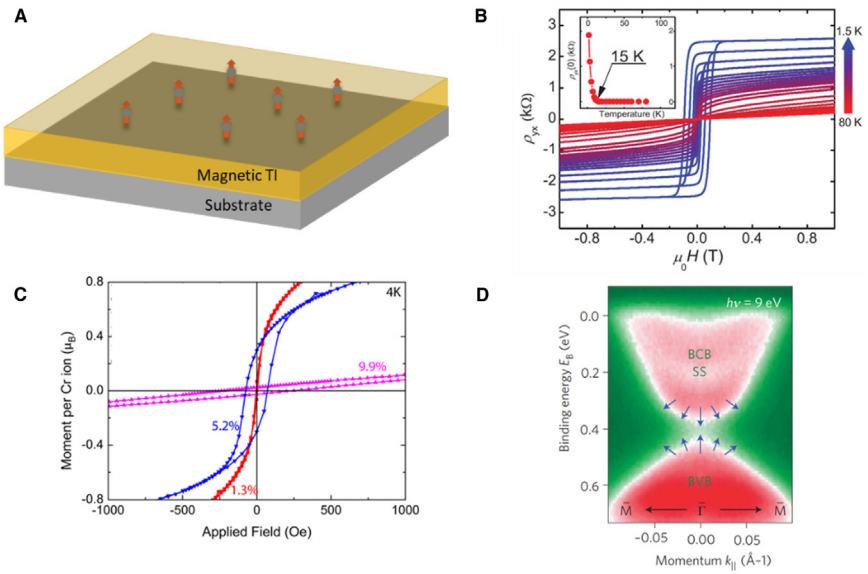

Fig. 23 The magnetic TI systems. (A) Schematic of magnetic doping. (B) The QAHE observed in a 5-SL-thick $Cr_{0.15}(Bi_{0.1}Sb_{0.9})_{1.85}Te_3$ thin film on a $SrTiO_3(111)$ substrate. The inset plot indicates a Curie temperature around 15 K (C) The magnetization measured by SQUID for 70 nm $Cr_xBi_{2-x}Se_3$ on Si(111) at T = 4 K (D) The magnetic gap opening measured by ARPES in a 60-nm-thick $Mn_xBi_{2-x}Se_3$ thin film on GaAs(111) with ZnSe buffer layer. The arrows indicate the spin polarization direction. Reprinted with permission from references (Haazen et al., 2012; Xu et al., 2012; Chang et al., 2013b)

Intrinsically magnetic 2D chalcogenide TI $MnBi_2Te_4$

The drawback of most doping mechanisms is the randomness of the dopant distribution, which leads to disorder in the doped system. This is particularly disadvantageous for investigations of the QAHE since it limits its observable temperature to an extremely low temperature range. Therefore, much effort has been dedicated to finding intrinsically ordered ferromagnetic TI materials. This was satisfied in $MnBi_2Te_4$. Magnetic doping of Mn in Bi_2Te_3 propitiated the discovery of this intrinsic ferromagnetic topological insulator (Li et al., 2019a; Otrokov et al., 2019; Otrokov et al., 2019).

$MnBi_2Te_4$ can be synthesized as single crystals or as thin films using molecular beam epitaxy (Gong et al., 2019; Otrokov et al., 2019; Deng et al., 2020; Liu et al., 2020). By MBE, as shown in **Fig. 24**A, a single quintuple layer of Bi_2Te_3 is grown on a nonmagnetic substrate first. After this, a MnTe bilayer is grown on top of the TI. The heterostructure is then annealed for 10 min to promote the diffusion of Mn to the bottom layer and Bi to the upper forming a SL of $MnBi_2Te_4$ consisting of seven atomic layers, referred to as a septuple layer. The process is now repeated to grow a film of any arbitrary thickness one SL at the time as demonstrated by the scanning transmission electron microscopy (STEM) image in **Fig. 24**B and C (Gong et al., 2019). This growth method is especially useful since $MnBi_2Te_4$ possesses A-type antiferromagnetic order, such that each SL is antiferromagnetically coupled to the neighboring ones with opposing magnetic moment. This means that the magnetism in the material can be controlled in a structural manner by changing the number of SL (odd being ferromagnetic and even anti-ferromagnetic) (Chen et al., 2019b; Lee et al., 2019). Furthermore, the anti-ferromagnetic interlayer coupling also allows the realization of the QAH effect and the axion insulator state, which have been demonstrated in exfoliated samples but not yet in thin films due to less than optimal sample quality (Zhang et al., 2019a; Deng et al., 2020; Liu et al., 2020). Bulk growth has also demonstrated the ability to form an periodic ordered crystal of $MnBi_2Te_4$ septuple layers and Bi_2Te_3 quintuple layers. By carefully introducing defects into such a crystal by electron irradiation to tune the Fermi energy, this structure has demonstrated QAHE approaching quantization as high as 7 K (Deng et al., 2021).

Magnetic heterostructures

An alternative way of introducing magnetism into TIs without increasing the disorder in the system relies on proximity coupling between a TI and a magnet realized through heterostructures. The magnetic proximity effect approach has mainly focused on using ferromagnetic insulators to induce magnetism without altering the electrical conduction in the TI layer. In contrast to doping, this approach has the advantage of not introducing crystal defects, magnetic scattering centers or impurity states in the insulating bandgap of the TI (Wei et al., 2013). Moreover, it has been shown that magnetic proximity can lift the spin degeneracy of Cooper pairs without destroying superconductivity, which might be beneficial for quantum computing applications involving Majorana quasiparticles (Hao et al., 1991; Wei et al., 2013). Typically used insulating ferromagnets include EuS, GdN, $Cr_2Ge_2Te_6$ (CGT), $Y_3Fe_5O_{12}$ (YIG), $Tm_3Fe_5O_{12}$ (TIG) and $BaFe_{12}O_{19}$ (BaM).

Early studies of magnetic proximity effect started with EuS ($T_C \approx 20$ K) and GdN ($T_C \approx 70$ K). These are both insulating in-plane ferromagnets that can be deposited at room temperature after the growth of the TI either by e-beam evaporation or radiofrequency (RF) sputtering (Kandala et al., 2013; Wei et al., 2013; Katmis et al., 2016). Since the interface is crucial for the proximity

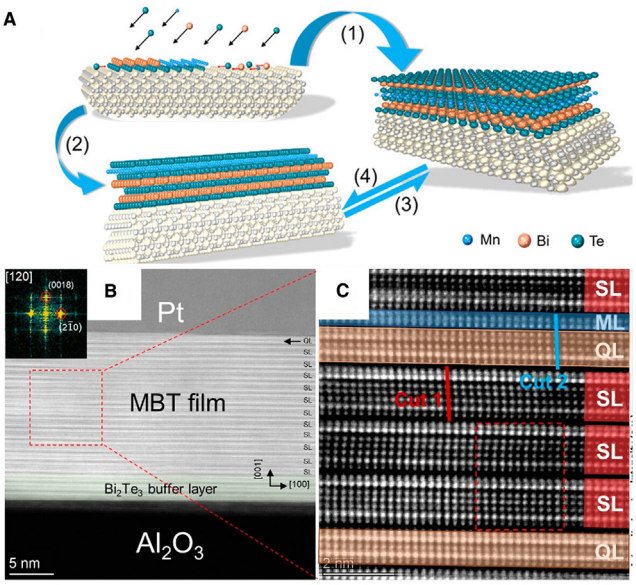

Fig. 24 MBE-growth process of $MnBi_2Te_4$. (A) Reaction paths for MBE growth of $MnBi_2Te_4$. $MnBi_2Te_4$ can form directly or as a consequence of Mn diffusing into Bi_2Te_3 when MnTe/Bi_2Te_3 heterostructures are annealed. (B) Cross-sectional STEM image of a $MnBi_2Te_4$ film. (C) The zoom-in on the center of the $MnBi_2Te_4$ thin film showing additional layers of MnTe (ML) and Bi_2Te_3 (QL) that are hard to eliminate. Reprinted with permission from reference (Luo et al., 2023).

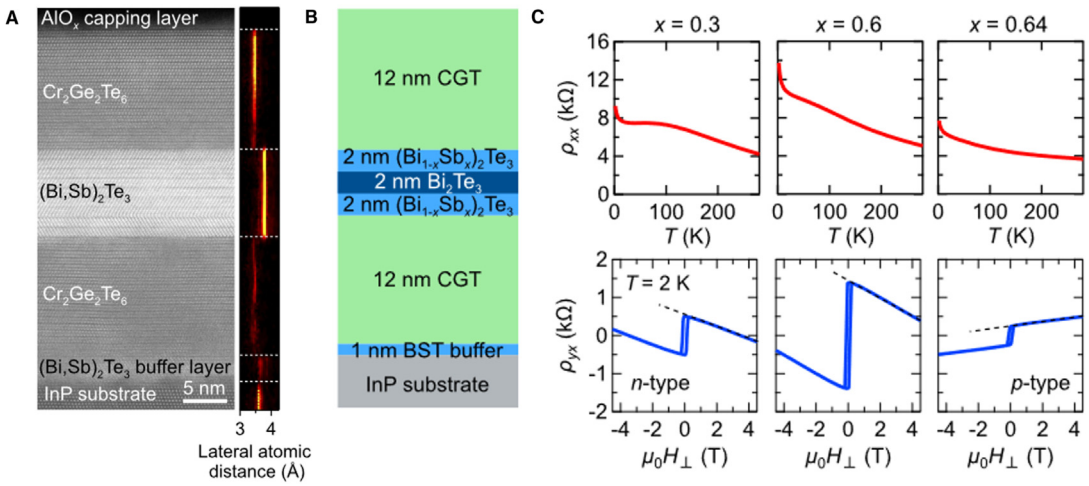

Fig. 25 Demonstration of MBE-grown magnetic/TI heterostructure with strong proximity coupling. (A) Cross-sectional HAADF-STEM image of the MBE-grown CGT (12 nm)/$(Bi_{1-x}Sb_x)_2Te_3$ (9 nm)/CGT (12 nm) heterostructure on InP. (B) Sketch of the same heterostructure shown in (A). (C) Temperature dependence of the longitudinal resistance measured in zero field—top, and magnetic field dependence of the Hall resistivity measured at 2 K-bottom for heterostructures containing different Sb concentrations of x = 0.3, 0.6, and 0.64 in the TI $(Bi_{1-x}Sb_x)_2Te_3$ layer. Reprinted with permission from reference (Mogi et al., 2019).

effect, it is necessary to fabricate these heterostructures without breaking vacuum or by plasma cleaning the surface of the TI before deposition (Kandala et al., 2013; Wei et al., 2013; Katmis et al., 2016).

Proximity coupling in TIs was furthermore achieved by using a full MBE-grown sandwich structure with the epitaxial out-of-plane magnetic insulator $Cr_2Ge_2Te_6$ ($T_C \approx 90$ K), as shown in **Fig. 25**. Van der Waals epitaxy makes it compatible with $(Bi_{1-x}Sb_x)_2Te_3$ which can also be used as buffer layer for this material. $Cr_2Ge_2Te_6$ is grown at 180 °C in Te overpressure to suppress Te deficiencies in the ferromagnet and the Cr to Ge ratio is usually chosen such that resistivity is maximized (Alegria et al., 2014; Mogi et al., 2018, 2019). In such structures, the proximity effect has been confirmed by polarized neutron reflectivity and magnetoresistance measurements (Ji et al., 2013; Kandala et al., 2013; Wei et al., 2013).

After these first attempts, much attention was directed to the use of iron garnets as substrates for topological insulators based on their ideal properties for technological applications like high resistance (as high as 10^{12} Ωcm at room temperature), high Curie temperature ($T_C \approx 560$ K), and low magnetic damping (10^{-3}–10^{-4}) (Jiang et al., 2015, 2016; Tang et al., 2017; Thiery et al., 2018). These efforts have mainly focused on using $Y_3Fe_5O_{12}$ (YIG) and $Tm_3Fe_5O_{12}$ (TIG) which have an in-plane and out-of-plane magnetic anisotropy, respectively. The growth of these materials is typically carried out on gadolinium gallium garnet $Gd_3Ga_5O_{12}$ (GGG) by sputtering, pulsed laser deposition or liquid phase epitaxy (Harrison et al., 2014; Tang et al., 2017). Since the interface is essential to achieve the magnetic proximity effect, the substrate is typically annealed at 500–600 °C for 1 h before lowering the temperature to initiate a two-step growth process. Because of the difficulty of growing a continuous film on these oxides due to the difference in the surface energies, a single SL is typically first deposited at low temperature to serve as seed layer for the remaining TI material that is grown at the typical growth temperature. It has also been reported that a 2-nm-thick amorphous Se layer combined with a 1-SL-thick amorphous Bi_2Se_3 layer deposited on TIG at 50 °C can crystallize as the temperature is raised to the growth temperature for the remaining TI film producing clean interfaces (Chen et al., 2019c). The magnetism in these heterostructures has been extensively studied by polarized neutron reflectivity, magneto optical Kerr effect, ferromagnetic resonance, and spin pumping (Lang et al., 2014; Wang et al., 2016a, 2019a; Katmis et al., 2016). Moreover, electrical transport has shown changes in magnetoresistance and QAHE that has been measured at temperatures as high as 400 K (Tang et al., 2017).

A similar growth method that involves a soft anneal followed by a two-step TI deposition technique has also been reported in M-type barium hexaferrite $BaFe_{12}O_{19}$ ($T_C = 725$ K, also denoted as BaM) (Li et al., 2019b). In this case the proximity effect has been demonstrated by magnetoresistance measurements, room temperature QAHE and current driven magnetization switching (Yang et al., 2014c; Li et al., 2019b).

Summary and outlook

When 3D topological insulators were first discovered it was hoped that the topological suppression of backscattering would lead to higher mobility materials than topologically trivial ones. This has not been borne out by experiments, the mobilities observed are generally comparable with other van der Waals materials. What has been remarkable however is the degree to which the topological properties are robust against disorder. For magnetically doped QAHE, samples with mobilities on the order of a few hundred cm^2/

Vs can show quantization to a few parts in 10^4 (Liu et al., 2016b). Recently, Cr doped heterostructure samples have been shown to reach quantization within 10 parts per billion using just a permanent disk magnet (Okazaki et al., 2022). This level of quantization is comparable to that of the quantum Hall effect that needs a large superconducting magnet capable of producing fields of several Tesla to be observed and is the current resistance standard for metrology. If such QAHE samples can be produced routinely they may become the new basis for the resistance standard utilizing portable measurement setups that, while still requiring low temperatures, would not need bulky superconducting magnets.

For topological insulator's technological applications, we seem quite far from the proposal to use the chiral edge modes of QAHE as dissipationless wires in devices, but TI's spin properties have clearly shown promise. In the field of spintronics, 3D topological insulators have raised substantial interest since the first experimental demonstration using Bi_2Se_3 interfaced with a ferromagnet to generate spin-orbit torques (Mellnik et al., 2014). This can be used to manipulate the magnetization of the ferromagnet using electric current instead of an external magnetic field. The strong spin-orbit torques in the 3D topological insulators can be attributed to the "spin-momentum locking" properties in the topological surface states when passing a charge current generating non-equilibrium spin polarization, although there are debates on whether the spin-polarized surface states can be perturbed in the proximity of the ferromagnet based on first principles calculations (Zhang et al., 2016a). Nevertheless, topological surface states and strong spin-orbit coupling in the typical 3D topological insulators make them promising material candidates to generate efficient current-induced spin-orbit torques for low-power consumption spintronics devices as compared to traditional materials, such as heavy metals (Liu et al., 2012a). Spin-orbit-torque-assisted magnetization switching at room temperature using 3D topological insulators has been experimentally demonstrated with high efficiencies (Han et al., 2017; Li et al., 2019b). The idea of harnessing the topological properties of the materials in spintronics applications can be further extended to other topological material systems, such as Dirac and Weyl semimetals, as there has been ongoing interest in studying the charge-spin interconversion in those materials as a result of their 3D topological band structures (Sun et al., 2016a; Yanez et al., 2021, 2022). However, there are still obstacles that need to be overcome in the actual practical applications of 3D topological insulators, such as the compatibility challenge of using these materials in the CMOS manufacturing process that usually undergoes higher annealing temperatures (> 450 °C) than the growth temperatures of the topological insulators themselves.

As these 3D topological insulators are van der Waals materials, it provides other opportunities for complex heterostructures with other novel 2D material systems, such as 2D magnets. The discovery of robust long-range magnetism in 2D magnets has opened up new research areas interfacing them with strong spin-orbit coupling materials, such as TMDs like WTe_2 resulting in large spin-orbit torques and in exotic real-space magnetic structures (Wu et al., 2020) or with new topological materials for magnetization switching (Ou et al., 2022). In this context, there are a plethora of possible interfacial effects that can be custom designed by a careful choice of materials utilizing the topological properties of these materials.

Summary and future directions for 2D semiconductor and topological insulator synthesis

In conclusion, the field of chalcogenide-based 2D vdW semiconductors and TIs is highly relevant to both future advanced technologies, and the study of fundamental carrier transport and quantum coupling mechanisms as their properties give rise to new physics and enable novel device functionalities. As a result, the field is highly vibrant and active. Despite impressive recent advances, especially in the growth of SL-thick wafer-sized TMDs, many unsolved challenges remain for the synthesis of these materials. The challenges can be sorted into two categories, depending on whether they concern obstacles in the growth process—category one—or arise as fundamental issues of the vdW nature—category two.

Category one comprises the above often mentioned point and line defects, intentional and unintentional doping, alloying within SLs to the extreme point of Janus structure synthesis, and chalcogen vacancies—characteristics that define the materials' transport properties like carrier mobility, carrier density, and positioning the Fermi level within the bandgap of the material. These category-one characteristics of 2D chalcogenide materials not only vary largely by fabrication method. To this date is also undefined what the intrinsic properties of a most-pristine 2D vdW chalcogenide material are (Zhang et al., 2014; Ciarrocchi et al., 2018; Li et al., 2018b; Xu et al., 2019; Xiong et al., 2020; Hilse et al., 2024). Although there is a plethora of theoretical studies on the fundamental properties of these materials, these studies are sometimes contradictory, and the experimental evaluation of category-one characteristics and the trustworthiness of theoretical studies is tedious and expensive (Gopalan et al., 2019; Villaos et al., 2019; Shi et al., 2020; Li et al., 2021a). The lack of standards and metrics for these materials weigh heavy on the development and betterment of growth processes. Growers' attention and efforts are therefore mostly directed towards attaining wafer-scale growth with SL precision and reducing point and line defects. It has furthermore been shown that the substrate—2D vdW film interaction strongly influences the observed electrical characteristics of a 2D vdW material (Cui et al., 2015). However, these potential effects stemming from the growth platform are often neglected in discussions of vdW materials. Much work is thus still needed to further our understanding and knowledge of the growth and properties of 2D vdW chalcogenides to determine their intrinsic properties and evaluate growth methods and strategies appropriately.

Challenges for 2D vdW chalcogenide materials' development in category two concern selective area growth, intercalation, the adaption of processing techniques to 2D vdW materials, especially the fabrication of low-resistance electrical contacts, as well as the introduction of magnetism in the 2D configuration (Ajayan et al., 2016; Huyghebaert et al., 2018; Stanford et al., 2018;

Kang et al., 2020; Cao et al., 2023). Despite the existence of all these category-two challenges that the vdW nature of these materials imposes, significant strides in this area have already been accomplished (Stanford et al., 2018). These accomplishments indicate a good omen for the potential use of 2D vdW chalcogenides in future electronics.

On a more positive and exciting note, the vdW epitaxy of intrinsically 2D layered materials offers some unique emergent phenomena and an additional degree of freedom in designing heterostructures and functional devices. The coupling of electrons and holes across SLs for example could lead to the realization of interlayer excitons with the potential of forming a superfluid and show the emergence of exotic superconducting states (Ajayan et al., 2016). The twist angle between SLs offers furthermore the possibility to introduce large-scale periodic commensurate or quasi-periodic incommensurate potentials into the energy landscape of a material or heterostructure. Such large-scale energy patterns are known as Moiré patterns that have the potential to realize a fractal energy spectrum, i.e., to observe the fractal quantum Hall effect (Ajayan et al., 2016). Atomically thin p-n junctions, exciton superfluidity at high temperatures, chiral resonant tunneling between SLs separated by an insulating barrier, and superconductor-semiconductor interface coupling with unusual Andreev reflections are further examples of highly intriguing phenomena that have been proposed in layered vdW materials (Ajayan et al., 2016).

Expanding on the advantages of vdW epitaxy is the recent realization of confinement hetero epitaxy (CHet) (Briggs et al., 2020; Dong et al., 2020a; Turker et al., 2023). CHet can be regarded as conventional epitaxy on SiC under the hood of a protecting and confining graphene layer. Intentionally created defects in the graphene layer grown previously on SiC expose the strong dangling bonds of the underlying substrate that effectively pull the impinging atoms through the defects in the graphene. Underneath the graphene, the atoms are forced to form a coalesced ultra-thin layer sandwiched between SiC and graphene. Since the so formed ultra-thin layer is still completely covered by graphene at the end of the growth process, CHet naturally delivers the film in a protected state against potentially harmful ambient conditions.

The heightened interest in 2D materials, and among those especially the 2D magnetic materials has furthermore led the field to expand beyond the chalcogenide-based 2D vdW semiconductors and TIs to other intrinsically vdW layered materials like halides (compounds containing the group VII elements F, Cl, Br, I)—a selection of halide semiconductors with formulars in analogy to the discussed chalcogenides is presented in **Fig. 26** plotting their band gap versus interlayer binding energy (Mounet et al., 2018; Khan et al., 2020; Aji Suleiman et al., 2021; Hou et al., 2022; Campi et al., 2023; Liu et al., 2023b). In comparison, 2D vdW halide semiconductors range on average at slightly lower interlayer binding energies than the family of chalcogenides. Exfoliation and layer transfer processes are thus most likely going to play a similarly important role for this class of materials. In addition, and contrasting with the 2D vdW chalcogenide semiconductors, the bandgaps of 2D vdW halide semiconductors cover the ultra-violet (UV), and deep-UV range as well, which adds much diversity to the pool of properties and applications of 2D vdW materials.

Theoretically predicted 2D vdW configurations of elemental and compound semiconducting materials of group II, III, IV, and V, that are unstable in bulk form are furthermore gaining interest, though their experimental pursuit is due to their unstable nature highly challenging (Ajayan et al., 2016; Hess, 2021; Qiu et al., 2022; Hayat et al., 2023). It should be mentioned here that there are also a few intrinsically 2D vdW layered semiconducting oxide materials (Sucharitakul et al., 2017; Frisenda et al., 2020; Feng et al., 2023).

Finally, new ways of engineering intrinsically 3D materials into 2D layered configurations using quasi-vdW spacer layers are recently being explored and are gaining more and more attention. This field comprises oxides, halides, and MXenes (Yan et al., 2018; Mao et al., 2019a; Ortiz-Cervantes et al., 2019; Li et al., 2021c; Friedrich et al., 2022; Yang et al., 2022; Zeng et al., 2023).

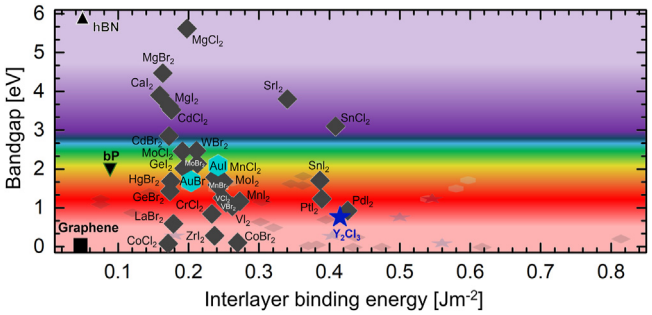

Fig. 26 Bandgap versus interlayer binding energy for the bulk 2D vdW halide [X = (F, Cl, Br, I)] semiconductors with formulas MX, MX_2, and M_2X_3 as well as bP, hBN, and graphene. The bandgaps covered by the halide composites selected in this view in analogy to the discussed chalcogenides span over a much larger bandgap range compared to the chalcogenides (chalcogenide data points from **Fig. 1** are overlayed in partial transparency for ease of comparison). On average, halide semiconductors possess furthermore slightly reduced interlayer binding energies, i.e., SL surface energies compared to the chalcogenide semiconductors and TIs. The data to compose this image was sourced from references: (Jain et al., 2011, 2013; Aykol et al., 2018; Latimer et al., 2018; Mounet et al., 2018; Wang et al., 2021; Campi et al., 2023; Merchant et al., 2023).

Acknowledgements

The authors acknowledge the financial support of the National Science Foundation (NSF) through the 2D Crystal Consortium – Materials Innovation Platform (2DCC-MIP) under NSF Cooperative Agreement No. DMR-1539916, and DMR-2039351.

N. Trainor acknowledges support from the National Science Foundation Graduate Research Fellowship Program (NSF-GRFP) under Grant No. DGE1255832.

R. Engel-Herbert furthermore acknowledges support by the US Department of Energy, Office of Science, Office of Basic Energy Sciences Energy Frontier Research Centers program under Award Number DE-SC0021118, as well as funding support through the US Department of Energy, Office of Science, Basic Energy Sciences, under Award Number DE-SC0020145 as part of the Computational Materials Sciences Program. R. Engel-Herbert also acknowledges additional support by the Federal Ministry of Education and Research Germany and the Senate of Berlin.

Any opinions, findings, and conclusions or recommendations expressed in this material are those of the author(s) and do not necessarily reflect the views of the National Science Foundation or the US Department of Energy.

References

Ajayan, P., Kim, P., Banerjee, K., 2016. Two-dimensional van der Waals materials. Phys. Today 69 (9), 38–44. https://doi.org/10.1063/PT.3.3297.
Ajayi, O.A., et al., 2017. Approaching the intrinsic photoluminescence linewidth in transition metal dichalcogenide monolayers. 2D Mater. 4 (3), 31011.
Aji Suleiman, A., Zhou, X., Zhai, T., 2021. Two-dimensional metal halides. J. Phys. Appl. Phys. 54 (1), 013002. https://doi.org/10.1088/1361-6463/abae35.
Akinwande, D., Petrone, N., Hone, J., 2014. Two-dimensional flexible nanoelectronics. Nat. Commun. 5 (1), 5678.
Akinwande, D., et al., 2019. Graphene and two-dimensional materials for silicon technology. Nature 573 (7775), 507–518.
Alegria, L.D., et al., 2014. Large anomalous Hall effect in ferromagnetic insulator-topological insulator heterostructures. Appl. Phys. Lett. 105 (5), 53512. https://doi.org/10.1063/1.4892353.
Ali, M.N., et al., 2015. Correlation of crystal quality and extreme magnetoresistance of WTe2. Europhys. Lett. 110 (6), 67002.
Allakhverdiev, K.R., et al., 2009. Effective nonlinear GaSe crystal. Optical properties and applications. Laser Phys. 19 (5), 1092–1104. https://doi.org/10.1134/S1054660X09050375.
Ando, Y., 2024. Topological insulators. In: Encyclopedia of Condensed Matter Physics. Elsevier, pp. 690–699. https://doi.org/10.1016/b978-0-323-90800-9.00005-6.
Andrzejewski, D., et al., 2018. Improved luminescence properties of MoS2 monolayers grown via MOCVD: role of pre-treatment and growth parameters. Nanotechnology 29 (29), 295704.
Annamalai, M., et al., 2016. Surface energy and wettability of van der Waals structures. Nanoscale 8 (10), 5764–5770. https://doi.org/10.1039/c5nr06705g.
Antunez, P.D., Buckley, J.J., Brutchey, R.L., 2011. Tin and germanium monochalcogenide IV–VI semiconductor nanocrystals for use in solar cells. Nanoscale 3 (6), 2399. https://doi.org/10.1039/c1nr10084j.
Armitage, N.P., Mele, E.J., Vishwanath, A., 2018. Weyl and Dirac semimetals in three-dimensional solids. Rev. Mod. Phys. 90 (1), 015001. https://doi.org/10.1103/RevModPhys.90.015001.
Arora, R., Waghmare, U.V., Rao, C.N.R., 2023. Metavalent bonding origins of unusual properties of group IV chalcogenides. Adv. Mater. 35 (7). https://doi.org/10.1002/adma.202208724.
Aykol, M., et al., 2018. Thermodynamic limit for synthesis of metastable inorganic materials. Sci. Adv. 4 (4). https://doi.org/10.1126/sciadv.aaq0148.
Bao, L., et al., 2013. Quantum corrections crossover and ferromagnetism in magnetic topological insulators. Sci. Rep. 3, 2391.
Bao, Y., et al., 2019. Gate-tunable in-plane ferroelectricity in few-layer SnS. Nano Lett. 19 (8), 5109–5117. https://doi.org/10.1021/acs.nanolett.9b01419.
Barraza-Lopez, S., et al., 2021. Colloquium: physical properties of group-IV monochalcogenide monolayers. Rev. Mod. Phys. 93 (1), 011001. https://doi.org/10.1103/RevModPhys.93.011001.
Batzill, M., 2018. Mirror twin grain boundaries in molybdenum dichalcogenides. J. Phys. Condens. Matter 30 (49), 493001. https://doi.org/10.1088/1361-648X/aae9cf.
Bernevig, B.A., Hughes, T.L., Zhang, S.-C., 2006. Quantum spin Hall effect and topological phase transition in HgTe quantum wells. Science 314 (5806), 1757–1761. https://doi.org/10.1126/science.1133734.
Bian, R., et al., 2022. Recent progress in the synthesis of novel two-dimensional van der Waals materials. Natl. Sci. Rev. 9 (5). https://doi.org/10.1093/nsr/nwab164.
Bonilla, M., et al., 2018. Strong room-temperature ferromagnetism in VSe2 monolayers on van der Waals substrates. Nat. Nanotechnol. 13 (4), 289–293.
Bouša, D., et al., 2020. Surface energy of black phosphorus alloys with arsenic. ChemNanoMat 6 (5), 821–826. https://doi.org/10.1002/cnma.202000143.
Brahlek, M., et al., 2014. Emergence of decoupled surface transport channels in bulk insulating Bi2Se3 thin films. Phys. Rev. Lett. 113 (2), 1–5. https://doi.org/10.1103/PhysRevLett.113.026801.
Brahlek, M., et al., 2015. Transport properties of topological insulators: band bending, bulk metal-to-insulator transition, and weak anti-localization. Solid State Commun. 215–216 (1), 54–62. https://doi.org/10.1016/j.ssc.2014.10.021.
Briggs, N., et al., 2020. Atomically thin half-van der Waals metals enabled by confinement heteroepitaxy. Nat. Mater. 19 (6), 637–643. https://doi.org/10.1038/s41563-020-0631-x.
Buchkov, K., et al., 2021. Anisotropic optical response of WTe_2 single crystals studied by ellipsometric analysis. Nanomaterials 11 (9), 2262. https://doi.org/10.3390/nano11092262.
Butch, N.P., et al., 2010. Strong surface scattering in ultrahigh-mobility Bi_2Se_3 topological insulator crystals. Phys. Rev. B 81 (24), 241301. https://doi.org/10.1103/PhysRevB.81.241301.
Cain, J.D., Hanson, E.D., Dravid, V.P., 2018. Controlled synthesis of 2D MX2 (M= Mo, W; X= S, Se) heterostructures and alloys. J. Appl. Phys. 123 (20), 11268–11278. https://doi.org/10.1021/acsnano.2c11510.
Campi, D., et al., 2023. Expansion of the materials Cloud 2D Database. ACS Nano 17 (12), 11268–11278. https://doi.org/10.1021/acsnano.2c11510.
Cao, Y., et al., 2015. Strong enhancement of photoresponsivity with shrinking the electrodes spacing in few layer GaSe photodetectors. Sci. Rep. 5 (1), 8130. https://doi.org/10.1038/srep08130.
Cao, W., et al., 2023. The future transistors. Nature 620. https://doi.org/10.1038/s41586-023-06145-x.
Cevallos, F.A., et al., 2019. Liquid salt transport growth of single crystals of the layered dichalcogenides MoS2 and WS2. Cryst. Growth Des. 19 (10), 5762–5767.
Cha, J.J., et al., 2010. Magnetic doping and Kondo effect in Bi2Se3 nanoribbons. Nano Lett. 10 (3), 1076–1081.
Chang, C., et al., 2013a. Thin films of magnetically doped topological insulator with carrier-independent long-range ferromagnetic order. Adv. Mater. 25 (7), 1065–1070.
Chang, C.-Z., et al., 2013b. Experimental observation of the quantum anomalous Hall effect in a magnetic topological insulator. Science 340 (6129), 167–170. https://doi.org/10.1126/science.1234414.
Chang, C.-Z., et al., 2015. High-precision realization of robust quantum anomalous Hall state in a hard ferromagnetic topological insulator. Nat. Mater. 14 (5), 473–477. https://doi.org/10.1038/nmat4204.

Chang, Y.-R., et al., 2017. Surface oxidation doping to enhance photogenerated carrier separation efficiency for ultrahigh gain indium selenide photodetector. ACS Photonics 4 (11), 2930–2936. https://doi.org/10.1021/acsphotonics.7b01030.

Chang, K., et al., 2020. Microscopic manipulation of ferroelectric domains in SnSe monolayers at room temperature. Nano Lett. 20 (9), 6590–6597. https://doi.org/10.1021/acs.nanolett.0c02357.

Charles, E., Groubert, E., Boyer, A., 1988. Structural and electrical properties of bismuth telluride films grown by the molecular beam technique. J. Mater. Sci. Lett. 7 (6), 575–577. https://doi.org/10.1007/BF01730298.

Chaves, A., et al., 2020. Bandgap engineering of two-dimensional semiconductor materials. Npj 2D Materials and Applications 4 (1), 29. https://doi.org/10.1038/s41699-020-00162-4.

Checkelsky, J.G., et al., 2012. Dirac-fermion-mediated ferromagnetism in a topological insulator. Nat. Phys. 8 (10), 729–733.

Checkelsky, J.G., et al., 2014. Trajectory of the anomalous Hall effect towards the quantized state in a ferromagnetic topological insulator. Nat. Phys. 10 (10), 731–736. https://doi.org/10.1038/nphys3053.

Chen, Y.L., et al., 2009. Experimental realization of a three-dimensional topological insulator, Bi2Te3. Science 325 (5937), 178–181. https://doi.org/10.1126/science.1173034.

Chen, J., et al., 2016. Chemical vapor deposition of high-quality large-sized MoS2 crystals on silicon dioxide substrates. Adv. Sci. 3 (8), 1500033.

Chen, B.B., et al., 2019a. Highly oriented GeSe thin film: self-assembly growth via the sandwiching post-annealing treatment and its solar cell performance †. Nanoscale 11. https://doi.org/10.1039/c8nr09836k.

Chen, B., et al., 2019b. Intrinsic magnetic topological insulator phases in the Sb doped MnBi2Te4 bulks and thin flakes. Nat. Commun. 10 (1), 4469. https://doi.org/10.1038/s41467-019-12485-y.

Chen, C.C., et al., 2019c. Topological insulator Bi2Se3 films on rare earth iron garnets and their high-quality interfaces. Appl. Phys. Lett. 114 (3), 31601. https://doi.org/10.1063/1.5054329.

Chen, C., et al., 2024. Effect of growth temperature on the microstructure and properties of epitaxial MoS2 monolayers grown by metalorganic chemical vapor deposition. J. Vac. Sci. Technol. A 42 (2). https://doi.org/10.1116/6.0003296.

Cheng, P., et al., 2010. Landau quantization of topological surface states in Bi_{2}Se_{3}. Phys. Rev. Lett. 105 (7), 076801. https://doi.org/10.1103/PhysRevLett.105.076801.

Cheng, Y., et al., 2019. Understanding the Structure and Properties of Sesqui-Chalcogenides (i.e., V2VI3 or Pn2Ch3 (Pn = Pnictogen, Ch = Chalcogen) Compounds) from a Bonding Perspective. Adv. Mater. 31 (43). https://doi.org/10.1002/adma.201904316.

Chernikov, A., et al., 2014. Exciton binding energy and nonhydrogenic Rydberg series in monolayer WS 2. Phys. Rev. Lett. 113 (7), 76802.

Chhowalla, M., et al., 2013. The chemistry of two-dimensional layered transition metal dichalcogenide nanosheets. Nat. Chem. 5 (4), 263–275.

Chhowalla, M., Jena, D., Zhang, H., 2016. Two-dimensional semiconductors for transistors. Nat. Rev. Mater. 1 (11), 1–15.

Chi, Z., et al., 2020. The spin Hall effect of Bi-Sb alloys driven by thermally excited Dirac-like electrons. Sci. Adv. 6 (10). https://doi.org/10.1126/sciadv.aay2324.

Choi, J., et al., 2022. A strategy for wafer-scale crystalline MoS2 thin films with controlled morphology using pulsed metal–organic chemical vapor deposition at low temperature. Adv. Mater. Interfac. 9 (4), 2101785.

Choudhury, T.H., et al., 2020. Epitaxial growth of two-dimensional layered transition metal dichalcogenides. Annu. Rev. Mater. Res. 50 (1), 155–177. https://doi.org/10.1146/annurev-matsci-090519-113456.

Chowdhury, C., Karmakar, S., Datta, A., 2017. Monolayer group IV–VI monochalcogenides: low-dimensional materials for photocatalytic water splitting. J. Phys. Chem. C 121 (14), 7615–7624. https://doi.org/10.1021/acs.jpcc.6b12080.

Chowdhury, S., et al., 2021. Two-step growth of uniform monolayer MoS2 nanosheets by metal–organic chemical vapor deposition. ACS Omega 6 (15), 10343–10351.

Chubarov, M., Choudhury, T.H., et al., 2021. Wafer-scale epitaxial growth of unidirectional WS2 monolayers on sapphire. ACS Nano 15 (2), 2532–2541. https://doi.org/10.1021/acsnano.0c06750.

Chung, Y.J., et al., 2022. Record-quality GaAs two-dimensional hole systems. Phys. Rev. Mater. 6 (3). https://doi.org/10.1103/PhysRevMaterials.6.034005.

Ciarrocchi, A., et al., 2018. Thickness-modulated metal-to-semiconductor transformation in a transition metal dichalcogenide. Nat. Commun. 9 (1). https://doi.org/10.1038/s41467-018-03436-0.

Cohen, A., et al., 2020. Growth-etch metal–organic chemical vapor deposition approach of WS2 atomic layers. ACS Nano 15 (1), 526–538.

Cohen, A., et al., 2023. Tungsten oxide mediated quasi-van der Waals epitaxy of WS2 on sapphire. ACS Nano 17 (6), 5399–5411.

Cui, X., et al., 2015. Multi-terminal transport measurements of MoS2 using a van der Waals heterostructure device platform. Nat. Nanotechnol. 10 (6), 534–540. https://doi.org/10.1038/nnano.2015.70.

Cunningham, G., et al., 2012. Solvent exfoliation of transition metal dichalcogenides: dispersibility of exfoliated nanosheets varies only weakly between compounds. ACS Nano 6 (4), 3468–3480. https://doi.org/10.1021/nn300503e.

Curiotto, S., Chatain, D., 2009. Surface morphology and composition of c-, a-and m-sapphire surfaces in O2 and H2 environments. Surf. Sci. 603 (17), 2688–2697.

Curreli, N., et al., 2020. Liquid phase exfoliated indium selenide based highly sensitive photodetectors. Adv. Funct. Mater. 30 (13). https://doi.org/10.1002/adfm.201908427.

Dai, J., et al., 2016. Toward the intrinsic limit of the topological insulator Bi2Se3. Phys. Rev. Lett. 117 (10), 106401. https://doi.org/10.1103/PhysRevLett.117.106401.

Das, S., et al., 2021. Transistors based on two-dimensional materials for future integrated circuits. Nat. Electron. 4 (11), 786–799.

Deckoff-Jones, S., et al., 2016. Observing the interplay between surface and bulk optical nonlinearities in thin van der Waals crystals. Sci. Rep. 6 (1), 22620. https://doi.org/10.1038/srep22620.

Deng, Y., et al., 2020. Quantum anomalous Hall effect in intrinsic magnetic topological insulator MnBi2Te4. Science 367 (6480), 895–900. https://doi.org/10.1126/science.aax8156.

Deng, H., et al., 2021. High-temperature quantum anomalous Hall regime in a MnBi2Te4/Bi2Te3 superlattice. Nat. Phys. 17 (1), 36–42. https://doi.org/10.1038/s41567-020-0998-2.

Dhar, S., et al., 2016. Chemical vapor deposition of MoS 2 layers from Mo–S–C–O–H system: thermodynamic modeling and validation. Phys. Chem. Chem. Phys. 18 (22), 14918–14926.

Dodda, A., et al., 2020. Stochastic resonance in MoS2 photodetector. Nat. Commun. 11 (1), 1–11.

Dong, C., et al., 2020a. Air-stable, large-area 2D metals and semiconductors. ACS Nanosci. Au 4. https://doi.org/10.1021/acsnanoscienceau.3c00047.

Dong, J., et al., 2020b. The epitaxy of 2D materials growth. Nat. Commun. 11 (1), 5862. https://doi.org/10.1038/s41467-020-19752-3.

Duan, X., et al., 2014. Lateral epitaxial growth of two-dimensional layered semiconductor heterojunctions. Nat. Nanotechnol. 9 (12), 1024–1030.

D'Olimpio, G., et al., 2020. Enhanced electrocatalytic activity in GaSe and InSe nanosheets: the role of surface oxides. Adv. Funct. Mater. 30 (43). https://doi.org/10.1002/adfm.202005466.

Edelberg, D., et al., 2019. Approaching the intrinsic limit in transition metal diselenides via point defect control. Nano Lett. 19 (7), 4371–4379. https://doi.org/10.1021/acs.nanolett.9b00985.

Eglitis, R.I., 2014. Ab initio calculations of $SrTiO_3$, $BaTiO_3$, $PbTiO_3$, $CaTiO_3$, $SrZrO_3$, $PbZrO_3$ and $BaZrO_3$ (001), (011) and (111) surfaces as well as F centers, polarons, KTN solid solutions and Nb impurities therein. Int. J. Modern Phys. B 28 (17), 1430009. https://doi.org/10.1142/S0217979214300096.

Eglitis, R.I., 2015. Comparative ab initio calculations of $SrTiO_3$ and $CaTiO_3$ polar (111) surfaces. Physica Status Solidi (B) 252 (3), 635–642. https://doi.org/10.1002/pssb.201248072.

Fei, R., et al., 2015. Giant piezoelectricity of monolayer group IV monochalcogenides: SnSe, SnS, GeSe, and GeS. Appl. Phys. Lett. 107 (17). https://doi.org/10.1063/1.4934750.

Fei, R., Kang, W., Yang, L., 2016. Ferroelectricity and phase transitions in monolayer group-IV monochalcogenides. Phys. Rev. Lett. 117 (9). https://doi.org/10.1103/PhysRevLett.117.097601.

Feng, W., et al., 2018. A fast and zero-biased photodetector based on GaTe—InSe vertical 2D p—n heterojunction. 2D Mater. 5 (2), 025008. https://doi.org/10.1088/2053-1583/aaa721.
Feng, X., et al., 2023. Two-dimensional oxide crystals for device applications: challenges and opportunities. Adv. Mater. https://doi.org/10.1002/adma.202304708.
Ferhat, M., Tedenac, J.C., Nagao, J., 2000. Mechanisms of spiral growth in Bi_2Te_3 thin films grown by the hot-wall-epitaxy technique. J. Crystal Growth 218 (2—4), 250—258. https://doi.org/10.1016/S0022-0248(00)00582-0.
Friedrich, R., et al., 2022. Data-Driven Quest for Two-Dimensional Non-van der Waals Materials. Nano Lett. 22 (3), 989—997. https://doi.org/10.1021/acs.nanolett.1c03841.
Frisenda, R., et al., 2020. Naturally occurring van der Waals materials. Npj 2D Materials and Applications 4 (1), 38. https://doi.org/10.1038/s41699-020-00172-2.
Fu, H., 2018. Environmentally friendly and earth-abundant colloidal chalcogenide nanocrystals for photovoltaic applications. J. Mater. Chem. C 6 (3), 414—445. https://doi.org/10.1039/C7TC04952H.
Fu, J.-H., et al., 2023. Oriented lateral growth of two-dimensional materials on c-plane sapphire. Nat. Nanotechnol. 18 (11), 1289—1294.
Ganatra, R., Zhang, Q., 2014. Few-layer MoS2: a promising layered semiconductor. ACS Nano 8 (5), 4074—4099.
Gendry, M., et al., 1997. Role of surface energy and surface reconstructions on the 2D-to-3D growth-mode transition of strained $In_xGa_{1-x}As$ layers on InP(001). Phys. Rev. B 56 (15), 9271—9274. https://doi.org/10.1103/PhysRevB.56.9271.
Ghorai, S., Govind Rajan, A., 2024. From molecular precursors to MoS2 monolayers: nanoscale mechanism of organometallic chemical vapor deposition. Chem. Mater. 36.
Gilardoni, C.M., et al., 2021. Symmetry and control of spin-scattering processes in two-dimensional transition metal dichalcogenides. Phys. Rev. B 103 (11), 115410.
Gilman, J.J., 1960. Direct measurements of the surface energies of crystals. J. Appl. Phys. 31, 2208—2218. https://doi.org/10.1063/1.1735524.
Ginley, T.P., Law, S., 2016. Growth of Bi 2 Se 3 topological insulator films using a selenium cracker source. J. Vac. Sci. Technol. B. Nanotechnol. Microelectron. 34 (2), 02L105. https://doi.org/10.1116/1.4941134.
Gomes, L.C., Carvalho, A., 2015. Phosphorene analogues: isoelectronic two-dimensional group-IV monochalcogenides with orthorhombic structure. Phys. Rev. B 92, 85406. https://doi.org/10.1103/PhysRevB.92.085406.
Gomes, C.L., Carvalho, A., 2020. Electronic and optical properties of low-dimensional group-IV monochalcogenides. J. Appl. Phys. 128 (12), 121101. https://doi.org/10.1063/5.0016003.
Gong, Y., et al., 2014. Vertical and in-plane heterostructures from WS 2/MoS 2 monolayers. Nat. Mater. 13 (12), 1135.
Gong, Y., et al., 2015. Two-step growth of two-dimensional WSe2/MoSe2 heterostructures. Nano Lett. 15 (9), 6135—6141.
Gong, Y., et al., 2019. Experimental realization of an intrinsic magnetic topological Insulator{\ast}. Chin. Phys. Lett. 36 (7), 76801. https://doi.org/10.1088/0256-307x/36/7/076801.
Gopalan, S., et al., 2019. Monte Carlo study of electronic transport in monolayer InSe. Materials 12 (24), 4210. https://doi.org/10.3390/ma12244210.
Green, M.A., 2013. Improved value for the silicon free exciton binding energy. AIP Adv. 3 (11).
Grimaldi, I., et al., 2020. Structural investigation of InSe layered semiconductors. Solid State Commun. 311, 113855. https://doi.org/10.1016/j.ssc.2020.113855.
Grundmann, M., 2011. Formation of epitaxial domains: Unified theory and survey of experimental results. Physica Status Solidi (B) 248 (4), 805—824. https://doi.org/10.1002/pssb.201046530.
Grzonka, J., et al., 2021. Novel polymorph of GaSe. Adv. Funct. Mater. 31 (48), 2104965.
Guan, H., et al., 2023. Liquid-precursor-intermediated synthesis of atomically thin transition metal dichalcogenides. Mater. Horiz. 10 (4), 1105—1120.
Guo, X., et al., 2013. Single domain Bi2Se3 films grown on InP(111)A by molecular-beam epitaxy. Appl. Phys. Lett. 102 (15), 151604. https://doi.org/10.1063/1.4802797.
Haazen, P.P.J., et al., 2012. Ferromagnetism in thin-film Cr-doped topological insulator Bi2Se3. Appl. Phys. Lett. 100 (8), 082404. https://doi.org/10.1063/1.3688043.
Haldane, F.D.M., 1988. Model for a quantum Hall effect without Landau levels: condensed-matter realization of the “parity anomaly”. Phys. Rev. Lett. 61 (18), 2015—2018. https://doi.org/10.1103/PhysRevLett.61.2015.
Han, J., et al., 2017. Room temperature spin-orbit torque switching induced by a topological insulator. arXiv. http://arxiv.org/abs/1703.07470. (Accessed 23 April 2017).
Han, G.H., et al., 2018. van der Waals metallic transition metal dichalcogenides. Chem. Rev. 118 (13), 6297—6336.
Hanbicki, A.T., et al., 2015. Measurement of high exciton binding energy in the monolayer transition-metal dichalcogenides WS2 and WSe2. Solid State Commun. 203, 16—20.
Hao, X., Moodera, J.S., Meservey, R., 1991. Thin-film superconductor in an exchange field. Phys. Rev. Lett. 67 (10), 1342—1345. https://doi.org/10.1103/PhysRevLett.67.1342.
Hao, Q., et al., 2020a. Visible to near-infrared photodetector with novel optoelectronic performance based on graphene/S-doped InSe heterostructure on h-BN substrate. Nanoscale 12 (37), 19259—19266. https://doi.org/10.1039/D0NR04338A.
Hao, S., et al., 2020b. Edge-epitaxial growth of InSe nanowires toward high-performance photodetectors. Small 16 (4). https://doi.org/10.1002/smll.201905902.
Harris, S.B., et al., 2023. Real-time diagnostics of 2D crystal transformations by pulsed laser deposition: controlled synthesis of Janus WSSe monolayers and alloys. ACS Nano 17 (3), 2472—2486.
Harrison, S.E., et al., 2014. Preparation of layered thin film samples for angle-resolved photoemission spectroscopy. Appl. Phys. Lett. 105 (12), 121608. https://doi.org/10.1063/1.4896632.
Harvey, A., et al., 2015. Preparation of gallium sulfide nanosheets by liquid exfoliation and their application as hydrogen evolution catalysts. Chem. Mater. 27 (9), 3483—3493. https://doi.org/10.1021/acs.chemmater.5b00910.
Hayat, A., et al., 2023. Recent advances, properties, fabrication and opportunities in two-dimensional materials for their potential sustainable applications. Energy Storage Mater. 59, 102780. https://doi.org/10.1016/j.ensm.2023.102780.
He, K., et al., 2010. Crossover of the three-dimensional topological insulator Bi2Se3 to the two-dimensional limit. Nat. Phys. 6 (8), 584—588. https://doi.org/10.1038/nphys1689.
Heifets, E., et al., 2000. Semi-empirical simulations of surface relaxation for perovskite titanates. Surf. Sci. 462 (1—3), 19—35. https://doi.org/10.1016/S0039-6028(00)00603-8.
Herbig, C., et al., 2021. Local electronic properties of coherent single-layer WS2/WSe2 lateral heterostructures. Nano Lett. 21 (6), 2363—2369.
Heremans, J.P., Cava, R.J., Samarth, N., 2017. Tetradymites as thermoelectrics and topological insulators. Nat. Rev. Mater. 2 (10), 17049. https://doi.org/10.1038/natrevmats.2017.49.
Hess, P., 2021. Bonding, structure, and mechanical stability of 2D materials: the predictive power of the periodic table. Nanoscale Horiz. 856—892. https://doi.org/10.1039/d1nh00113b.
Higashitarumizu, N., et al., 2020. Purely in-plane ferroelectricity in monolayer SnS at room temperature. Nat. Commun. 11 (1), 2428. https://doi.org/10.1038/s41467-020-16291-9.
Hill, H.M., et al., 2015. Observation of excitonic Rydberg states in monolayer MoS2 and WS2 by photoluminescence excitation spectroscopy. Nano Lett. 15 (5), 2992—2997.
Hilse, M., et al., 2024. Mixed polytype/polymorph formation and its effects on the electronic properties in InSe films grown by molecular beam epitaxy on GaAs(111)B. arXiv. http://arxiv.org/abs/2404.12578. (Accessed 21 April 2024).
Hong, W., et al., 2021. Wafer-scale uniform growth of an atomically thin MoS2 film with controlled layer numbers by metal—organic chemical vapor deposition. ACS Appl. Mater. Interfaces 13 (42), 50497—50504.
Hor, Y., et al., 2009. p-type Bi2Se3 for topological insulator and low-temperature thermoelectric applications. Phys. Rev. B 79 (19), 195208. https://doi.org/10.1103/PhysRevB.79.195208.
Hor, Y.S., et al., 2010. Development of ferromagnetism in the doped topological insulator Bi_{2-x}Mn_{x}Te_{3}. Phys. Rev. B 81 (19), 195203. https://doi.org/10.1103/PhysRevB.81.195203.
Hou, Y., et al., 2019. Millimetre-long transport of photogenerated carriers in topological insulators. Nat. Commun. 10 (1), 5723. https://doi.org/10.1038/s41467-019-13711-3.
Hou, Y., et al., 2022. Multifunctional two-dimensional van der Waals Janus magnet Cr-based dichalcogenide halides. Npj Computational Materials 8 (1), 120. https://doi.org/10.1038/s41524-022-00802-x.

Hsieh, D., et al., 2008. A topological Dirac insulator in a quantum spin Hall phase. Nature 452 (7190), 970–974. https://doi.org/10.1038/nature06843.
Hsieh, D., Xia, Y., Qian, D., et al., 2009a. A tunable topological insulator in the spin helical Dirac transport regime. Nature 460 (7259), 1101–1105. https://doi.org/10.1038/nature08234.
Hsieh, D., Xia, Y., Wray, L., et al., 2009b. Observation of unconventional quantum spin textures in topological insulators. Science 323 (5916), 919–922. https://doi.org/10.1126/science.1167733.
Hsieh, T.H., et al., 2012. Topological crystalline insulators in the SnTe material class. Nat. Commun. 3, 982. https://doi.org/10.1038/ncomms1969.
Hu, T., Dong, J., 2016. Two new phases of monolayer group-IV monochalcogenides and their piezoelectric properties. Phys. Chem. Chem. Phys. 18 (47), 32514–32520. https://doi.org/10.1039/C6CP06734D.
Hu, P., et al., 2012. Synthesis of few-layer GaSe nanosheets for high performance photodetectors. ACS Nano 6 (7), 5988–5994. https://doi.org/10.1021/nn300889c.
Hu, P., et al., 2013. Highly responsive ultrathin GaS nanosheet photodetectors on rigid and flexible substrates. Nano Lett. 13 (4), 1649–1654. https://doi.org/10.1021/nl400107k.
Hu, Z.-Y., et al., 2017. High thermoelectric performances of monolayer SnSe allotropes †. Nanoscale 9, 16093. https://doi.org/10.1039/c7nr04766e.
Hu, H., et al., 2019. Room-temperature out-of-plane and in-plane ferroelectricity of two-dimensional β-InSe nanoflakes. Appl. Phys. Lett. 114 (25). https://doi.org/10.1063/1.5097842.
Hu, H., et al., 2021. Out-of-plane and in-plane ferroelectricity of atom-thick two-dimensional InSe. Nanotechnology 32 (38). https://doi.org/10.1088/1361-6528/ac0ac5.
Hu, L., et al., 2022a. Solution-processed Ge(II)-based chalcogenide thin films with tunable bandgaps for photovoltaics †. Chem. Sci. https://doi.org/10.1039/d1sc07043f.
Hu, S., et al., 2022b. Reconfigurable InSe Electronics with van der Waals Integration. Adv. Electron. Mater. 8 (5). https://doi.org/10.1002/aelm.202101176.
Hu, J., et al., 2023. Chemical vapor deposition syntheses of wafer-scale 2D transition metal dichalcogenide films toward next-generation integrated circuits related applications. Adv. Funct. Mater. 33 (40), 2303520.
Huang, C., et al., 2013. Stable colloidal boron nitride nanosheet dispersion and its potential application in catalysis. J. Mater. Chem. A 1 (39), 12192. https://doi.org/10.1039/c3ta12231j.
Huang, C., et al., 2014. Lateral heterojunctions within monolayer MoSe 2–WSe 2 semiconductors. Nat. Mater. 13 (12), 1096–1101.
Huang, Y.T., et al., 2018. High-performance InSe transistors with ohmic contact enabled by nonrectifying barrier-type indium electrodes. ACS Appl. Mater. Interfaces 10 (39), 33450–33456. https://doi.org/10.1021/acsami.8b10576.
Huang, X., Liu, C., Zhou, P., 2022. 2D semiconductors for specific electronic applications: from device to system. Npj 2D Materials and Applications 6 (1), 51. https://doi.org/10.1038/s41699-022-00327-3.
Huyghebaert, C., et al., 2018. 2D materials: roadmap to CMOS integration. In: 2018 IEEE International Electron Devices Meeting (IEDM). IEEE, pp. 22.1.1–22.1.4. https://doi.org/10.1109/IEDM.2018.8614679.
Jaccodine, R., 1963. Surface energy of germanium and silicon. J. Electrochem. Soc. 110 (6). https://doi.org/10.1149/1.2425806.
Jain, A., et al., 2011. Formation enthalpies by mixing GGA and GGA + U calculations. Phys. Rev. B 84 (4), 045115. https://doi.org/10.1103/PhysRevB.84.045115.
Jain, A., et al., 2013. Commentary: the Materials Project: a materials genome approach to accelerating materials innovation. Apl. Mater. 1 (1). https://doi.org/10.1063/1.4812323.
Jancu, J.-M., et al., 2005. Atomistic spin-orbit coupling and k· p parameters in III-V semiconductors. Phys. Rev. B 72 (19), 193201.
Ji, H., et al., 2013. A ferromagnetic insulating substrate for the epitaxial growth of topological insulators. J. Appl. Phys. 114 (11), 114907. https://doi.org/10.1063/1.4822092.
Jia, S., Xu, S.-Y., Hasan, M.Z., 2016. Weyl semimetals, Fermi arcs and chiral anomalies. Nat. Mater. 15 (11), 1140–1144. https://doi.org/10.1038/nmat4787.
Jiang, Z., et al., 2015. Independent tuning of electronic properties and induced ferromagnetism in topological insulators with heterostructure approach. Nano Lett. 15 (9), 5835–5840. https://doi.org/10.1021/acs.nanolett.5b01905.
Jiang, Z., et al., 2016. Structural and proximity-induced ferromagnetic properties of topological insulator-magnetic insulator heterostructures. AIP Adv. 6 (5), 055809. https://doi.org/10.1063/1.4943061.
Jiang, J., et al., 2020. Concurrence of quantum anomalous Hall and topological Hall effects in magnetic topological insulator sandwich heterostructures. Nat. Mater. 1–6.
Jin, G., et al., 2021. Heteroepitaxial van der Waals semiconductor superlattices. Nat. Nanotechnol. 16 (10), 1092–1098.
Jones, A.M., et al., 2013. Optical generation of excitonic valley coherence in monolayer WSe2. Nat. Nanotechnol. 8 (9), 634–638.
Joshi, N., et al., 2018. A review on chemiresistive room temperature gas sensors based on metal oxide nanostructures, graphene and 2D transition metal dichalcogenides. Microchim. Acta 185, 1–16.
Jung, Y., et al., 2014. Metal seed layer thickness-induced transition from vertical to horizontal growth of MoS2 and WS2. Nano Lett. 14 (12), 6842–6849.
Jung, C.S., et al., 2015. Red-to-Ultraviolet emission tuning of two-dimensional gallium sulfide/selenide. ACS Nano 9 (10), 9585–9593. https://doi.org/10.1021/acsnano.5b04876.
Kalanyan, B., et al., 2017. Rapid wafer-scale growth of polycrystalline 2H-MoS2 by pulsed metal–organic chemical vapor deposition. Chem. Mater. 29 (15), 6279–6288. https://doi.org/10.1021/acs.chemmater.7b01367.
Kandala, A., 2015. Transport Studies of Mesoscopic and Magnetic Topological Insulators. Dissertation. The Pennsylvania State University. https://etda.libraries.psu.edu/catalog/26495.
Kandala, A., et al., 2013. Growth and characterization of hybrid insulating ferromagnet-topological insulator heterostructure devices. Appl. Phys. Lett. 103 (20), 202409. https://doi.org/10.1063/1.4831987.
Kandala, A., et al., 2015. Giant anisotropic magnetoresistance in a quantum anomalous Hall insulator. Nat. Commun. 6 (May), 7434. https://doi.org/10.1038/ncomms8434.
Kane, C.L., Mele, E.J., 2005. Quantum Spin hall effect in graphene. Phys. Rev. Lett. 95 (22), 226801. https://doi.org/10.1103/PhysRevLett.95.226801.
Kang, K., et al., 2015. High-mobility three-atom-thick semiconducting films with wafer-scale homogeneity. Nature 520 (7549), 656–660.
Kang, S., et al., 2020. 2D semiconducting materials for electronic and optoelectronic applications: potential and challenge. 2D Mater. 7 (2), 022003. https://doi.org/10.1088/2053-1583/AB6267.
Katmis, F., et al., 2016. A high-temperature ferromagnetic topological insulating phase by proximity coupling. Nature 533 (7604), 513–516. https://doi.org/10.1038/nature17635.
Kaxiras, E., Joannopoulos, J.D., 2019. Quantum Theory of Materials. Cambridge university press.
Khan, Y., et al., 2020. Recent breakthroughs in two-dimensional van der Waals magnetic materials and emerging applications. Nano Today 34, 100902. https://doi.org/10.1016/j.nantod.2020.100902.
Khang, N.H.D., Ueda, Y., Hai, P.N., 2018. A conductive topological insulator with large spin Hall effect for ultralow power spin–orbit torque switching. Nat. Mater. 17 (9), 808–813. https://doi.org/10.1038/s41563-018-0137-y.
Kim, H.W., 2023. Recent progress in the role of grain boundaries in two-dimensional transition metal dichalcogenides studied using scanning tunneling microscopy/spectroscopy. Appl. Microsc. 53 (1), 5. https://doi.org/10.1186/s42649-023-00088-3.
Kim, H., Choi, H.J., 2021. Quasiparticle band structures, spontaneous polarization, and spin-splitting in noncentrosymmetric few-layer and bulk γ-GeSe. J. Mater. Chem. C 9 (30), 9683–9691. https://doi.org/10.1039/D1TC01800K.
Kim, H., et al., 2017a. Suppressing nucleation in metal–organic chemical vapor deposition of MoS2 monolayers by alkali metal halides. Nano Lett. 17 (8), 5056–5063. https://doi.org/10.1021/acs.nanolett.7b02311.
Kim, J., et al., 2017b. Observation of ultralong valley lifetime in WSe2/MoS2 heterostructures. Sci. Adv. 3 (7) e1700518.
Kim, T., et al., 2017c. Wafer-scale production of highly uniform two-dimensional MoS2 by metal-organic chemical vapor deposition. Nanotechnology 28 (18), 18LT01.
Kim, K.S., et al., 2023. Non-epitaxial single-crystal 2D material growth by geometric confinement. Nature 614 (7946), 88–94.
King, P.D.C., et al., 2011. Large tunable Rashba spin splitting of a two-dimensional electron gas in Bi_{2}Se_{3}. Phys. Rev. Lett. 107 (9), 096802. https://doi.org/10.1103/PhysRevLett.107.096802.

Ko, K., et al., 2024. Native point defects in 2D transition metal dichalcogenides: a perspective bridging intrinsic physical properties and device applications. J. Appl. Phys. 135 (10), 100901. https://doi.org/10.1063/5.0185604.
Koirala, N., Brahlek, M., Salehi, M., Wu, L., Dai, J., Waugh, J., Nummy, T., Han, M.G., et al., 2015. Record surface state mobility and quantum Hall effect in topological insulator thin films via interface engineering. Nano Lett. 15 (12), 8245–8249. https://doi.org/10.1021/acs.nanolett.5b03770.
Komsa, H., Krasheninnikov, A.V., 2017. Engineering the electronic properties of two-dimensional transition metal dichalcogenides by introducing mirror twin boundaries. Adv. Electron. Mater. 3 (6). https://doi.org/10.1002/aelm.201600468.
König, M., et al., 2007. Quantum spin hall insulator state in HgTe quantum wells. Science (New York, N.Y.) 318 (5851), 766–770. https://doi.org/10.1126/science.1148047.
Koppens, F.H.L., et al., 2014. Photodetectors based on graphene, other two-dimensional materials and hybrid systems. Nat. Nanotechnol. 9 (10), 780–793.
Koskinen, K., et al., 2017. Bulk second-harmonic generation from thermally evaporated indium selenide thin films. Opt Lett. 42 (6), 1076. https://doi.org/10.1364/OL.42.001076.
Kou, X.F., et al., 2012. Magnetically doped semiconducting topological insulators. J. Appl. Phys. 112 (6), 63912.
Kou, X., et al., 2013. Interplay between different magnetisms in Cr-doped topological insulators. ACS Nano 7 (10), 9205–9212. https://doi.org/10.1021/nn4038145.
Kou, X., et al., 2014. Scale-invariant quantum anomalous Hall effect in magnetic topological insulators beyond the two-dimensional limit. Phys. Rev. Lett. 113 (13), 137201. https://doi.org/10.1103/PhysRevLett.113.137201.
Kübler, C., et al., 2004. Ultrabroadband detection of multi-terahertz field transients with GaSe electro-optic sensors: approaching the near infrared. Appl. Phys. Lett. 85 (16), 3360–3362. https://doi.org/10.1063/1.1808232.
Kuhn, A., Chevy, A., Chevalier, R., 1975. Crystal structure and interatomic distances in GaSe. Phys. Status Solidi 31 (2), 469–475. https://doi.org/10.1002/pssa.2210310216.
Külah, E., et al., 2021. The improved inverted AlGaAs/GaAs interface: its relevance for high-mobility quantum wells and hybrid systems. Semicond. Sci. Technol. 36 (8), 085013. https://doi.org/10.1088/1361-6641/ac0d98.
Kumikov, V.K., Khokonov, K.B., 1983. On the measurement of surface free energy and surface tension of solid metals. J. Appl. Phys. 54, 1346–1350. https://doi.org/10.1063/1.332209.
Kushwaha, S.K., et al., 2016. Sn-doped Bi1.1Sb0.9Te2S bulk crystal topological insulator with excellent properties. Nat. Commun. 7 (7), 11456. https://doi.org/10.1038/ncomms11456.
Kwak, T., et al., 2019. Growth behavior of wafer-scale two-dimensional MoS2 layer growth using metal-organic chemical vapor deposition. J. Cryst. Growth 510, 50–55.
Kylänpää, I., Komsa, H.-P., 2015. Binding energies of exciton complexes in transition metal dichalcogenide monolayers and effect of dielectric environment. Phys. Rev. B 92 (20), 205418.
Lai, Y.-Y., et al., 2021. Substrate lattice-guided MoS2 crystal growth: implications for van der Waals epitaxy. ACS Appl. Nano Mater. 4 (5), 4930–4938.
Lang, M., et al., 2014. Proximity induced high-temperature magnetic order in topological insulator–ferrimagnetic insulator heterostructure. Nano Lett. 14 (6), 3459–3465. https://doi.org/10.1021/nl500973k.
Lasek, K., et al., 2021. Synthesis and characterization of 2D transition metal dichalcogenides: recent progress from a vacuum surface science perspective. Surf. Sci. Rep. 76 (2), 100523.
Late, D.J., et al., 2012. GaS and GaSe Ultrathin Layer Transistors. Adv. Mater. 24 (26), 3549–3554. https://doi.org/10.1002/adma.201201361.
Latimer, K., et al., 2018. Evaluation of thermodynamic equations of state across chemistry and structure in the materials project. Npj Computational Materials 4 (1). https://doi.org/10.1038/s41524-018-0091-x.
Lebedev, A., 2018. Ferroelectricity and piezoelectricity in monolayers and nanoplatelets of SnS. J. Appl. Phys. 124, 164302. https://doi.org/10.1063/1.5035419.
Lee, W.E., Lagerlof, K.P.D., 1985. Structural and electron diffraction data for sapphire (α-al2o3). J. Electron. Microsc. Tech. 2 (3), 247–258.
Lee, J.S., Richardella, A., Rench, D.W., et al., 2014. Ferromagnetism and spin-dependent transport in n-type Mn-Bi2Te3 thin films. Phys. Rev. B 89 (17), 174425. http://arxiv.org/abs/1402.5546. (Accessed 16 March 2014).
Lee, E., Yoon, Y.S., Kim, D.-J., 2018. Two-dimensional transition metal dichalcogenides and metal oxide hybrids for gas sensing. ACS Sens. 3 (10), 2045–2060.
Lee, S.H., et al., 2019. Spin scattering and noncollinear spin structure-induced intrinsic anomalous Hall effect in antiferromagnetic topological insulator $MnBi_2Te_4$. Phys. Rev. Res. 1 (1), 12011. https://doi.org/10.1103/PhysRevResearch.1.012011.
Lee, S., et al., 2021. γ-GeSe: a new hexagonal polymorph from group IV-VI monochalcogenides. Nano Lett. 21 (10), 4305–4313. https://doi.org/10.1021/acs.nanolett.1c00714.
Lei, S., et al., 2013. Synthesis and photoresponse of large GaSe atomic layers. Nano Lett. 13 (6), 2777–2781. https://doi.org/10.1021/nl4010089.
Lei, S., et al., 2014. Evolution of the electronic band structure and efficient photo-detection in atomic layers of InSe. ACS Nano. https://doi.org/10.1021/nn405036u.
Lei, S., et al., 2015. An atomically layered InSe avalanche photodetector. Nano Lett. 15 (5), 3048–3055. https://doi.org/10.1021/acs.nanolett.5b00016.
Lemme, M.C., et al., 2022. 2D materials for future heterogeneous electronics. Nat. Commun. 13 (1), 1392. https://doi.org/10.1038/s41467-022-29001-4.
Li, H.D., et al., 2010. The van der Waals epitaxy of Bi2 Se3 on the vicinal Si(111) surface: an approach for preparing high-quality thin films of a topological insulator. New J. Phys. 12 (10), 103038. https://doi.org/10.1088/1367-2630/12/10/103038.
Li, H., et al., 2012. Carriers dependence of the magnetic properties in magnetic topological insulator Sb1. 95− x Bi x Cr0. 05Te3. Appl. Phys. Lett. 101 (7), 72406.
Li, B., et al., 2013. Carrier dependent ferromagnetism in chromium doped topological insulator. Phys. Lett. 377 (31–33), 1925–1929. https://doi.org/10.1016/j.physleta.2013.05.020.
Li, X., et al., 2014. Controlled vapor phase growth of single crystalline, two-dimensional GaSe crystals with high photoresponse. Sci. Rep. 4 (1), 5497. https://doi.org/10.1038/srep05497.
Li, H., et al., 2015. Optoelectronic crystal of artificial atoms in strain-textured molybdenum disulphide. Nat. Commun. 6 (1), 1–7.
Li, P., et al., 2017. Evidence for topological type-II Weyl semimetal WTe2. Nat. Commun. 8 (1), 2150.
Li, C., et al., 2018a. Excellent thermoelectricity performance of p-type SnSe along b axis. Phys. B Condens. Matter 530, 264–269. https://doi.org/10.1016/j.physb.2017.11.074.
Li, L., et al., 2018b. Wafer-scale fabrication of recessed-channel PtSe2 MOSFETs with low contact resistance and improved gate control. IEEE Trans. Electron. Dev. 65 (10), 4102–4108. https://doi.org/10.1109/TED.2018.2856305.
Li, J., et al., 2019a. Intrinsic magnetic topological insulators in van der Waals layered MnBi2Te4-family materials. Sci. Adv. 5 (6). https://doi.org/10.1126/sciadv.aaw5685.
Li, P., et al., 2019b. Magnetization switching using topological surface states. Sci. Adv. 5 (8). https://doi.org/10.1126/sciadv.aaw3415.
Li, J., et al., 2021a. Layer-dependent band gaps of platinum dichalcogenides. ACS Nano 15, 26. https://doi.org/10.1021/acsnano.1c02971.
Li, T., et al., 2021b. Epitaxial growth of wafer-scale molybdenum disulfide semiconductor single crystals on sapphire. Nat. Nanotechnol. 16 (11), 1201–1207.
Li, X., Hoffman, J.M., Kanatzidis, M.G., 2021c. The 2D halide Perovskite rulebook: how the spacer influences everything from the structure to optoelectronic device efficiency. Chem. Rev. 121 (4), 2230–2291. https://doi.org/10.1021/acs.chemrev.0c01006.
Li, L., Wang, Q., Wu, F., Xu, Q., Tian, J., Huang, Z., Wang, Q., Zhao, X., Zhang, Q., Fan, Q., et al., 2024. Epitaxy of wafer-scale single-crystal MoS2 monolayer via buffer layer control. Nat. Commun. 15 (1), 1825. https://doi.org/10.1038/s41467-024-46170-6.
Liang, J., et al., 2022. Controlled growth of two-dimensional heterostructures: in-plane epitaxy or vertical stack. Acc. Mater. Res. 3 (10), 999–1010.
Liao, Y., et al., 2020. Liquid-exfoliated few-layer InSe nanosheets for broadband nonlinear all-optical applications. Adv. Opt. Mater. 8 (9). https://doi.org/10.1002/adom.201901862.
Liebig, A., et al., 2024. Structural characterization of defects in the topological insulator Bi 2 Se 3 at the picometer scale. J. Phys. Chem. C 2022, 21716–21722. https://doi.org/10.1021/acs.jpcc.2c06084.
Lim, S.Y., et al., 2020. Polytypism in few-layer gallium selenide. Nanoscale 12 (15), 8563–8573. https://doi.org/10.1039/D0NR00165A.
Lin, Y.C., et al., 2012. Wafer-scale MoS2 thin layers prepared by MoO3 sulfurization. Nanoscale 4 (20), 6637–6641. https://doi.org/10.1039/c2nr31833d.
Lin, Y., et al., 2014. Dielectric screening of excitons and trions in single-layer MoS2. Nano Lett. 14 (10), 5569–5576.

Lin, Y.-C., et al., 2015. Single-layer ReS2: two-dimensional semiconductor with tunable in-plane anisotropy. ACS Nano 9 (11), 11249–11257.
Lin, Z., et al., 2016. Defect engineering of two-dimensional transition metal dichalcogenides. 2D Mater. 3 (2), 022002. https://doi.org/10.1088/2053-1583/3/2/022002.
Lin, Y.-C., et al., 2018. Realizing large-scale, electronic-grade two-dimensional semiconductors. ACS Nano 12 (2), 965–975.
Lin, Y., et al., 2021. Controllable thin-film approaches for doping and alloying transition metal dichalcogenides monolayers. Adv. Sci. 8 (9), 2004249.
Liu, Q.K.K., et al., 1999. Equilibrium shapes and energies of coherent strained InP islands. Phys. Rev. B 60 (17008). https://doi.org/10.1103/PhysRevB.60.17008.
Liu, L., et al., 2012a. Spin-torque switching with the giant spin Hall effect of tantalum. Science 336 (6081), 555–558. https://doi.org/10.1126/science.1218197.
Liu, M., et al., 2012b. Crossover between weak antilocalization and weak localization in a magnetically doped topological insulator. Phys. Rev. Lett. 108 (3), 036805. https://doi.org/10.1103/PhysRevLett.108.036805.
Liu, L., et al., 2016a. Atomic MoS 2 monolayers synthesized from a metal–organic complex by chemical vapor deposition. Nanoscale 8 (8), 4486–4490.
Liu, M., et al., 2016b. Large discrete jumps observed in the transition between Chern states in a ferromagnetic topological insulator. Sci. Adv. 2 (7) e1600167–e1600167.
Liu, C., et al., 2017. Dimensional crossover-induced topological Hall effect in a magnetic topological insulator. Phys. Rev. Lett. 119 (17), 176809.
Liu, C., et al., 2020. Robust axion insulator and Chern insulator phases in a two-dimensional antiferromagnetic topological insulator. Nat. Mater. 19 (5), 522–527. https://doi.org/10.1038/s41563-019-0573-3.
Liu, D.S.H., Hilse, M., Engel-Herbert, R., 2021. Sticking coefficients of selenium and tellurium. J. Vac. Sci. Technol. A 39 (2), 023413. https://doi.org/10.1116/6.0000736.
Liu, L., et al., 2022. Uniform nucleation and epitaxy of bilayer molybdenum disulfide on sapphire. Nature 605 (7908), 69–75.
Liu, D.S.H., et al., 2023a. Growth of nanometer-thick γ-InSe on Si(111) 7 × 7 by molecular beam epitaxy for field-effect transistors and optoelectronic devices. ACS Appl. Nano Mater. 6 (16), 15029–15037. https://doi.org/10.1021/acsanm.3c02602.
Liu, P., et al., 2023b. Recent advances in 2D van der Waals magnets: Detection, modulation, and applications. iScience 26 (9), 107584. https://doi.org/10.1016/j.isci.2023.107584.
Liu, S., et al., 2023c. Two-step flux synthesis of ultrapure transition-metal dichalcogenides. ACS Nano 17 (17), 16587–16596.
Logsdail, A.J., et al., 2015. Structural, energetic and electronic properties of (100) surfaces for alkaline earth metal oxides as calculated with hybrid density functional theory. Surf. Sci. 642, 58–65. https://doi.org/10.1016/j.susc.2015.06.012.
Loh, L., et al., 2021. Substitutional doping in 2D transition metal dichalcogenides. Nano Res. 14, 1668–1681.
Long, M., et al., 2019. Progress, challenges, and opportunities for 2D material based photodetectors. Adv. Funct. Mater. 29 (19), 1803807.
Lu, A.-Y., et al., 2017. Janus monolayers of transition metal dichalcogenides. Nat. Nanotechnol. 12 (8), 744–749.
Luo, J., et al., 2023. Exploring the epitaxial growth kinetics and anomalous hall effect in magnetic topological insulator $MnBi_2Te_4$ films. ACS Nano 17 (19). https://doi.org/10.1021/acsnano.3c04626.
Ly, T.H., et al., 2016. Misorientation-angle-dependent electrical transport across molybdenum disulfide grain boundaries. Nat. Commun. 7 (1), 10426. https://doi.org/10.1038/ncomms10426.
Ma, J., et al., 2019. Experimental progress on layered topological semimetals. 2D Mater. 6 (3), 032001. https://doi.org/10.1088/2053-1583/ab0902.
Ma, Z., et al., 2020. Epitaxial growth of rectangle shape MoS2 with highly aligned orientation on twofold symmetry a-plane sapphire. Small 16 (16), 2000596.
Mak, K.F., Shan, J., 2016. Photonics and optoelectronics of 2D semiconductor transition metal dichalcogenides. Nat. Photonics 10 (4), 216–226. https://doi.org/10.1038/nphoton.2015.282.
Mak, K.F., et al., 2010. Atomically thin MoS 2: a new direct-gap semiconductor. Phys. Rev. Lett. 105 (13), 136805.
Mak, K.F., et al., 2012. Control of valley polarization in monolayer MoS2 by optical helicity. Nat. Nanotechnol. 7 (8), 494–498.
Man, P., et al., 2021. Functional grain boundaries in two-dimensional transition-metal dichalcogenides. Accounts Chem. Res. 54 (22), 4191–4202. https://doi.org/10.1021/acs.accounts.1c00519.
Manna, S., et al., 2018. Large piezoelectric response of van der Waals layered solids. J. Mater. Chem. C 6 (41), 11035–11044. https://doi.org/10.1039/C8TC02560F.
Mao, L., Stoumpos, C.C., Kanatzidis, M.G., 2019a. Two-dimensional hybrid halide perovskites: principles and promises. J. Am. Chem. Soc. 141 (3), 1171–1190. https://doi.org/10.1021/jacs.8b10851.
Mao, Y., et al., 2019b. A two-dimensional GeSe/SnSe heterostructure for high performance thin-film solar cells †. J. Mater. Chem. A. https://doi.org/10.1039/c9ta01219b.
Marx, M., et al., 2018. Metalorganic vapor-phase epitaxy growth parameters for two-dimensional MoS2. J. Electron. Mater. 47 (2), 910–916.
McCreary, K.M., et al., 2018. A-and B-exciton photoluminescence intensity ratio as a measure of sample quality for transition metal dichalcogenide monolayers. Apl. Mater. 6 (11), 111106.
McKinney, R.W., et al., 2018. Ionic vs. van der Waals layered materials: identification and comparison of elastic anisotropy. J. Mater. Chem. A 6 (32), 15828–15838. https://doi.org/10.1039/C8TA04933E.
Medrano Sandonas, L., et al., 2016. Anisotropic thermoelectric response in two-dimensional puckered structures. J. Phys. Chem. C 120 (33), 18841–18849. https://doi.org/10.1021/acs.jpcc.6b04969.
Mellnik, A.R., et al., 2014. Spin-transfer torque generated by a topological insulator. Nature 511 (7510), 449–451. https://doi.org/10.1038/nature13534.
Merchant, A., et al., 2023. Scaling deep learning for materials discovery. Nature 624 (7990), 80–85. https://doi.org/10.1038/s41586-023-06735-9.
Mermin, N., Wagner, H., 1966. Absence of ferromagnetism or antiferromagnetism in one- or two-dimensional isotropic heisenberg models. Phys. Rev. Lett. 17 (22), 1133–1136. https://doi.org/10.1103/PhysRevLett.17.1133.
Minhas, H., et al., 2022. Ultralow thermal conductivity and high thermoelectric performance of γ-GeSe: effects of dimensionality and thickness. ACS Appl. Energy Mater. 5 (8). https://doi.org/10.1021/acsaem.2c01600.
Mo, J., et al., 2020a. Importance of the substrate's surface evolution during the MOVPE growth of 2D-transition metal dichalcogenides. Nanotechnology 31 (12), 125604.
Mogi, M., et al., 2015. Magnetic modulation doping in topological insulators toward higher-temperature quantum anomalous Hall effect. Appl. Phys. Lett. 107 (18), 182401. https://doi.org/10.1063/1.4935075.
Mogi, M., et al., 2017. Tailoring tricolor structure of magnetic topological insulator for robust axion insulator. Sci. Adv. 3 (10), eaao1669. https://doi.org/10.1126/sciadv.aao1669.
Mogi, M., et al., 2018. Ferromagnetic insulator Cr2Ge2Te6 thin films with perpendicular remanence. Apl. Mater. 6 (9), 91104. https://doi.org/10.1063/1.5046166.
Mogi, M., et al., 2019. Large anomalous Hall effect in topological insulators with proximitized ferromagnetic insulators. Phys. Rev. Lett. 123 (1), 16804. https://doi.org/10.1103/PhysRevLett.123.016804.
Momma, K., Izumi, F., 2011. VESTA 3 for three-dimensional visualization of crystal, volumetric and morphology data. J. Appl. Crystallogr. 44 (6), 1272–1276.
Morin, C., et al., 2015. Polymorphism in thermoelectric As_2 Te_3. Inorg. Chem. 54 (20), 9936–9947. https://doi.org/10.1021/acs.inorgchem.5b01676.
Mortelmans, W., et al., 2019. Peculiar alignment and strain of 2D WSe2 grown by van der Waals epitaxy on reconstructed sapphire surfaces. Nanotechnology 30 (46), 465601.
Mortelmans, W., et al., 2020a. Epitaxial registry and crystallinity of MoS2 via molecular beam and metalorganic vapor phase van der Waals epitaxy. Appl. Phys. Lett. 117 (3).
Mortelmans, W., Nalin Mehta, A., et al., 2020b. Fundamental limitation of van der Waals homoepitaxy by stacking fault formation in WSe2. 2D Mater. 7 (2), 025027. https://doi.org/10.1088/2053-1583/ab70ec.
Mortelmans, W., et al., 2021. Epitaxy of 2D chalcogenides: Aspects and consequences of weak van der Waals coupling. Appl. Mater. Today 22, 100975. https://doi.org/10.1016/j.apmt.2021.100975.
Mounet, N., et al., 2018. Two-dimensional materials from high-throughput computational exfoliation of experimentally known compounds. Nat. Nanotechnol. 13 (3), 246–252. https://doi.org/10.1038/s41565-017-0035-5.
Mudd, G.W., et al., 2015. High Broad-Band Photoresponsivity of Mechanically Formed InSe–Graphene van der Waals Heterostructures. Adv. Mater. 27 (25), 3760–3766. https://doi.org/10.1002/adma.201500889.

Mun, J., et al., 2016. Low-temperature growth of layered molybdenum disulphide with controlled clusters. Sci. Rep. 6 (1), 1–7.
Murgatroyd, P.A.E., et al., 2020. GeSe: Optical Spectroscopy and Theoretical Study of a van der Waals Solar Absorber. Chem. Mater. 32 (7), 3245–3253. https://doi.org/10.1021/acs.chemmater.0c00453.
Nam, S.B., et al., 1976. Free-exciton energy spectrum in GaAs. Phys. Rev. B 13 (2), 761.
Narang, P., Garcia, C.A.C., Felser, C., 2021. The topology of electronic band structures. Nat. Mater. 20 (3), 293–300. https://doi.org/10.1038/s41563-020-00820-4.
National Science and Technology Council, 2021. The 2021 Materials Genome Initiative Strategic Plan.
Navrátil, J., et al., 2004. Conduction band splitting and transport properties of Bi2Se3. J. Solid State Chem. 177 (4–5), 1704–1712. https://doi.org/10.1016/j.jssc.2003.12.031.
Neupane, G.P., et al., 2019. In-plane isotropic/anisotropic 2D van der Waals heterostructures for future devices. Small 15 (11), 1804733.
Nicolosi, V., et al., 2013. Liquid exfoliation of layered materials. Science 340 (6139), 1226419.
Nie, Y., Barton, A.T., et al., 2018. Dislocation driven spiral and non-spiral growth in layered chalcogenides. Nanoscale 10 (31), 15023–15034. https://doi.org/10.1039/C8NR02280A.
Noh, J.-Y., et al., 2015. Deep-to-shallow level transition of Re and Nb dopants in monolayer MoS 2 with dielectric environments. Phys. Rev. B 92 (11), 115431.
Novoselov, K.S., et al., 2005. Two-dimensional atomic crystals. Proc. Nat. Acad. Sci. 102 (30), 10451–10453.
Novoselov, K.S., et al., 2016. 2D materials and van der Waals heterostructures. Science 353 (6298) aac9439.
Ohtake, A., Mano, T., Sakuma, Y., 2020. Strain relaxation in InAs heteroepitaxy on lattice-mismatched substrates. Sci. Rep. 10 (1), 4606. https://doi.org/10.1038/s41598-020-61527-9.
Okamoto, H., 1998. Se-Sn (selenium-tin). J. Phase Equilib. 19 (3). https://doi.org/10.1361/105497198770342544.
Okamoto, H., 2000. Ge-Se (germanium-selenium). J. Phase Equilib. 21 (3). https://doi.org/10.1361/105497100770340129.
Okamoto, H., 2004. In-Se (indium-selenium). J. Phase Equilib. Diffus. 25 (2). https://doi.org/10.1007/s11669-004-0031-y.
Okamoto, H., 2009. Ga-Se (gallium-selenium). J. Phase Equilib. Diffus. 30 (6). https://doi.org/10.1007/s11669-009-9601-3.
Okazaki, Y., et al., 2022. Quantum anomalous Hall effect with a permanent magnet defines a quantum resistance standard. Nat. Phys. 18 (1), 25–29. https://doi.org/10.1038/s41567-021-01424-8.
Ortiz-Cervantes, C., Carmona-Monroy, P., Solis-Ibarra, D., 2019. Two-dimensional halide perovskites in solar cells: 2D or not 2D? ChemSusChem 12 (8), 1560–1575. https://doi.org/10.1002/cssc.201802992.
Otrokov, M.M., Klimovskikh, I.I., et al., 2019a. Prediction and observation of an antiferromagnetic topological insulator. Nature 576 (7787), 416–422. https://doi.org/10.1038/s41586-019-1840-9.
Otrokov, M.M., Rusinov, I.P., et al., 2019b. Unique Thickness-Dependent Properties of the van der Waals Interlayer Antiferromagnet $MnBi_2Te_4$ Films. Phys. Rev. Lett. 122 (10), 107202. https://doi.org/10.1103/PhysRevLett.122.107202.
Ou, Y., et al., 2022. ZrTe2/CrTe2: an epitaxial van der Waals platform for spintronics. Nat. Commun. 13 (1), 2972. https://doi.org/10.1038/s41467-022-30738-1.
O'Hara, D.J., et al., 2018. Room temperature intrinsic ferromagnetism in epitaxial manganese selenide films in the monolayer limit. Nano Lett. 18 (5), 3125–3131. https://doi.org/10.1021/acs.nanolett.8b00683.
Pan, H., et al., 2019. Broadband nonlinear optical response of InSe nanosheets for the pulse generation from 1 to 2 μm. ACS Appl. Mater. Interfaces. https://doi.org/10.1021/acsami.9b18632.
Park, S., et al., 2018. Direct determination of monolayer MoS 2 and WSe 2 exciton binding energies on insulating and metallic substrates. 2D Mater. 5 (2), 25003.
Park, J., et al., 2021. Synthesis of high-performance monolayer molybdenum disulfide at low temperature. Small Methods 5 (6), 2000720.
Park, Y., et al., 2023a. Critical role of surface termination of sapphire substrates in crystallographic epitaxial growth of MoS2 using inorganic molecular precursors. ACS Nano 17 (2), 1196–1205.
Park, Y., Li, N., Jung, D., Singh, L.T., Baik, J., Lee, E., Oh, D., Kim, Y.D., Lee, J.Y., Woo, J., et al., 2023b. Unveiling the origin of n-type doping of natural MoS2: carbon. Npj 2D Materials and Applications 7 (1), 60. https://doi.org/10.1038/s41699-023-00424-x.
Patil, V., et al., 2021. High mobility field-effect transistors based on MoS2 crystals grown by the flux method. Nanotechnology 32 (32), 325603.
Pauling, L., 1975. The formula, structure, and chemical bonding of tetradymite, Bi14Te13S8, and the phase Bi14Te15S6. Am. Mineral. 60, 994–997.
Pearson, R.K., Haugen, G.R., 1981. Kinetics of the thermal decomposition of H2Se. Int. J. Hydrogen Energy 6 (5), 509–519.
Peters, L., et al., 2020. Directing the morphology of chemical vapor deposition-grown MoS2 on sapphire by crystal plane selection. Physica Status Solidi (A) 217 (15), 2000073.
Pielić, B., et al., 2020. Sulfur structures on bare and graphene-covered Ir (111). J. Phys. Chem. C 124 (12), 6659–6668.
Pisoni, A., et al., 2015. The role of transport agents in MoS2 single crystals. J. Phys. Chem. C 119 (8), 3918–3922.
Priydarshi, A., et al., 2022. Strain-tunable in-plane ferroelectricity and lateral tunnel junction in monolayer group-IV monochalcogenides. J. Appl. Phys. 131 (3). https://doi.org/10.1063/5.0072124.
Qian, X., et al., 2014. Quantum spin Hall effect in two-dimensional transition metal dichalcogenides. Science 346 (6215), 1344–1347. https://doi.org/10.1126/science.1256815.
Qiu, G., et al., 2022. The resurrection of tellurium as an elemental two-dimensional semiconductor. Npj 2D Materials and Applications 6 (1), 17. https://doi.org/10.1038/s41699-022-00293-w.
Radamson, H.H., et al., 2020. State of the art and future perspectives in advanced CMOS technology. Nanomaterials 10 (8), 1555. https://doi.org/10.3390/nano10081555.
Rai-Choudhury, P., Noreika, A.J., 1969. Hydrogen sulfide as an etchant for silicon. J. Electrochem. Soc. 116 (4), 539.
Rajan, A., et al., 2020. Morphology control of epitaxial monolayer transition metal dichalcogenides. Phys. Rev. Mater. 4 (1), 014003. https://doi.org/10.1103/PhysRevMaterials.4.014003.
Ramasamy, P., et al., 2016. Solution synthesis of GeS and GeSe nanosheets for high-sensitivity photodetectors. J. Mater. Chem. C 4 (3), 479–485. https://doi.org/10.1039/C5TC03667D.
Rathod, N., Hatzikiriakos, S., 2004. The effect of surface energy of boron nitride on polymer processability. Polym. Eng. Sci. 44 (8), 1543–1550. https://doi.org/10.1002/pen.20151.
Reifsnyder Hickey, D., et al., 2021. Illuminating invisible grain boundaries in coalesced single-orientation WS 2 monolayer films. Nano Lett. 21, 6495. https://doi.org/10.1021/acs.nanolett.1c01517.
Ren, Z., et al., 2010. Large bulk resistivity and surface quantum oscillations in the topological insulator Bi_2Te_2Se. Phys. Rev. B 82 (24), 241306. https://doi.org/10.1103/PhysRevB.82.241306.
Ribeiro-Soares, J., et al., 2014. Group theory analysis of phonons in two-dimensional transition metal dichalcogenides. Phys. Rev. B 90 (11), 115438.
Richardella, A., et al., 2015. Characterizing the structure of topological insulator thin films. Apl. Mater. 3 (8), 083303. https://doi.org/10.1063/1.4926455.
Rivera, P., et al., 2015. Observation of long-lived interlayer excitons in monolayer MoSe2–WSe2 heterostructures. Nat. Commun. 6 (1), 1–6.
Rivera, P., et al., 2018. Interlayer valley excitons in heterobilayers of transition metal dichalcogenides. Nat. Nanotechnol. 13 (11), 1004–1015.
Ross, J.S., et al., 2013. Electrical control of neutral and charged excitons in a monolayer semiconductor. Nat. Commun. 4 (1), 1474.
Roychowdhury, S., et al., 2018. Germanium chalcogenide thermoelectrics: electronic structure modulation and low lattice thermal conductivity †. Chem. Mater. https://doi.org/10.1021/acs.chemmater.8b02676.
RŮžička, J., et al., 2015a. Structural and electronic properties of manganese-doped Bi2Te3 epitaxial layers. New J. Phys. 17 (1), 13028.
Sadan, H., Kaplan, W.D., 2006. Au–Sapphire (0001) solid–solid interfacial energy. J. Mat. Sci. 41, 5099–5107. https://doi.org/10.1007/s10853-006-0437-5.
Samal, R., Rout, C.S., 2020. Recent developments on emerging properties, growth approaches, and advanced applications of metallic 2D layered vanadium dichalcogenides. Adv. Mater. Interf. 7 (8). https://doi.org/10.1002/admi.201901682.

Sarkar, A.S., Stratakis, E., 2020. Recent advances in 2D metal monochalcogenides. Adv. Sci. 7 (21). https://doi.org/10.1002/advs.202001655.

Schaefer, C.M., et al., 2021. Carbon incorporation in MOCVD of MoS2 thin films grown from an organosulfide precursor. Chem. Mater. 33 (12), 4474—4487.

Schönfeld, B., Huang, J.J., Moss, S.C., 1983. Anisotropic mean-square displacements (MSD) in single-crystals of 2H-and 3R-MoS2. Acta Crystallogr. Sect. B Struct. Sci. 39 (4), 404—407.

Schreyeck, S., et al., 2013. Molecular beam epitaxy of high structural quality Bi2Se3 on lattice matched InP(111) substrates. Appl. Phys. Lett. 102 (4), 041914. https://doi.org/10.1063/1.4789775.

Sebastian, A., et al., 2021. Benchmarking monolayer MoS2 and WS2 field-effect transistors. Nat. Commun. 12 (1), 1—12.

Segev, E., et al., 2018. Surface energies and nanocrystal stability in the orthorhombic and π-phases of tin and germanium monochalcogenides. CrystEngComm 20 (30), 4237—4248. https://doi.org/10.1039/C8CE00710A.

Shafique, A., Shin, Y.-H., 2017. Thermoelectric and phonon transport properties of two-dimensional IV—VI compounds. Sci. Rep. 7 (1), 506. https://doi.org/10.1038/s41598-017-00598-7.

Shalf, J., 2020. The future of computing beyond Moore's Law. Phil. Trans. Math. Phys. Eng. Sci. 378 (2166), 20190061.

Shang, H., et al., 2020. A mixed-dimensional 1D Se—2D InSe van der Waals heterojunction for high responsivity self-powered photodetectors. Nanoscale Horiz. 5 (3), 564—572. https://doi.org/10.1039/C9NH00705A.

Shankar, M.R., Prabhu, A.N., 2023. A review on structural characteristics and thermoelectric properties of mid-temperature range Chalcogenide-based thermoelectric materials. J. Mater. Sci. 58 (43), 16591—16633. https://doi.org/10.1007/s10853-023-09028-8.

Shi, H., et al., 2015. Connecting thermoelectric performance and topological-insulator behavior: Bi_2Te_3 and Bi_2Te_2Se from first principles. Phys. Rev. Appl. 3 (1), 014004. https://doi.org/10.1103/PhysRevApplied.3.014004.

Shi, L.-B., et al., 2020. Theoretical prediction of intrinsic electron mobility of monolayer InSe: first-principles calculation. J. Phys. Condens. Matter 32 (6), 065306. https://doi.org/10.1088/1361-648X/ab534f.

Shi, Y., et al., 2021. Engineering wafer-scale epitaxial two-dimensional materials through sapphire template screening for advanced high-performance nanoelectronics. ACS Nano 15 (6), 9482—9494.

Shiffa, M., et al., 2024. Wafer-scale two-dimensional semiconductors for deep UV sensing. Small 20 (7). https://doi.org/10.1002/smll.202305865.

Shimada, T., Ohuchi, F.S., Parkinson, B.A., 1992. Thermal decomposition of SnS2 and SnSe2: novel molecular-beam epitaxy sources for sulfur and selenium. J. Vac. Sci. Technol. A 10 (3), 539—542.

Shin, D., et al., 2016. BaCu2Sn(S,Se)4: earth-abundant chalcogenides for thin-film photovoltaics. Chem. Mater. 28 (13), 4771—4780. https://doi.org/10.1021/acs.chemmater.6b01832.

Simonson, N.A., et al., 2018. Low-temperature metalorganic chemical vapor deposition of molybdenum disulfide on multicomponent glass substrates. FlatChem 11, 32—37.

Singh, A., Singh, A.K., 2019. Origin of n-type conductivity of monolayer MoS2. Phys. Rev. B 99 (12), 121201. https://doi.org/10.1103/PhysRevB.99.121201.

Singh, P., et al., 2022. Two-Dimensional ClPS-InSe van der Waal Heterostructure Ferroelectric Field Effect Transistor for Nonvolatile Memory Applications. ACS Nano 16 (4), 5418—5426. https://doi.org/10.1021/acsnano.1c09136.

Smets, Q., et al., 2019. Ultra-scaled MOCVD MoS 2 MOSFETs with 42nm contact pitch and 250μA/μm drain current. In: 2019 IEEE International Electron Devices Meeting (IEDM). IEEE, pp. 22—23.

Stanford, M.G., Rack, P.D., Jariwala, D., 2018. Emerging nanofabrication and quantum confinement techniques for 2D materials beyond graphene. In: Npj 2D Materials and Applications. Nature Publishing Group.

Stevens, C.E., et al., 2018. Biexcitons in monolayer transition metal dichalcogenides tuned by magnetic fields. Nat. Commun. 9 (1), 3720.

Su, T., et al., 2018. Role of interfaces in two-dimensional photocatalyst for water splitting. ACS Catal. 8 (3), 2253—2276.

Sucharitakul, S., et al., 2015. Intrinsic electron mobility exceeding 10 ^{3} cm ^{2}/(V s) in multilayer InSe FETs. Nano Lett. 15 (6), 3815—3819. https://doi.org/10.1021/acs.nanolett.5b00493.

Sucharitakul, S., et al., 2017. V 2 O 5: A 2D van der Waals Oxide with Strong In-Plane Electrical and Optical Anisotropy. ACS Appl. Mater. Interfaces 9, 27. https://doi.org/10.1021/acsami.7b05377.

Sun, Y., et al., 2016a. Strong intrinsic spin Hall effect in the TaAs family of Weyl semimetals. Phys. Rev. Lett. 117 (14), 146403. https://doi.org/10.1103/PhysRevLett.117.146403.

Sun, Y., Wang, D., Shuai, Z., 2016b. Indirect-to-direct band gap crossover in few-layer transition metal dichalcogenides: a theoretical prediction. J. Phys. Chem. C 120 (38), 21866—21870.

Sun, Y., et al., 2018. InSe: a two-dimensional material with strong interlayer coupling. Nanoscale 10 (17), 7991—7998. https://doi.org/10.1039/C7NR09486H.

Tan, S.M., et al., 2016. Electrochemistry of layered GaSe and GeS: applications to ORR, OER and HER †. Phys. Chem. Chem. Phys. 18, 1699. https://doi.org/10.1039/c5cp06682d.

Tanaka, Y., et al., 2012. Experimental realization of a topological crystalline insulator in SnTe. Nat. Phys. 8 (11), 800—803. https://doi.org/10.1038/nphys2442.

Tang, C., et al., 2017. Above 400-K robust perpendicular ferromagnetic phase in a topological insulator. Sci. Adv. 3 (6). https://doi.org/10.1126/sciadv.1700307.

Tang, K., et al., 2022a. High-Throughput Calculation of Interlayer van der Waals Forces Validated with Experimental Measurements. Research 2022. https://doi.org/10.34133/2022/9765121.

Tang, S., et al., 2022b. Detailed study on MOCVD of wafer-scale MoS2 monolayers: from nucleation to coalescence. MRS Adv. 1—6.

Tarakina, N.V., et al., 2014. Suppressing twin formation in Bi2Se3 thin films. Adv. Mater. Interfac. 1 (5). https://doi.org/10.1002/admi.201400134.

Tebyetekerwa, M., et al., 2020. Mechanisms and applications of steady-state photoluminescence spectroscopy in two-dimensional transition-metal dichalcogenides. ACS Nano 14 (11), 14579—14604.

Thiery, N., et al., 2018. Electrical properties of epitaxial yttrium iron garnet ultrathin films at high temperatures. Phys. Rev. B 97 (6), 64422. https://doi.org/10.1103/PhysRevB.97.064422.

Thouless, D.J., et al., 1982. Quantized Hall conductance in a two-dimensional periodic potential. Phys. Rev. Lett. 49 (6), 405—408. https://doi.org/10.1103/PhysRevLett.49.405.

Tian, H., et al., 2016. Low-symmetry two-dimensional materials for electronic and photonic applications. Nano Today 11 (6), 763—777. https://doi.org/10.1016/j.nantod.2016.10.003.

Titova, L.V., et al., 2020. 5 - Group-IV monochalcogenides GeS, GeSe, SnS, SnSe. Chalcogenide 119—151. From 3D to 2D and Beyond Woodhead Publishing Series in Electronic and Optical Materials. https://doi.org/10.1016/B978-0-08-102687-8.00007-5.

Tongay, S., et al., 2013. Defects activated photoluminescence in two-dimensional semiconductors: interplay between bound, charged, and free excitons. Sci. Rep. https://doi.org/10.1038/srep02657.

Tsuda, M., et al., 2003. Mechanism of H2 pre-annealing on the growth of GaN on sapphire by MOVPE. Appl. Surf. Sci. 216 (1—4), 585—589.

Turker, F., et al., 2023. 2D oxides realized via confinement heteroepitaxy. Adv. Funct. Mater. 33 (5). https://doi.org/10.1002/adfm.202210404.

Ubaldini, A., Giannini, E., 2014. Improved chemical vapor transport growth of transition metal dichalcogenides. J. Cryst. Growth 401, 878—882.

Ubaldini, A., et al., 2013. Chloride-driven chemical vapor transport method for crystal growth of transition metal dichalcogenides. Cryst. Growth Des. 13 (10), 4453—4459.

Ueno, K., 2015. Introduction to the growth of bulk single crystals of two-dimensional transition-metal dichalcogenides. J. Phys. Soc. Jpn. 84 (12), 121015.

Ugeda, M.M., et al., 2014. Giant bandgap renormalization and excitonic effects in a monolayer transition metal dichalcogenide semiconductor. Nat. Mater. 13 (12), 1091—1095. https://doi.org/10.1038/nmat4061.

Haq, B.U., et al., 2018. Thermoelectric properties of the novel cubic structured silicon monochalcogenides: a first-principles study. J. Alloys Compd. 769, 413—419. https://doi.org/10.1016/j.jallcom.2018.07.325.

Unzueta, I., et al., 2016. Observation of a charge delocalization from Se vacancies in Bi2Se3: a positron annihilation study of native defects. Phys. Rev. B 94 (1), 014117. https://doi.org/10.1103/PhysRevB.94.014117.
Vaitkus, J.A., Ho, C.S., Cole, J.H., 2022. Effect of magnetic impurity scattering on transport in topological insulators. Phys. Rev. B 106 (11), 115420. https://doi.org/10.1103/PhysRevB.106.115420.
Van der Donck, M., Zarenia, M., Peeters, F.M., 2018. Excitons, trions, and biexcitons in transition-metal dichalcogenides: magnetic-field dependence. Phys. Rev. B 97 (19), 195408.
Velický, M., Toth, P.S., 2017. From two-dimensional materials to their heterostructures: an electrochemist's perspective. Appl. Mater. Today 8, 68–103. https://doi.org/10.1016/j.apmt.2017.05.003.
Veyrat, L., et al., 2015. Band bending inversion in Bi 2 Se 3 nanostructures. Nano Lett. 15 (11), 7503–7507. https://doi.org/10.1021/acs.nanolett.5b03124.
Villaos, R.A.B., et al., 2019. Thickness dependent electronic properties of Pt dichalcogenides. Npj 2D Materials and Applications 3 (1), 2. https://doi.org/10.1038/s41699-018-0085-z.
Vitale, S.A., et al., 2018. Valleytronics: opportunities, challenges, and paths forward. Small 14 (38). https://doi.org/10.1002/smll.201801483.
Von Rohr, F.O., et al., 2017. High-pressure synthesis and characterization of β-GeSeA six-membered-ring semiconductor in an uncommon boat conformation. J. Am. Chem. Soc. https://doi.org/10.1021/jacs.6b12828.
Walsh, L.A., et al., 2018. Molecular beam epitaxy of transition metal dichalcogenides. In: Molecular Beam Epitaxy. Elsevier, pp. 515–531. https://doi.org/10.1016/b978-0-12-812136-8.00024-4.
Wan, Y., et al., 2022. Wafer-scale single-orientation 2D layers by atomic edge-guided epitaxial growth. Chem. Soc. Rev. 51 (3), 803–811. https://doi.org/10.1039/D1CS00264C.
Wang, S., Zhang, P., 2020. Native point defects in Bi 2 Se 3: a first-principles study. Phys. Lett. 384, 126281. https://doi.org/10.1016/j.physleta.2020.126281.
Wander, A., et al., 2003. Stability of rocksalt polar surfaces: An *ab initio* study of MgO(111) and NiO(111). Phys. Rev. B 68 (233405). https://doi.org/10.1103/PhysRevB.68.233405.
Wang, S., et al., 2009. Wettability and surface free energy of graphene films. Langmuir 25 (18), 11078–11081. https://doi.org/10.1021/la901402f.
Wang, Q.H., et al., 2012. Electronics and optoelectronics of two-dimensional transition metal dichalcogenides. Nat. Nanotechnol. 7 (11), 699–712.
Wang, S., et al., 2014. Shape evolution of monolayer MoS2 crystals grown by chemical vapor deposition. Chem. Mater. 26 (22), 6371–6379.
Wang, F.Q., et al., 2015. Thermoelectric properties of single-layered SnSe sheet. Nanoscale 7 (38), 15962–15970. https://doi.org/10.1039/C5NR03813H.
Wang, H., et al., 2016a. Surface-state-dominated spin-charge current conversion in topological-insulator-ferromagnetic-insulator heterostructures. Phys. Rev. Lett. 117 (7), 076601. https://doi.org/10.1103/PhysRevLett.117.076601.
Wang, R., et al., 2016b. Atomic step formation on sapphire surface in ultra-precision manufacturing. Sci. Rep. 6 (1), 1–9.
Wang, Z., et al., 2016c. Metal induced growth of transition metal dichalcogenides at controlled locations. Sci. Rep. 6 (1), 38394.
Wang, H., et al., 2017. High-quality monolayer superconductor NbSe 2 grown by chemical vapour deposition. Nat. Commun. 8 (1), 394.
Wang, H., et al., 2019a. Fermi level dependent spin pumping from a magnetic insulator into a topological insulator. Phys. Rev. Res. 1 (1), 12014. https://doi.org/10.1103/PhysRevResearch.1.012014.
Wang, H., et al., 2019b. Semimetal or semiconductor: the nature of high intrinsic electrical conductivity in TiS2. J. Phys. Chem. Lett. 10 (22), 6996–7001. https://doi.org/10.1021/acs.jpclett.9b02710.
Wang, Q., et al., 2020. Wafer-scale highly oriented monolayer MoS2 with large domain sizes. Nano Lett. 20 (10), 7193–7199.
Wang, A., et al., 2021. A framework for quantifying uncertainty in DFT energy corrections. ChemRxiv. https://doi.org/10.26434/chemrxiv.14593476.v1.
Wang, X., et al., 2023. Three-dimensional transistors and integration based on low-dimensional materials for the post-Moore's law era. Mater. Today 63, 170–187. https://doi.org/10.1016/j.mattod.2022.11.023.
Wei, P., et al., 2013. Exchange-coupling-induced symmetry breaking in topological insulators. Phys. Rev. Lett. 110 (18), 186807. https://doi.org/10.1103/PhysRevLett.110.186807.
Wei, Y., et al., 2017. Synthesis and investigation of layered GeS as a promising large capacity anode with low voltage and high efficiency in full-cell Li-ion batteries †. Mater. Chem. Front. 1, 1607. https://doi.org/10.1039/c7qm00060j.
West, D., et al., 2012. Native defects in second-generation topological insulators: effect of spin-orbit interaction on Bi 2Se 3. Phys. Rev. B Condens. Matter 86 (12), 1–4. https://doi.org/10.1103/PhysRevB.86.121201.
Wu, S., et al., 2018. Observation of the quantum spin Hall effect up to 100 kelvin in a monolayer crystal. Science 359 (6371), 76–79. https://doi.org/10.1126/science.aan6003.
Wu, Q., et al., 2019. Computational screening of defective group IVA monochalcogenides as efficient catalysts for hydrogen evolution reaction. J. Phys. Chem. C 123 (18), 11791–11797. https://doi.org/10.1021/acs.jpcc.9b02783.
Wu, Y., et al., 2020. Néel-type skyrmion in WTe2/Fe3GeTe2 van der Waals heterostructure. Nat. Commun. 11 (1), 3860. https://doi.org/10.1038/s41467-020-17566-x.
Wuttig, M., et al., 2023. Revisiting the nature of chemical bonding in chalcogenides to explain and design their properties. Adv. Mater. 35 (20). https://doi.org/10.1002/adma.202208485.
Xiang, Y., et al., 2020. Monolayer MoS2 on sapphire: an azimuthal reflection high-energy electron diffraction perspective. 2D Mater. 8 (2), 25003.
Xiao, D., et al., 2012. Coupled spin and valley physics in monolayers of MoS 2 and other group-VI dichalcogenides. Phys. Rev. Lett. 108 (19), 196802.
Xiao, D., et al., 2018. Realization of the axion insulator state in quantum anomalous Hall sandwich heterostructures. Phys. Rev. Lett. 120 (5), 056801. https://doi.org/10.1103/PhysRevLett.120.056801.
Xiao, Z., et al., 2024. Point defect limited carrier mobility in 2D transition metal dichalcogenides. ACS Nano 18, 8511–8516. https://doi.org/10.1021/acsnano.4c01033.
Xie, S., et al., 2018. Coherent, atomically thin transition-metal dichalcogenide superlattices with engineered strain. Science 359 (6380), 1131–1136.
Xiong, K., et al., 2020. Large-scale fabrication of submicrometer-gate-length MOSFETs with a trilayer PtSe2 channel grown by molecular beam epitaxy. IEEE Trans. Electron. Dev. 67 (3), 796–801. https://doi.org/10.1109/TED.2020.2966434.
Xu, S.-Y., et al., 2012. Hedgehog spin texture and Berry's phase tuning in a magnetic topological insulator. Nat. Phys. 8 (8), 616–622. https://doi.org/10.1038/nphys2351.
Xu, B., et al., 2016a. Comparative study of electronic structure and thermoelectric properties of SnSe for Pnma and Cmcm phase. J. Electron. Mater. 45 (10), 5232–5237. https://doi.org/10.1007/s11664-016-4679-y.
Xu, K., et al., 2016b. Synthesis, properties and applications of 2D layered $M^{III}X^{VI}$ (M = Ga, In; X = S, Se, Te) materials. Nanoscale 8 (38), 16802–16818. https://doi.org/10.1039/C6NR05976G.
Xu, L., et al., 2017a. Electronic and optical properties of the monolayer group-IV monochalcogenides M X (M=Ge, Sn; X=S, Se, Te). Phys. Rev. B 95 (23), 235434. https://doi.org/10.1103/PhysRevB.95.235434.
Xu, Y., et al., 2017b. First-principles study on the electronic, optical, and transport properties of monolayer α—and β -GeSe. Phys. Rev. B 96 (24). https://doi.org/10.1103/PhysRevB.96.245421.
Xu, H., et al., 2019. Controlled doping of wafer-scale PtSe2 films for device application. Adv. Funct. Mater. 29 (4). https://doi.org/10.1002/adfm.201805614.
Xuan, Y., et al., 2019. Multi-scale modeling of gas-phase reactions in metal-organic chemical vapor deposition growth of WSe2. J. Cryst. Growth 527, 125247.
Xue, L., et al., 2013. First-principles study of native point defects in Bi 2 Se 3. AIP Adv. 3 (5), 052105. https://doi.org/10.1063/1.4804439.
Xue, D.J., et al., 2017. GeSe thin-film solar cells fabricated by self-regulated rapid thermal sublimation. J. Am. Chem. Soc. 139 (2), 958–965. https://doi.org/10.1021/jacs.6b11705.
Yamashita, T., et al., 2010. Effects of facet orientation on relative stability between zinc blende and wurtzite structures in group III–V nanowires. Jpn. J. Appl. Phys. 49 (055003). https://doi.org/10.1143/JJAP.49.055003.

Yan, F., et al., 2017. Fast, multicolor photodetection with graphene-contacted p -GaSe/n -InSe van der Waals heterostructures. Nanotechnology 28 (27), 27LT01. https://doi.org/10.1088/1361-6528/aa749e.
Yan, J., et al., 2018. Recent progress in 2D/quasi-2D layered metal halide perovskites for solar cells. J. Mater. Chem. A 6 (24), 11063—11077. https://doi.org/10.1039/C8TA02288G.
Yanez, W., et al., 2021. Spin and charge interconversion in Dirac-semimetal thin films. Phys. Rev. Appl. 16 (5), 054031. https://doi.org/10.1103/PhysRevApplied.16.054031.
Yanez, W., et al., 2022. Giant Dampinglike-Torque Efficiency in Naturally Oxidized Polycrystalline Ta As Thin Films. Phys. Rev. Appl. 18 (5), 054004. https://doi.org/10.1103/PhysRevApplied.18.054004.
Yang, M.H., Flynn, C.P., 1989. Growth of alkali halides from molecular beams: global growth characteristics. Phys. Rev. Lett. 62.
Yang, L., et al., 2014a. Chloride molecular doping technique on 2D materials: WS2 and MoS2. Nano Lett. 14 (11), 6275—6280.
Yang, S., et al., 2014b. High performance few-layer GaS photodetector and its unique photo-response in different gas environments. Nanoscale 6 (5), 2582—2587. https://doi.org/10.1039/C3NR05965K.
Yang, W., et al., 2014c. Proximity effect between a topological insulator and a magnetic insulator with large perpendicular anisotropy. Appl. Phys. Lett. 105 (9), 092411. https://doi.org/10.1063/1.4895073.
Yang, J., et al., 2019. Electrical doping effect of vacancies on monolayer MoS_2. J. Phys. Chem. C 123 (5), 2933—2939. https://doi.org/10.1021/acs.jpcc.8b10496.
Yang, M., et al., 2022. Progress on two-dimensional binary oxide materials. Nanoscale 14, 9576. https://doi.org/10.1039/d2nr01076c.
Yasuda, K., et al., 2016. Geometric Hall effects in topological insulator heterostructures. Nat. Phys. 12 (6), 555—559.
Yazdani, S., Yarali, M., Cha, J.J., 2019. Recent progress on in situ characterizations of electrochemically intercalated transition metal dichalcogenides. Nano Res. 12, 2126—2139.
Younas, R., Zhou, G., Hinkle, C.L., 2023. A perspective on the doping of transition metal dichalcogenides for ultra-scaled transistors: challenges and opportunities. Appl. Phys. Lett. 122 (16).
Yu, H., et al., 2017. Wafer-scale growth and transfer of highly-oriented monolayer MoS2 continuous films. ACS Nano 11 (12), 12001—12007.
Yu, H., et al., 2018. Unraveling a novel ferroelectric GeSe phase and its transformation into a topological crystalline insulator under high pressure. NPG Asia Mater. 10 (9), 882—887. https://doi.org/10.1038/s41427-018-0081-y.
Yu, Y., et al., 2019. Room-temperature electron—hole liquid in monolayer MoS2. ACS Nano 13 (9), 10351—10358.
Yu, M., et al., 2021. Review of nanolayered post-transition metal monochalcogenides: synthesis, properties, and applications. ACS Appl. Nano Mater. https://doi.org/10.1021/acsanm.3c05984.
Yu, M., Murray, L., Doty, M., Law, S., 2023. Epitaxial growth of atomically thin Ga_2Se_2 films on c-plane sapphire substrates. J. Vac. Sci. Technol. A 41 (032704). https://doi.org/10.1116/6.0002446.
Yu, M., Iddawela, S.A., et al., 2024a. Quasi-van der Waals Epitaxial Growth of gamma-GaSe Thin Films on GaAs(111)B Substrates. arXiv, [Preprint]. http://arxiv.org/abs/2403.12265. https://doi.org/10.1021/acsnano.4c04194.
Yu, M., Hilse, M., et al., 2024b. Review of nanolayered post-transition metal monochalcogenides: synthesis, properties, and applications. ACS Appl. Nano Mater. https://doi.org/10.1021/acsanm.3c05984.
Yu, M., Wang, J., et al., 2024c. Treatment and aging studies of GaAs(111)B substrates for van der Waals chalcogenide film growth treatment and aging studies of GaAs(111)B substrates for van der Waals chalcogenide film growth. J. Vac. Sci. Technol. B 42, 33201. https://doi.org/10.1116/6.0003470.
Yue, R., Nie, Y., Walsh, L.A., et al., 2017. Nucleation and growth of WSe2: enabling large grain transition metal dichalcogenides. 2D Mater. 4 (4), 045019. https://doi.org/10.1088/2053-1583/aa8ab5.
Yüksek, M., 2012. Nonlinear refraction effects of amorphous semiconductor InSe thin films according to film thicknesses and/or pulse durations. Opt Commun. 285 (24), 5472—5474. https://doi.org/10.1016/j.optcom.2012.08.066.
Zehen Prit Singh, 2023. The power of semiconductor materials paving the way for technological advancements. Adv. Mater. Sci. Res. 6 (4), 67—69. https://doi.org/10.37532/aaasmr.2023.
Zemel, J.N., Jensen, J.D., Schoolar, R.B., 1965. Electrical and optical properties of epitaxial films of PbS, PbSe, PbTe, and SnTe. Phys. Rev. 140 (1A), A330. https://doi.org/10.1103/PhysRev.140.A330.
Zeng, L., et al., 2023. Reversible growth of halide perovskites via lead oxide hydroxide nitrates anchored zeolitic imidazolate frameworks for information encryption and decryption. ACS Nano 17 (5), 4483—4494. https://doi.org/10.1021/acsnano.2c10170.
Zhai, K., 2023. The changing landscape of semiconductor manufacturing: why the health sector should care. Front. Health Serv. 3, 1198501.
Zhang, H., et al., 2009. Topological insulators in Bi2Se3, Bi2Te3 and Sb2Te3 with a single Dirac cone on the surface. Nat. Phys. 5 (6), 438—442. https://doi.org/10.1038/nphys1270.
Zhang, J., et al., 2011. Band structure engineering in (Bi(1-x)Sb(x))(2)Te(3) ternary topological insulators. Nat. Commun. 2, 574. https://doi.org/10.1038/ncomms1588.
Zhang, D., et al., 2012a. Interplay between ferromagnetism, surface states, and quantum corrections in a magnetically doped topological insulator. Phys. Rev. B 86 (20), 205127. https://doi.org/10.1103/PhysRevB.86.205127.
Zhang, J.-M., et al., 2012b. Tailoring magnetic doping in the topological insulator Bi 2 Se 3. Phys. Rev. Lett. 109 (26), 266405. https://doi.org/10.1103/PhysRevLett.109.266405.
Zhang, L., et al., 2012c. High quality ultrathin Bi2Se3 films on CaF2 and CaF2/Si by molecular beam epitaxy with a radio frequency cracker cell. Appl. Phys. Lett. 101 (15), 153105. https://doi.org/10.1063/1.4758466.
Zhang, H., Liu, C.-X., Zhang, S.-C., 2013a. Spin-orbital texture in topological insulators. Phys. Rev. Lett. 111 (6), 066801. https://doi.org/10.1103/PhysRevLett.111.066801.
Zhang, J., et al., 2013b. Topology-driven magnetic quantum phase transition in topological insulators. Science (New York, N.Y.) 339 (6127), 1582—1586. https://doi.org/10.1126/science.1230905.
Zhang, W., et al., 2014. Two-dimensional semiconductors with possible high room temperature mobility. Nano Res. 7 (12), 1731—1737. https://doi.org/10.1007/s12274-014-0532-x.
Zhang, X., et al., 2015. Flux method growth of bulk MoS_2 single crystals and their application as a saturable absorber. CrystEngComm 17 (21), 4026—4032.
Zhang, Y.N., 2015. Communication: surface stability and topological surface states of cleaved Bi_2Se_3: first-principles studies. J. Chem. Phys. 143 (151101). https://doi.org/10.1063/1.4933298.
Zhang, J., et al., 2016a. Band structure and spin texture of BiSe3 3*d* ferromagnetic metal interface. Phys. Rev. B 94 (1), 014435. https://doi.org/10.1103/PhysRevB.94.014435.
Zhang, X., et al., 2016b. Influence of carbon in metalorganic chemical vapor deposition of few-layer WSe 2 thin films. J. Electron. Mater. 45 (12), 6273—6279.
Zhang, F., et al., 2017a. Controlled synthesis of 2D transition metal dichalcogenides: from vertical to planar MoS2. 2D Mater. 4 (2), 25029.
Zhang, J., et al., 2017b. Janus monolayer transition-metal dichalcogenides. ACS Nano 11 (8), 8192—8198.
Zhang, L., et al., 2017c. Ferromagnetism in vanadium-doped Bi2Se3 topological insulator films. Apl. Mater. 5 (7), 76106.
Zhang, K., et al., 2018a. Considerations for utilizing sodium chloride in epitaxial molybdenum disulfide. ACS Appl. Mater. Interfaces 10 (47), 40831—40837.
Zhang, X., et al., 2018b. Diffusion-controlled epitaxy of large area coalesced WSe2 monolayers on sapphire. Nano Lett. 18 (2), 1049—1056.
Zhang, D., et al., 2019a. Topological axion states in the magnetic insulator $MnBi_2Te_4$ with the quantized magnetoelectric effect. Phys. Rev. Lett. 122 (20), 206401. https://doi.org/10.1103/PhysRevLett.122.206401.
Zhang, F., et al., 2019b. Full orientation control of epitaxial MoS2 on hBN assisted by substrate defects. Phys. Rev. B 99 (15), 155430. https://doi.org/10.1103/PhysRevB.99.155430.
Zhang, X., et al., 2019c. Defect-controlled nucleation and orientation of WSe2 on hBN: a route to single-crystal epitaxial monolayers. ACS Nano 13 (3), 3341—3352. https://doi.org/10.1021/acsnano.8b09230.

Zhang, Z., et al., 2019d. Recent progress in the controlled synthesis of 2D metallic transition metal dichalcogenides. Nanotechnology 30 (18), 182002.
Zhang, L., et al., 2020. Recent advances in emerging Janus two-dimensional materials: from fundamental physics to device applications. J. Mater. Chem. A 8 (18), 8813–8830.
Zhang, X., et al., 2021. Room-temperature intrinsic ferromagnetism in epitaxial CrTe2 ultrathin films. Nat. Commun. 12 (1), 2492. https://doi.org/10.1038/s41467-021-22777-x.
Zhao, S., et al., 2015a. Controlled synthesis of single-crystal SnSe nanoplates. Nano Res. 8 (1), 288–295. https://doi.org/10.1007/s12274-014-0676-8.
Zhao, Y., et al., 2015b. Anisotropic magnetotransport and exotic longitudinal linear magnetoresistance in WT e 2 crystals. Phys. Rev. B 92 (4), 41104.
Zhou, Z., Chien, Y.-J., Uher, C., 2005. Thin-film ferromagnetic semiconductors based on Sb2−xVxTe3 with TC of 177K. Appl. Phys. Lett. 87 (11), 112503. https://doi.org/10.1063/1.2045561.
Zhou, Z., et al., 2006a. Carrier-mediated ferromagnetism in vanadium-doped (Sb[sub 1-x]Bi[sub x])[sub 2]Te[sub 3] solid solutions. Appl. Phys. Lett. 88 (19), 192502. https://doi.org/10.1063/1.2200738.
Zhou, Z., Chien, Y.-J., Uher, C., 2006b. Thin film dilute ferromagnetic semiconductors Sb 2 − x Cr x Te 3 with a Curie temperature up to 190 K. Phys. Rev. B 74 (22), 224418. https://doi.org/10.1103/PhysRevB.74.224418.
Zhou, Y., et al., 2014. Epitaxy and photoresponse of two-dimensional GaSe crystals on flexible transparent mica sheets. ACS Nano 8 (2), 1485–1490. https://doi.org/10.1021/nn405529r.
Zhou, J., Lin, J., et al., 2018a. A library of atomically thin metal chalcogenides. Nature 556 (7701), 355–359.
Zhou, J., Shi, J., et al., 2018b. InSe monolayer: synthesis, structure and ultra-high second-harmonic generation. 2D Mater. 5 (2), 025019. https://doi.org/10.1088/2053-1583/aab390.
Zhou, J.C., et al., 2021. Polycrystalline SnSe with a thermoelectric figure of merit greater than the single crystal. Nat. Mater. 20 (10), 1378–1384. https://doi.org/10.1038/s41563-021-01064-6.
Zhu, Z.Y., Cheng, Y.C., Schwingenschlögl, U., 2011. Giant spin-orbit-induced spin splitting in two-dimensional transition-metal dichalcogenide semiconductors. Phys. Rev. B 84 (15), 153402.
Zhu, X.-G., et al., 2013. Three Dirac points on the (110) surface of the topological insulator Bi1−xSbx. New J. Phys. 15 (10), 103011. https://doi.org/10.1088/1367-2630/15/10/103011.
Zhu, B., Chen, X., Cui, X., 2015. Exciton binding energy of monolayer WS2. Sci. Rep. 5 (1), 9218.
Zhu, Y., et al., 2021. Anisotropic point defects in rhenium diselenide monolayers. iScience 24 (12), 103456. https://doi.org/10.1016/j.isci.2021.103456.
Zhu, H., Nayir, N., Choudhury, T.H., et al., 2023a. Step engineering for nucleation and domain orientation control in WSe2 epitaxy on c-plane sapphire. Nat. Nanotechnol. 18 (11), 1295–1302. https://doi.org/10.1038/s41565-023-01456-6.
Zhu, J., et al., 2023b. Low-thermal-budget synthesis of monolayer molybdenum disulfide for silicon back-end-of-line integration on a 200 mm platform. Nat. Nanotechnol. 18 (5), 456–463.
Zhussupbekov, K., et al., 2021. Imaging and identification of point defects in PtTe2. Npj 2D Materials and Applications 5 (1), 14. https://doi.org/10.1038/s41699-020-00196-8.